THESE

Initial and Plasmon-Enhanced Optical Properties of Nanostructured Silicon Carbide

présentée devant
L'Institut National des Sciences Appliquées de Lyon

pour obtenir
le grade de docteur

Ecole doctorale: Matériaux de Lyon

par
Yuriy ZAKHARKO
Soutenance le 30 octobre 2012 devant la Commission d'examen

Jury

Rapporteur	LERONDEL Gilles	Professeur (Université de Technologie Troyes)
Rapporteur	ROZHIN Alex	Professeur (Aston University)
Président	DUJARDIN Christophe	Professeur (Université Claude Bernard Lyon 1)
Examinateur	DEREUX Alain	Professeur (Université de Bourgogne)
Examinateur	PAILLARD Vincent	Professeur (Université de Toulouse)
Directeur de these	BLUET Jean-Marie	Maître de Conférences (INSA-Lyon)
Examinateur	MONNIER Virginie	Maître de Conférences (Ecole Central de Lyon)

Cette thèse a été préparée à l'Institut des Nanotechnologies de Lyon de l'INSA de LYON

Acknowledgements

The research conducted during my thesis would not have been possible without the support of many people. First and foremost, I wish to express my deep sense of gratitude to the former and current directors of Lyon Insitute of Nanotechnology (INSA-Lyon) Gerard Guillot and Catherine Bru-Chavellier, for providing the opportunity to join the lab with a good environment and facilities to carry out my research. I would like also to convey thanks to the members of the administration helping me through all the procedures required for the completion of the thesis.

I sincerely thank to my thesis supervisors Jean-Marie Bluet and Vladimir Lysenko, for their patient guidance, enthusiastic encouragement, useful critiques and for offering fascinating subject. My very great appreciation goes to Jean-Marie Bluet for his valuable and constructive suggestions during the planning and development of the thesis that helped me tremendously in completing everything in time.

I would like to gratefully acknowledge the motivating and energetic supervision of Vladimir Lysenko during my Master research, which successfully evolved into advanced studies during the thesis. A special thanks for his helping hand and numerous stimulating discussions in many professional and personal matters.

I wish to extend my thanks for the support given by all the technicians in our laboratory. A warm thank goes to Philippe Girard and Robert Perrin for their help. I also thank Joëlle Grégoire, Khaled Ayadi and Andrei Sabac from NanoLyon team for their assistance in the chemistry lab.

I would like to show my greatest appreciation to Jacques Botsoa for the invaluable assistance and masterpiece during my Master research and precious help with optical measurements and relevant discussions. Without this support, my thesis work would not be so efficient.

Deepest gratitude is also due to people who enriched my thesis with their help and expertise. Willingness of Tetyana Nychyporuk to give her time so generously during numerous measurements and sample preparations is also very much appreciated. Sergei Alekseev from Kyiv National University is thanked for his endless interest, valuable experiments and hints in chemistry. An honourable mention goes to Luigi Bonacina and his colleagues from Biophotonics group at University of Geneva for fruitful cooperation in nonlinear optical characterization. I also thank Olivier Marty for TEM characterisation.

Important part of this thesis related to plasmonic nanohybrids would not have been possible without the collaboration with Chemistry and Nanobiotechnology group of INL at Ecole Centrale de Lyon. My sincere thanks go to Virginie Monnier and Ning Sui for their professionalism and persistence in solving problems we have encountered. I also appreciate the willingness of Yann Chevolot to respond on my requests for absorption UV-Visible measurements.

I sincerely thank Alain Geloen, CNRS researcher from Cardiovascular, Metabolism, Diabetologia and Nutrition (CarMeN) laboratory, giving me access to his laboratory for manipulations, which have been very crucial for my thesis. I also thank his Master student Tetiana Serdiuk for providing help with biological sample preparation and characterization, which is a part of the experimental results of my thesis.

I would like to express very great appreciation to Kuzyk Raisa Grygorivna, my teacher of physics at Lviv Physics and Mathematics Lyceum who cultivated significant interest and inspiration in physics throughout my studies. Special thanks to Skryshevsky Valeriy Antonovych, my former scientific supervisor at Kyiv National University for the opportunity to work with him on the cutting-edge subjects, which eventually led to my Master and thesis research at INL.

Finally, I am forever indebted to my family and relatives for their understanding, endless patience and encouragement when it was most required. I am grateful to all my friends in Lyon and abroad for spending great times and their help.

Résumé

Le carbure de silicium (SiC) nanostructuré est considéré aujourd'hui comme une bonne alternative aux matériaux traditionnels pour diverses applications multidisciplinaires. Dans cette thèse, des nanostructures de SiC ont été élaborées par gravure électrochimique et par ablation laser. La première partie de cette thèse décrit et explique la dépendance en taille des propriétés optiques ainsi que l'importance des effets de champ local sur les transitions électroniques photo-induites des nanostructures de SiC. Dans la seconde partie, il est démontré une amplification d'un facteur 15 de l'intensité de photoluminescence des nanoparticules de SiC par leurs interactions en champ proche avec les plasmons multipolaires localisées. En outre, un facteur 287 et un facteur 72, induits par le couplage plasmonique, sont obtenus respectivement pour les signaux de luminescence à deux photons et de génération de seconde harmonique. Les principaux mécanismes physiques responsables des effets observés ont été décrits par des simulations de type différences finies dans le domaine temporel en trois dimensions. Enfin, l'effet de couplage de nanoparticules de SiC luminescentes à des nanostructures plasmoniques en structures planes est utilisé pour améliorer le marquage de cellules biologiques. Une perspective est ouverte sur la réalisation et les premières caractérisations de suspension colloïdales de nanohybrides plasmonique (Au@SiO_2)SiC.

Mots-clés: Nanostructures de SiC, Confinement quantique, Photoluminescence, Réponse optique non linéaire, Exaltation plasmonique, Marquage biologique.

Abstract

Nanostructured silicon carbide (SiC) is considered today as a good alternative to the conventional materials for various multidisciplinary applications. In this thesis, SiC nanostructures were elaborated by means of electrochemical etching and laser ablation techniques. The first part of the thesis clarifies size-dependence of optical properties as well as importance of local-field effects onto the photoinduced electronic transitions of SiC nanostructures. In the second part of the thesis strong 15-fold photoluminescence enhancement of SiC nanoparticles is ensured by their near-field interactions with multipolar localized plasmons. Further, 287-fold and 72-fold plasmon-induced enhancement factors of two-photon excited luminescence and second harmonic generation is achieved, respectively. The main physical mechanisms responsible for the observed effects were described by three-dimensional finite-difference time domain simulations. Finally, the coupling effect of luminescent SiC nanoparticles to plasmonic nanostructures is used in the enhanced labelling of biological cells on the planar structures. As a perspective, colloidal plasmonic (Au@SiO_2)SiC nanohybrids were elaborated and characterized.

Keywords: SiC nanostructures, Quantum confinement, Photoluminescence, Nonlinear optical response, Plasmon enhancement, Bioimaging.

Contents

List of Abbreviations

AFM	atomic force microscopy
DFT	density-functional theory
DFT-LDA	DFT in local-density approximation
DLS	dynamic light scattering
EDX	energy-dispersive X-ray spectroscopy
ELS	electrophoretic light scattering
FDTD	finite-difference time-domain
FED	field emission diode
FET	field effect transistor
FTIR	Fourier transform infrared spectroscopy
GWA	GW approximation
HF	hydrofluoric acid
HHG	high harmonic generation
HOMO	highest occupied molecular orbital
LUMO	lowest unoccupied molecular orbital
NC	nanocrystal
NH	nanohybrid
NP	nanoparticle
NW	nanowire
PISHG	photo-induced second-harmonic generation
PL	photoluminescence
QD	quantum dot
SEM	scanning electron microscopy
SHG	second-harmonic generation
TEM	transmission electron microscopy
TPA	two-photon absorption
TPD-MS	temperature programmed desorption mass spectrometry
TPPL	two-photon excited photoluminescence

List of Figures

General Introduction

The strong efforts have been made in nanoscience and nanotechnology to optimize and exploit the potential of materials. Nanoscale engineering allows dramatic extension of their basic properties and also leads to new applications.

Nanostructuring of silicon carbide (SiC) is not an exception. Bulk SiC is a wide band gap IV-IV semiconductor with interesting and well-known physical properties. The SiC nanostructures have received recently considerable attention because of their potential applications in the stable emitting blue or ultraviolet light. According to the theory of quantum and spatial confinements, reduction in size of the SiC to values comparable to the Bohr radius of the exciton should lead to a strong enhancement of linear and nonlinear optical properties.

The first objective of this thesis is to fabricate SiC nanostructures and to study their optical properties. Particular attention is paid to the size- and local-field dependent properties and related effects. Although the original optical properties of SiC nanostructures have been discussed in literature, the overall brightness of SiC nanoparticles (NPs) is lower when compared to commonly used dyes and other semiconductor NPs. What is more, in comparison with conventional non-linear crystals, the reported nonlinear optical characteristics of the SiC nanostructures have to be enhanced. To overcome such limitations the second part of this thesis focuses on controlling plasmon-enhanced optical properties.

In plasmonics, a simple principle of electromagnetic field confinement (i.e. enhancement) in the dimensions smaller than the wavelength of light is used. This in turn, can be effectively implemented to alter numerous physical properties of surrounding media. Recently, progress in fabrication techniques of plasmon nanostructures has already boosted the interest in plasmon enhanced fluorescence, high harmonic generation and photovoltaic research. Special efforts have been devoted to the implementation of plasmonics in medicine and biology.

In the first chapter, general overview of SiC nanostructures is made. Firstly, physical properties of bulk SiC are discussed in details. Secondly, several techniques known to be effectively used for SiC nanostructuring are described. Afterwards, the state of the art on the luminescence properties of SiC nanostructures is discussed. Finally, different multidisciplinary applications of nanostructured SiC are listed.

The second chapter focuses on the description of the SiC nanostructures fabrication methods applied in the thesis. This includes electrochemical etching and laser ablation

techniques. Further, production steps of planar and colloidal plasmonic nanostructures are clarified. The main characterization techniques used in this thesis are discussed at the end of the chapter.

In the third and fourth chapters, complete investigation of initial and plasmon enhanced optical properties of the fabricated SiC nanostructures is made. These studies cover both linear (UV-Vis absorption, photoluminescence) and nonlinear (two-photon absorption, second harmonic generation, two-photon excited luminescence) optical properties.

Finally, the fifth chapter demonstrates the possibilities of plasmon-enhanced nano-SiC labelling of biological cells. Preliminary fabrication and characterization results on colloidal (Au@SiO_2)SiC nanohybrids are presented as perspective of ultrabright biocompatible light emitters.

Chapter 1

Silicon Carbide Nanostructures: State of Art

Materials science being an interdisciplinary field investigates the relationship between the structural and macroscopic properties of materials at atomic or molecules scales. Increased attention to nanoscience and nanotechnology in recent years also provoked significant advances in materials science. The most promising among all known examples is the continuous development of revolutionary semiconductor and biomaterials technologies. But stable industries also employ materials scientists to make incremental improvements and troubleshoot issues with currently used materials. Silicon is the most commercially used semiconductor. Dozens of other materials are used, including germanium, gallium arsenide, and silicon carbide.

In this chapter, overview of nanostructured silicon carbide as a good alternative to the conventional materials for various multidisciplinary light-emitting applications will be presented. At the beginning, the general physical properties of bulk SiC will be introduced. Second section of the chapter will describe how nanostructured SiC can be fabricated. Third section is devoted to the detailed description of the optical properties gained after SiC nanostructuring. Eventually, last section reveals importance of the nanostructured SiC for wide range of applications.

1.1. Physical properties of bulk silicon carbide

Silicon carbide (SiC) is a binary compound semiconductor material composed of silicon and carbon. Very pure SiC is white or colourless, but produced by different technologies and from various raw materials can be black, grey, yellow or green in colour (**Figure 1.1**). For mass-production SiC is manufactured artificially due to an extremely rare natural appearance.

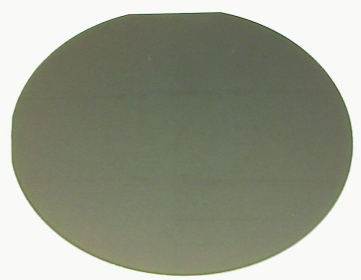

***Figure 1.1**: Silicon carbide substrate.*

During crystallization silicon and carbon, being IV group elements of periodic table, create covalent bonds with small degree of ionicity. Large number of different SiC crystalline forms is divided by similar structures called polytypes. The SiC polytypes are recognized by the stacking sequence of the tetrahedrally bonded Si-C bilayers, where the individual bond lengths and local atomic environments are nearly identical, while the overall symmetry of the crystal is determined by the stacking periodicity. Depending on the stacking order, the bonding between Si and C atoms in adjacent bilayer planes is either of a zinc-blende (cubic) or wurtzite (hexagonal) nature (**Figure 1.2**).

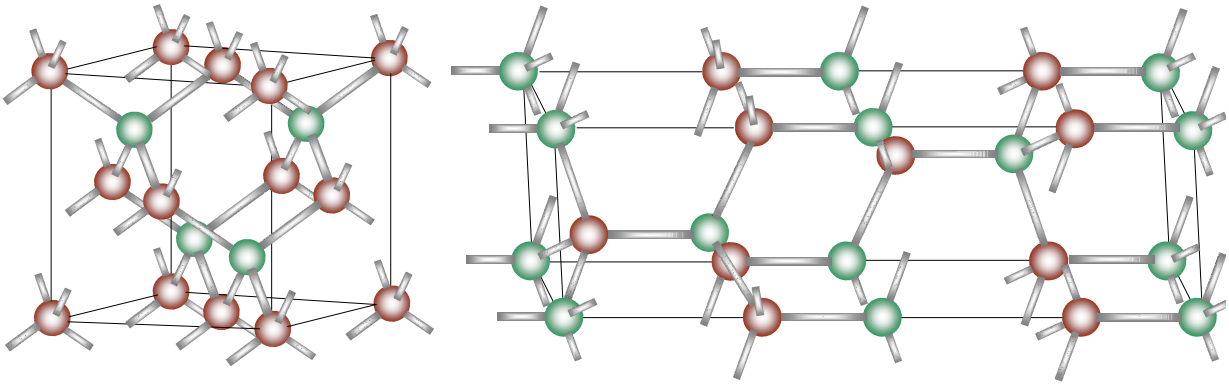

***Figure 1.2:** Crystalline structure of (a) 3C-SiC (cubic) and (b) 6H-SiC (hexagonal) polytypes.*

The physical properties of SiC are highly dependent on its polytype. Cubic (3C) polytype has the highest electron mobility and saturation velocity because of reduced phonon scattering resulting from the higher symmetry. The indirect band gaps differ among the polytypes ranging from 2.39 eV for 3C-SiC to 3 eV in 6H SiC, or 3.23 eV for 4H-SiC (see **Table 1.1**). Generally speaking, the greater the wurtzite component, the larger is the band gap. 6H-SiC polytype is most easily prepared and best studied, while the 3C and 4H polytypes are attracting more attention due to their superior electronic properties. In addition,

SiC has a large avalanche breakdown field, and an excellent thermal conductivity, all of which make it ideal for high-power operation [1].

Despite its indirect band gap, blue SiC LEDs are commercially available. The efficiency of these devices is less than 0.03%, but that is partly compensated by the ability to drive these LEDs at high currents. Moreover, large Si-C bonding energy allows use of elaborated yellow, green and blue emitting SiC LEDs in significant temperature and radiation fluence ranges [2].

As a wide-band-gap semiconductor, SiC is desirable for UV optical detection applications in consequence of insensitivity to longer wavelengths and very small dark current levels, even at elevated temperatures. Low dark current enables SiC photodiodes to exceed Si UV sensitivities by four orders of magnitude. The ruggedness of SiC is also an important advantage for UV detection, where hostile environments such as in-situ combustion monitoring and satellite-based missile plume detection are involved.

The **Table 1.1** summarizes main physical properties of three SiC polytypes [3-5].

Polytype	3C (β)	4H	6H
Crystal structure	Cubic	Hexagonal	Hexagonal
Lattice constants (Å)	4.3596	3.0730 ; 10.053	3.0730 ; 15.11
Density (g/cm^3)	3.21	3.21	3.21
Bandgap (eV)	2.39	3.23	3.0
Thermal conductivity (W/(cm·K))	3.6	3.7	4.9
Dielectric constant (static) (300K)	9.72	9.66 (⊥) 10.03 (∥)	9.66 (⊥) 10.03 (∥)
Dielectric constant (high frequency) (300K)	6.52	6.52 (⊥) 6.70 (∥)	6.52 (⊥) 6.70 (∥)
Infrared refractive index(300K)	2.55	2.55 (⊥) 2.59 (∥)	2.55 (⊥) 2.59 (∥)
Electron mobility ($cm^2\ V^{-1}\ s^{-1}$, 300K)	≤1000	≤850	≤450
Hole mobility ($cm^2\ V^{-1}\ s^{-1}$, 300K)	≤40	≤120	≤100

Table 1.1: *Summary of main physical properties for three SiC polytypes.*

In addition, SiC is attractive for nonlinear optics applications. The optical damage threshold is an important characteristic of any nonlinear material because of the higher device efficiency with increasing power density. The performances of many materials are limited by modest damage thresholds. The extremely high melting point (T~3100K) and thermal conductivity of bulk SiC suggest the possibility of a high durability and threshold values. Large electro-optic coefficients are expected in SiC polytypes, which will make this compound an excellent candidate for electro-optical devices in the visible and near ultraviolet region [6].

Table 1.2 lists the static SHG coefficients (in units of pm/V) of independent tensor components for 4H, 6H and 3C polytypes [6-9]. Theoretical evaluations are based on the ab-initio pseudo-potential calculation within density-functional theory in local-density approximation (DFT-LDA) with or without "scissors" operator, or in GW approximation. The sign of the components were adapted to the common coordinate system as in [7]. Additionally, semi-ab-initio tight-binding calculation in case of low-frequency third-order susceptibilities estimates values $\chi^{(3)}_{1111}$ =0.029 and $3\chi^{(3)}_{1212}$=0.043 (in 10^{-11} esu) [10].

Polytype	4H		6H		3C	
Component	$\chi^{(2)}_{zzz}$	$\chi^{(2)}_{zxx}$	$\chi^{(2)}_{zzz}$	$\chi^{(2)}_{zxx}$	$\chi^{(2)}_{zzz}$	$\chi^{(2)}_{zxx}$
DFT-LDA [7]	15.5	-9.7	18.1	-9.8	20.4	-10.2
Within GWA [7]	9.8	-6.3	8.3	-4.6	17.2	-8.6
With scissors [7]	8.6	-5.6	9.1	-5.1	13.2	-6.6
DFT-LDA [8]	14.5	-8.9	17.8	-9.7	20.2	-10.1
With scissors [8]	9.2	-5.7	11.4	-6.3	13.0	-6.5
DFT-LDA [9]	23.3	-14.8	27.6	-15.0	28.2	-14.2
With scissors [9]	15.6	-10.0	18.6	-10.4	18.4	-9.2
Experimental [6]	18±8	-4±2	24±10	-4±2		

Table 1.2: *Theoretical and experimental results of second-order low-frequency susceptibilities for three SiC polytypes.*

1.2. Methods for SiC nanostructuring

Among the main methods on the nano-SiC synthesis it is worth discussing of the most notable: a) laser ablation, b) chemical vapour synthesis, c) ion implantation followed by thermal annealing, d) laser pyrolysis, and e) electro- and electroless chemical etching. A brief description of the mentioned methods will be done in the next section.

1.2.1. Laser ablation

The diagram of laser ablation technique is shown in **Figure 1.3**. The basic method includes focusing of a pulsed laser beam on a bulk target, located on the rotating stage in a vacuum chamber. In contact with laser beam, heated material is ejected from the target and deposited onto the opposite substrate. Nanostructures are developed on the cooler surfaces through sequential condensation. This process can occur in ultra high vacuum or in the presence of a background gas.

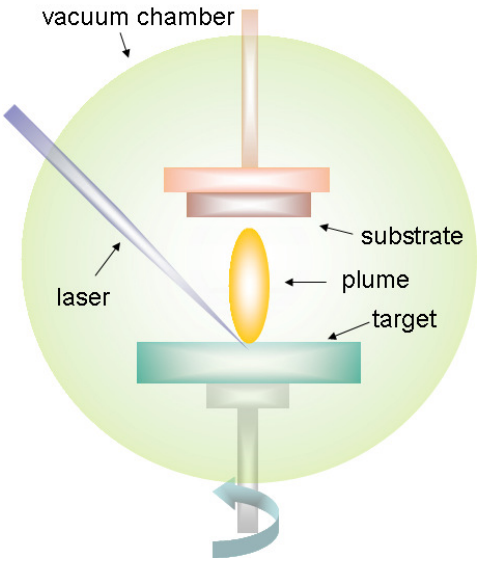

Figure 1.3: *Operation principle of laser ablation.*

Commercially available SiC target and deposition substrates of silicon or molybdenum are used in the fabrication of nano-SiC [11, 12]. The variation of the substrate temperature and material allows the controlled synthesis of SiC nanosprouts, nanowires, and nanoneedles. Laser ablation may also be used to form uniform arrays of periodic nanoparticles (NPs) on the initial SiC target substrate [13, 14]. The period of 80 nm was much smaller than the wavelength of the laser beam (λ=400 nm). Thus, the formation of short-period NPs was attributed to the second harmonic generation on the surface of SiC target.

Alternatively, the laser ablation can be carried out in a solution [15]. In this variation, laser beam is focused on silicon wafer (as Si source) immersed in ethanol which acts as carbon source. Schematic view of the procedure can be seen in **Figure 1.4**. Additional chemical etching was implemented to eliminate formation of Si NPs. In the end, this technique allows production of 3C-SiC particles only few nanometres in size.

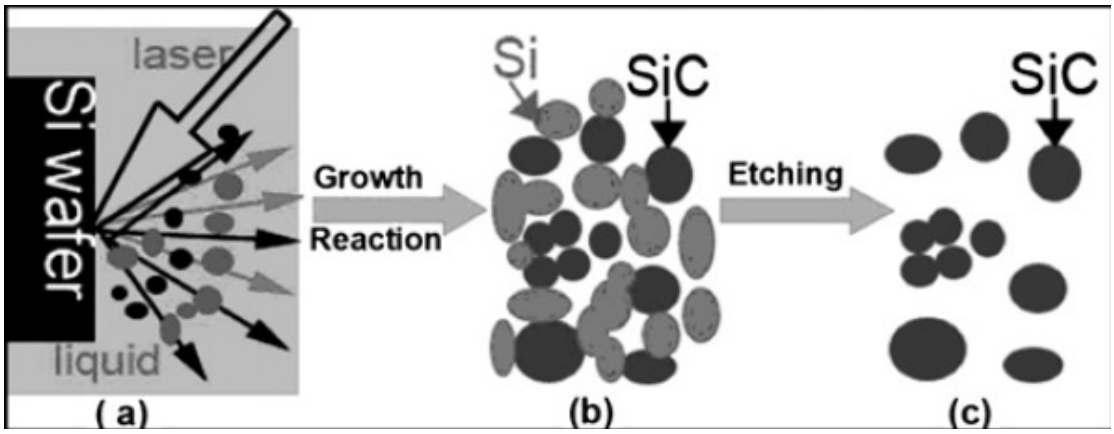

***Figure 1.4**: Illustration of the formation process for SiC NPs: (a) Formation of Si clusters (grey dots) and C atoms (black dots) due to laser-induced Si plasma and its subsequent cooling. (b) 3C-SiC and Si NPs formed after one shot of pulsed laser. (c) Only SiC NPs are left after etching with a HF–H_2O_2 aqueous solution [15].*

1.2.2. Chemical vapour synthesis

In conventional chemical vapor synthesis, films are deposited by surface reaction between gaseous species and a substrate (**Figure 1.5**). Formation of particles is usually initiated through decomposition of the precursor molecules in the gas phase at high temperatures, pressures, and precursor concentrations. 3C-SiC NPs with dimensions around 3-10 nm can be grown in a hot wall reactor using tetramethylsilane [$(CH_4)Si$] as precursor (**Figure 1.6a**). By changing the decomposition temperature and reactor pressure, the clusters may be amorphous or crystalline at low and elevated temperatures, respectively [16, 17].

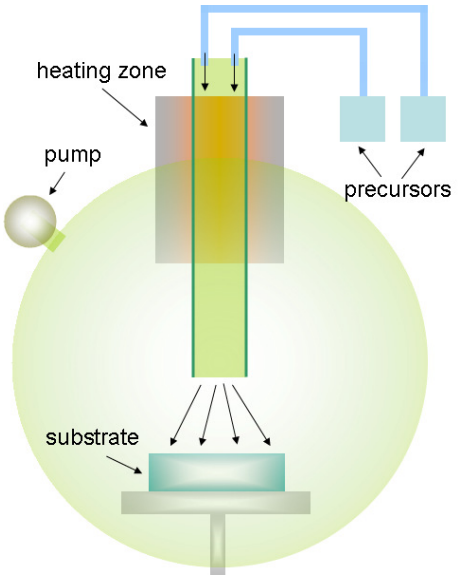

***Figure 1.5:** Operation principle of chemical vapour deposition technique.*

Amorphous SiC nanosprings, as well as biphase (crystalline core/amorphous sheath) helical nanowires have been synthesized by plasma enhanced chemical vapour deposition [18]. The precursor for growing SiC nanosprings was closo-l,2-dicarbadodecaborane ($C_2B_{10}H_{12}$) as the carbon source, while the Si substrate acts as the Si source. The diameter of the nanosprings in **Figure 1.6b** is 110 nm with nanowire diameters of 52 nm and 70 nm pitches.

Nanobelts of SiC have been prepared by a reaction of CH_3CH_2OH, $SiCl_4$, and Li in an autoclave at 600 °C. [19]. Electron microscopy investigations revealed that the nanobelts are usually 50-200 nm wide, 20-60 nm thick, and up to tens of micrometers long.

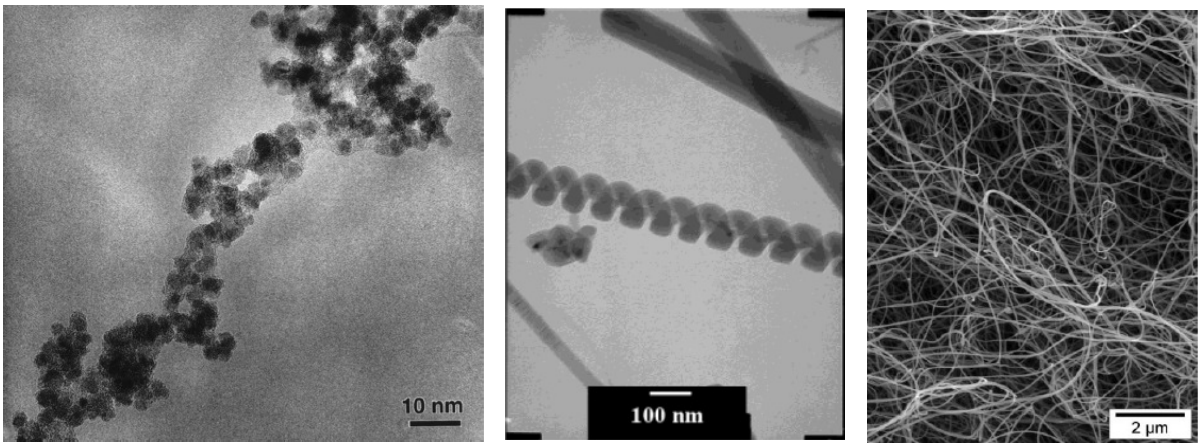

(a) (b) (c)

***Figure 1.6**: (a) TEM image of the SiC clusters with sizes ranging from 3 to 10 nm [16]; (b) TEM images of amorphous silicon carbide nanosprings [18]; (c) SEM image of a self-supported felt of SiC-based nanocables [20].*

Solid precursors of Si and C, namely SiO and polypropylene have been used in order to drastically decrease the cost of the resulting SiC-based nanocables compared to conventional high-purity gaseous reactants [20]. The main feature of these nanowires (**Figure 1.6c**) is their length estimated to be as long as 500 µm, while SEM pictures demonstrate nanowires with diameters in the range of 20–40 nm.

1.2.3. Ion implantation

Ion implantation is the method of ions introduction into a substrate at energies that allow their penetration beyond the surface. Conventionally used for the purpose of doping, this method can be used for the formation of nanocrystals (NCs) surrounded by a host matrix. Same approach was considered to obtain SiC NCs. For example, 3C-SiC NCs were formed by carbon implantation into Si substrate at 35 keV with various dose, followed by post-implantation annealing at 1200 °C for 30 min in Ar atmosphere [21]. Thermal dry-oxidation of the annealed samples at 1050 °C for 3 h was performed to form 3C-SiC NCs embedded in SiO_2 films (**Figure 1.7**). This is made possible due to the very slow oxidation kinetics of SiC compared to Si.

In-situ ion beam synthesis in silicon at 450°C has also been used to form nanosized SiC precipitates of diameter d=4-5 nm [22]. The SiC precipitation during dual-beam (Si^+ and C^+) synthesis is found to depend on the ion energy of the second beam and on the implantation mode, simultaneous or sequential. The additional Si^+ ion beam can either stimulate or delay the SiC precipitate formation. For suitable implantation conditions, simultaneous dual-beam synthesis can improve the in-situ SiC formation in comparison to the single-beam synthesis. A higher density of SiC precipitates with better crystal quality was observed, whereas their size was not changed.

It should be noted that co-implantation of Si and C in SiO_2 followed by annealing could not demonstrate the formation of SiC NCs, despite obtaining blue emission bands in photoluminescence (PL) [23].

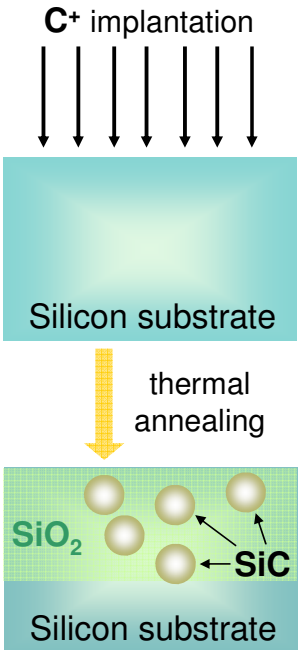

Figure 1.7: *Schematic representation of ion implantation technique.*

1.2.4. Pyrolysis

This technique is based on the use of an infrared CO_2 laser beam focused on a wall subjected to a flow of reagents in a controlled atmosphere. In these conditions, there is a transfer of energy to the precursors, causing a rise of temperature in the reaction zone, a dissociation of the precursors and the appearance of a flame in which NPs are formed without interaction with the walls of reactor (**Figure 1.8**).

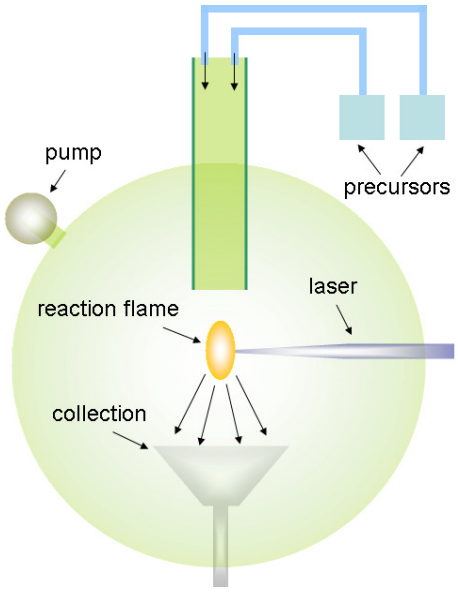

Figure 1.8: *Operation principle of laser pyrolysis.*

This method was employed to grow small SiC NPs in a flow reactor by CO_2 laser pyrolysis from acetylene (C_2H_2) and silane (SiH_4) mixture [24]. The crystal structure, composition and size of NPs can be modulated by the flow of reactive gases and the laser power. Whatever the laser power used for the synthesis, the mean grain size was very close to 10 nm, as can be seen in **Figure 1.9**. However the presence of crystallites about 2–3nm large can also be found in the powder synthesized with a high laser power (600 W).

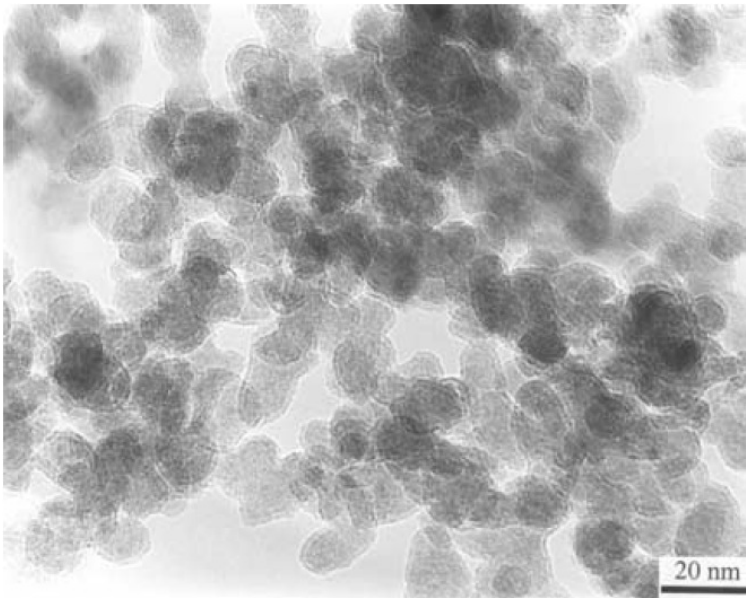

Figure 1.9: *TEM image of the SiC powder showing slightly agglomerated 10 nm SiC grains [24].*

The control on the grain growth via the laser pyrolysis technique can be carried out by different diameter of an inlet nozzle through which the precursors flow is introduced in the reaction chamber [25]. The comparison of SiC nanopowder produced in two preparation conditions is demonstrated in **Figure 1.10**. One can see that the enlargement of the nozzle leads to the growth of larger particles.

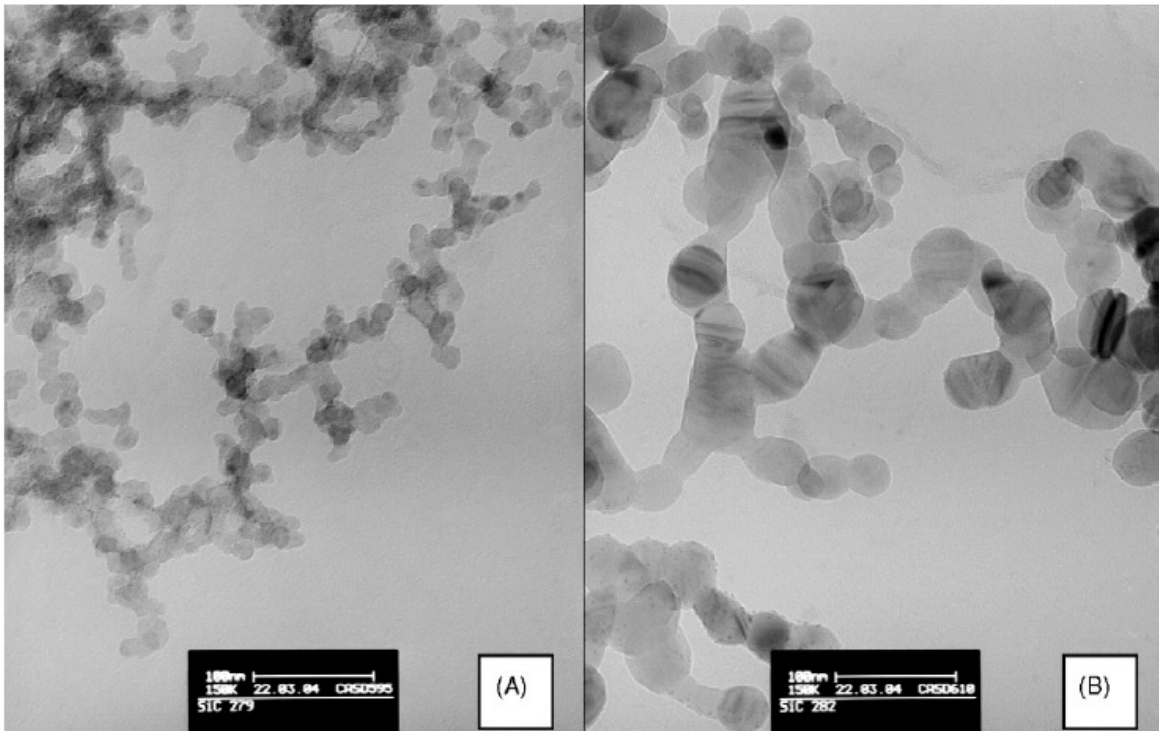

Figure 1.10: *TEM images of SiC nanopowders: (a) small and (b) large grains. Scale is 100 nm on both pictures (white line) [25].*

1.2.5. (Electro-)chemical etching

The electrochemical and electroless chemical etching are simple, efficient and inexpensive methods for SiC nanostructures production.

The diagram of the electrochemical anodization using a standard cell is shown in **Figure 1.11**. Etching leads to the electrochemical dissolution of SiC in a solution containing strong acids (HF for example). SiC is dissolved in the presence of the acid by passing an electric current between the interface of SiC and the electrolyte. This reaction is only possible by providing electrical carriers (holes) at the interface and then working with SiC as the anode, hence the term electrochemical anodization. In some cases, particularly for n-type materials, anodization takes place under UV illumination to generate holes at the semiconductor-electrolyte interface. The resulting porous structure is composed of interconnected NPs. Depending on manufacturing conditions, sizes range from nanometres to tens of nanometres. The main parameters, which can influence structure of the nano-SiC are the following: electrolyte concentration and composition, etching current, substrate type and doping level.

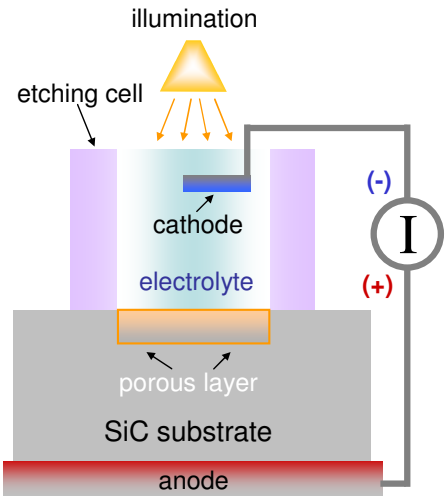

***Figure 1.11**: Operation principle of electrochemical etching.*

Rittenhouse et al. [26] can be cited for an example of SiC nanostructure fabrication by this method. A silicon carbide wafer of 6H-SiC (n-type wafer, ρ=0.45 Ω*cm) was used. The wafer was cut and polished on-axis to expose the (0001) Si plane. A two-layer metal film of Ti (10 nm) followed by Pt (220 nm) was applied to make electrical contact. The SiC was placed in a poly(tetrafluoroethylene) electrochemical cell, along with a Pt wire counter electrode and a saturated calomel reference electrode. The SiC was illuminated by UV light for the duration of etching (80mA/cm^2) in dilute HF (5%) solution. The SEM image of the resulting porous-SiC can be seen in the **Figure 1.12**. The top surface of each porous-SiC wafer is composed of nanofingers of SiC arranged randomly. In cross section, the porous SiC layers consistently show pitting with a dominant triangular shape. The porous-SiC NCs have an average diameter ~25 nm.

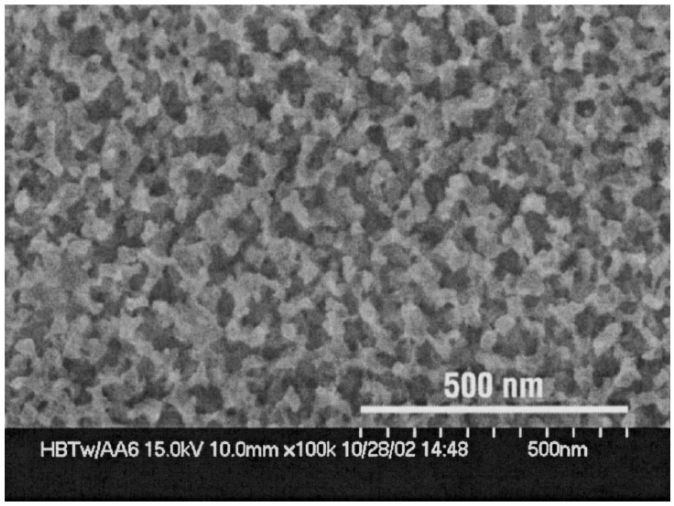

***Figure 1.12**: SEM image of porous-SiC prepared from n-type 6H-SiC [26].*

The same technique was used to fabricate SiC NPs by transformation of electrochemically etched porous-SiC into colloidal suspensions. For example, at the initial stage, Wu et al. [27] used highly catalyzed electrochemical etching of polycrystalline 3C-SiC wafer in HF-ethanol ($HF:C_2H_5OH$ = 2:1) solution. Additional illumination with a 150 W halogen lamp from a distance of 15 cm supplied reaction with holes. The anodic time was 60 min and the etching current densities 60 mA/cm^2. Finally, porous SiC was then transferred to an ultrasound water (or toluene) bath, in which the top porous structure film was crumbled into small NCs dispersed in the solvent. TEM taken by dripping the suspension on a graphite grid can be seen in **Figure 1.13**.

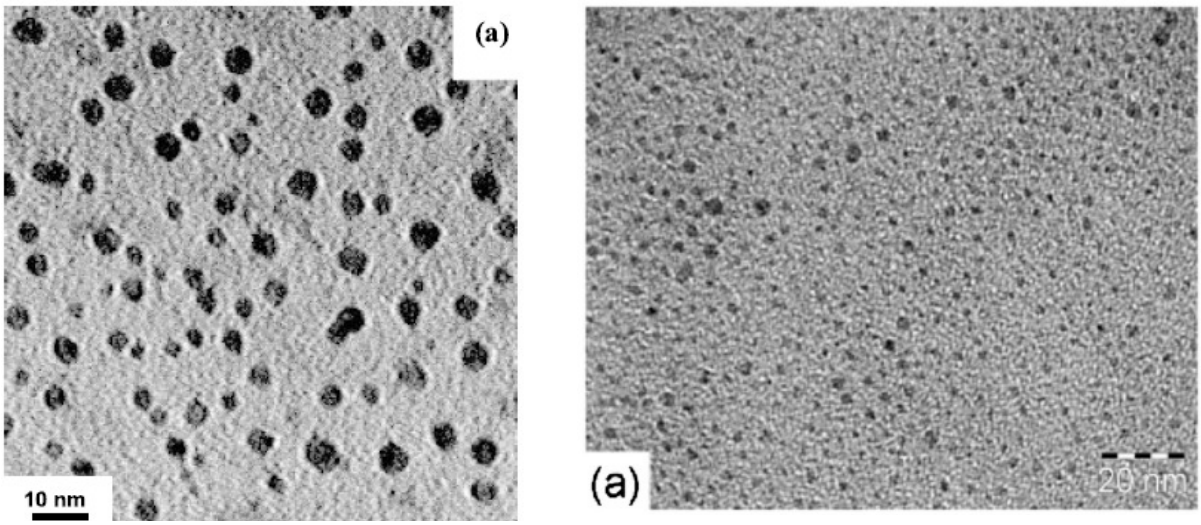

(a) (b)

***Figure 1.13**: TEM images of: (a) SiC nanopowder (Figure 1a from [27]), and (b) evaporated suspension of SiC NPs (Figure 1a from [28]).*

Similar approach proposed by Botsoa et al. [28] allows formation of dry SiC nanopowder by simple dry grinding of the formed free porous layer. Low resistivity grade (<1

Ω*cm) bulk 3C-SiC polycrystalline wafer was implemented in the preparation. The etching process took place for 3 h under UV illumination at a current density of 25 mA/cm^2 using a 1:1 HF (50%)/ ethanol electrolyte. After the etching, a highly porous network constituted by interconnected 3C-SiC NCs was formed. The ultraporous layer was then naturally dried in ambient air and afterwards removed from the wafer. The 3C-SiC nanopowder obtained by grinding can be easily dispersed in different polar solvents. TEM image of the NPs deposited on a graphite grid by evaporation of a part of the colloidal suspension can be seen in **Figure 1.13b**. Here again the presence of ultra-small NPs can be observed.

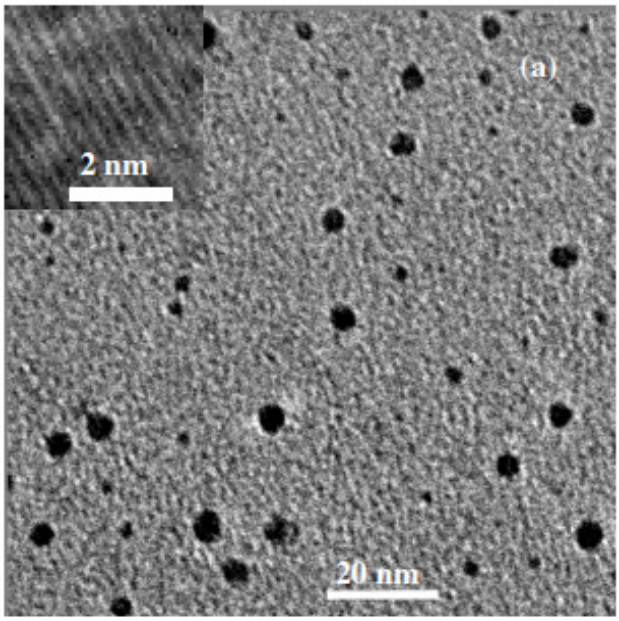

***Figure 1.14**: TEM image of the 3C-SiC NCs suspended in ethanol (Figure 1a from [29]).*

For the electroless chemical etching strong oxidizing agent is needed (HNO_3 acid for example), which primarily dissolves SiC to form some interconnected nanostructure network. Afterwards, HF removes the silicon oxide formed during the oxidization. Promising results, regarding direct preparation of bulk quantity 3C-SiC NCs by this technique starting from SiC powders was reported by Zhu et al [29]. The acids used for the fabrication was 65% nitric acid (HNO_3) with the volume of 25 ml and 40% hydrofluoric acid (HF) with the volume of 75 ml. The sizes of the as-prepared 3C-SiC NCs are smaller than 6.5 nm and have a centric distribution with the maximal probability of 3.6 nm (**Figure 1.14**). Spectral analysis and microstructural observations show that the chemical etching leads to the formation of a weakly interconnected nanostructure network in the large 3C-SiC grains and subsequent ultrasonic vibration crumbles the interconnected network, forming small-size 3C-SiC NCs.

1.3. Optical properties of SiC nanostructures

Nanoscale engineering of SiC allows considerable extension of its basic physicochemical properties. The increase in surface area to volume ratio alters a wide range of mechanical, thermal, electrical and optical properties of the material. The nonlinear properties of the nanostructured SiC can also be significantly enriched by strong dependence on defects and small deviations from the symmetric shape as well as from broken symmetry at interfaces. Additionally, quantum mechanical effects can modify the electronic properties of solids when the size of the system decreases. This effect is not observable by going from macro to micro dimensions. However, depending on the material, quantum effects become significant when the nanometer size range is reached, typically for dimensions of 100 nanometres or less.

1.3.1. Luminescence mechanisms

Luminescent properties of silicon carbide nanostructures have been subject to both theoretical and experimental studies for more then 20 years. In the early stages, the origin of the observed light emission was not clearly identified. Depending on the fabrication conditions and sample treatment it was possible to obtain PL widely ranging all over the ultraviolet and visible spectrum. The main mechanisms for the observed PL signals in below and above bandgap spectral regions have been generalized to radiative recombinations via localized (surface/defect) states and due to quantum size effects, respectively.

1.3.1.1. Localized energy states

For bulk semiconductors, the break of the crystal lattice on the boundary is at the origin of new surface-localized electron energy levels within the energy bandgap. Similar localized energy levels can be introduced onto the surface or in the volume by the extrinsic impurities or defects.

As expected, first results on the nanostructured porous SiC obtained by electrochemical etching with the luminescence below the bandgap was discussed as related to localized energy states [26, 30-33].

Studies performed by Matsumoto et al. [30] note shift of the PL peak in the higher energies and 100-fold enhancement of the intensity in comparison with the bulk material. However peak wavelength was around 460 nm , i.e. below the bangap of crystalline 6H-SiC. With increasing porosity PL intensity became stronger and decay rate slower, suggesting

dominant role of the surface in the observed PL. In this way, the emission was due to the recombination of photogenerated charge carriers in the crystalline core which are transferred to the surface where they recombined via surface states.

Furthermore, in the work of Konstantinov et al. [31] it has been shown that PL of porous SiC demonstrates a clear independence of the band-gap energy of a particular SiC polytype and applied photoexcitation. The proposed origin of the PL is believed to be related to surface defect centres or the carbon-rich phase on the SiC surface produced by the HF attack. Additional surface modification confirmed this hypothesis, when thermal oxidation at 700 ^{o}C in the oxygen atmosphere completely quenched PL, and was partially recovered by HF etching of the oxidized layer.

Some additional surface related PL mechanisms in nanostructured SiC include radiative recombination via surface C-H bonds [33], defect states at the interface between SiC and SiO_2 matrix [34]. In case of colloidal suspension of SiC NCs, luminescence peak at 510nm is attributed to the H^+ and OH^- dissociated from water and attached to Si dimers on the modified (001) Si-terminated portion of the SiC [35].

It is worth noting that extrinsic surface-localized chemical complexes or molecules can not be necessarily characterized by the electronic transition with energies below the bandgap. In this case, the electronic gap is obtained as the difference between the lowest unoccupied molecular orbital (LUMO) and the highest occupied molecular orbital (HOMO) eigenvalues, manifesting photon emission with both under and above bandgap gap energies. Such surface-related optical response is significantly enhanced in nanostructures due to above-mentioned increase of surface area to volume ratio. This in turn can complicate the assignment of the luminescence to the quantum size effects or the surface-localized chemical complexes.

Alternatively to mechanisms of PL via surface states, the recombination via impurity levels have been proposed in the luminescence of porous 6H-SiC. The work of Botsoa et al. [36] illustrates this hypothesis. The PL experiments were done on the porous and bulk 6H-SiC of n-type. The bulk materials contained donor nitrogen impurities partially compensated by aluminum. The PL of bulk material under vacuum and at low temperatures mostly reflected electronic transitions between donors-acceptors (N-Al) centred at 2.65eV. At room temperature, the N–Al donor-acceptor peak is quenched due to the ionization of the N donor by thermalization. The results of PL measurement on porous 6H-SiC also show presence of the peak around 2.65eV at low temperature. Thus, authors have attributed the origin of PL to the same mechanisms as to in bulk materials i.e. to electronic transitions via impurity levels of

donors and acceptors. To explain increased signal in porous material, additionally to the role of the increased surface to volume ratio, authors described idea of spatial confinement [37]. In this term, the spatial limitation of the NC volume in which radiative recombination takes place can lead to the increase of quantum efficiency of the luminescence process.

For 3C-SiC nanorods synthesized via catalyst-assisted pyrolysis of a polymeric precursor intensive sharp PL at 3.3 eV is observed [38]. After structural characterization, the authors attributed the emission to threefold stacking faults, which structurally resemble 6H-SiC nano-layers of 1.5 nm embedded in a 3C-SiC matrix.

1.3.1.2. Quantum confinement energy levels

Before the demonstration of the experimental manifestations of quantum confinement effects in SiC nanostructures, one should remind main concepts of quantum mechanics in confined systems.

In general, the confined systems are systems where particles (generally electrons and holes) are localized in one or several dimensions: quantum well (1D localization), quantum wire (2D) and quantum dot (3D). The effects of quantum confinement are present when dimensions become comparable to the de Broglie wavelength of the charge carriers. In these confined systems, energy of electronic states increase with confinement. There is also Coulomb interaction between electron and hole forming quasi-particle called “exciton”. Significant shift is observed when Bohr radius of the exciton r_{ex} (the sum of Bohr radius of electron r_e, and Bohr radius of hole r_h) and NC radius (R) are comparable.

Three regimes can be defined as the function of these values: 1) low confinement regime, when $R>r_e,r_h$, 2) moderate confinement regime, when $r_h<R<r_e$, and 3) regime of strong confinement, when $R<r_e,r_h$. Bohr radius, $r_{e,h}$ of hole or electron is defined by following formula:

$$r_{e,h} = \varepsilon\left(\frac{m_0}{m^*_{e,h}}\right) r_0 \qquad (1.1)$$

,where :

ε : relative permittivity

m_0 : mass of electron

r_0: Bohr radius of hydrogen (0.053 nm)

$m^*_{e,h}$: effective mass of electron or hole (taking into account mass anisotropy and light/heavy holes)

In the table 1.2, the values for effective mass of electrons and holes for three SiC polytypes with the calculated values for Bohr radius are represented [39].

Polytype	$\mathbf{m^*_e}$	$\mathbf{m^*_h}$	$\mathbf{r_e}$	$\mathbf{r_h}$	$\mathbf{r_{ex}}$
3C-SiC	$0.35m_0$	$1.26m_0$	1.47nm	0.41nm	1.88nm
4H-SiC	$0.37m_0$	$2.65m_0$	1.39nm	0.19nm	1.58nm
6H-SiC	$0.71m_0$	$2.71m_0$	0.72nm	0.19nm	0.91nm

Table 1.3: *Effective masses for electrons and holes with calculated Bohr radius for electrons, holes and excitons.*

The solution obtained from Shrodinger's equation for the particle confined in the quantum box (3D localization) represents the discretisation of electronic states expressed by this formula:

$$E_{n_x,n_y,n_z} = \frac{\hbar^2\pi^2}{2m^*}\left[\left(\frac{n_x}{d_x}\right)^2 + \left(\frac{n_y}{d_y}\right)^2 + \left(\frac{n_z}{d_z}\right)^2\right] \qquad (1.2)$$

,where

m^*: effective mass of the particle (supposed to be the same in all directions)

d_x,d_y,d_z: size of the quantum box in the X,Y and Z directions

n_x,n_y,n_z: quantum numbers in the corresponding directions

In the NCs of semiconductors, the quantum confinement effects lead to drastic increase of band-gap in comparison to bulk material. Further, the increased overlap of wave functions of the electrons and holes increase the probability of radiative recombinations. From the Heisenberg uncertainty principle ($\Delta x \Delta p \geq \frac{\hbar}{2}$), spatial localization of the particle leads to higher uncertainty in momentum of the particle. In this way, indirect electronic transitions become more probable.

There are several theoretical studies of bandgap values in the SiC nanostructures. The dependence of the bandgap in the porous 6H-SiC as the function of size was determined for quantum dots (QDs), quantum wires and quantum wells [40]. The correct values of the energies for electrons and holes are obtained from Shrodinger's equation for one, two or three dimensions. These values are added to the value of bandgap of bulk material in order to

obtain transition energy thus effective value for bandgap in the NCs. The results of this evaluation can be seen in **Figure 1.15**. One can clearly see that particles with sizes lower than 3 nm present drastic change of bandgap, while this effect is lower for particles of sizes from 4 to 7 nm.

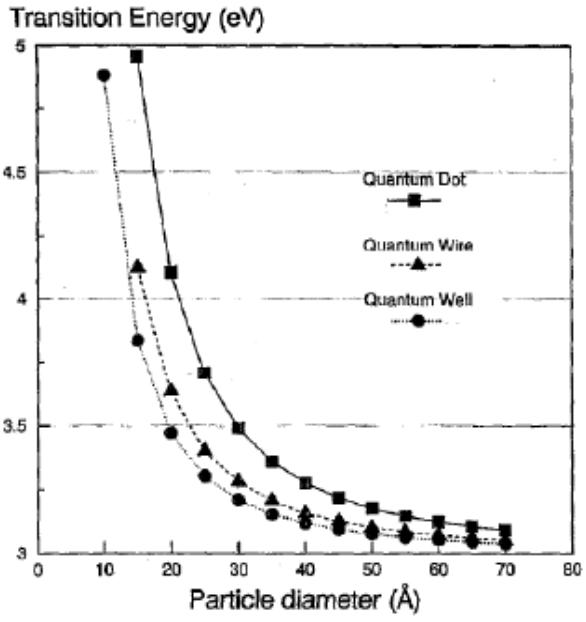

***Figure 1.15**: Transition energy versus structure size in porous 6H-SiC [40].*

Taking into account Coulomb interaction between electron and hole, the solution of Shrodinger's equation for the particle in spherical potential well according the model of Brus [41], is as following:

$$E_g^* \approx E_g + \frac{\hbar^2 \pi^2}{2d^2}\left[\frac{1}{m_e^*} + \frac{1}{m_h^*}\right] - \frac{1.8e^2}{4\pi\varepsilon_0\varepsilon_r d} \qquad (1.3)$$

,where:

E_g: bandgap of the bulk material

$m^*_{e,h}$: effective mass of electron or hole

d: diameter of the NP

e: charge of electron

ε_r : relative permittivity

ε_0 : vacuum permittivity

The second component (d^{-2}) in the equation is the addition of the confinement energies for hole and electron. The last component (d^{-1}) corresponds to the Coulomb interaction, which exists between electron and hole. **Figure 1.16** presents the variation of the excitonic bandgap as the function of the radius of 3C-SiC NCs [42]. The bandgap increases when the size of NPs

decreases, and this increase is evident when size is under 4 nm. The existence of the stable excitonic states has been shown at the ambient temperature due to strong coupling in electron-hole pair. In contrast, in the bulk materials, the excitons are observed only at the low temperatures.

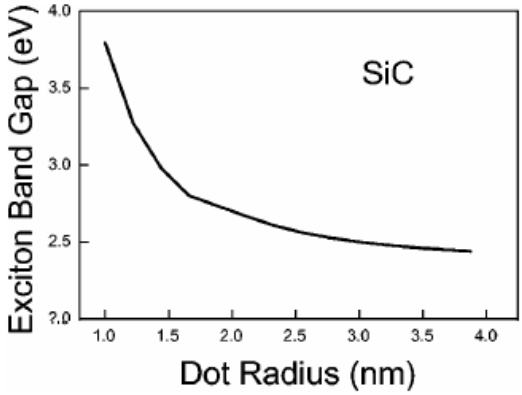

***Figure 1.16**: Exciton band gap as a function of dot radius for 3C-SiC QDs [42].*

Another theoretical work has been performed for SiC NPs with diameters between 1 and 3 nm [43]. This ab-initio computational study has been done using density functional theory in the approximation of gradients of Perdrew, Burke and Emzerholf. The 3C-SiC core was considered for every dot, however six different surface geometries are investigated: three different terminations (C, Si, or Si-rich), and two different surface structures, i.e., ideally terminated or reconstructed (100) facets (with dimer formation). In the case of dots large enough to accommodate more complex reconstructions (i.e., with radius larger than 1.1 nm), authors also considered a (3×1)-like reconstruction of (100) facets. **Figure 1.17** represents the variation of the bandgap for these clusters with different terminations; the gap here is the energy between HOMO and LUMO. The results of the calculations show that even when the gap increase with the decreasing NP radius, the surface structure still plays dominant role. In general, the dots with C or H terminations have bandgap values slightly higher. The smallest bandgaps correspond to the QDs with Si or Si-rich terminations.

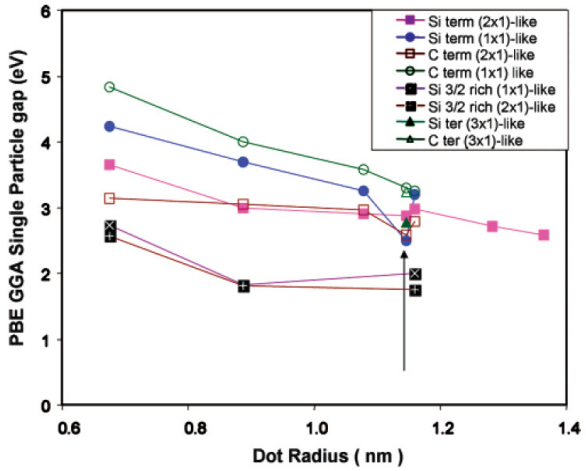

***Figure 1.17**: Single-particle electronic gap of SiC QDs as a function of size for different surface structures [43].*

Similar theoretical approach was used by Peng et al. [44], to study band-gap variation of spherical SiC nanoclusters with dimensions up to 2 nm from bulk 2H, 3C, and 4H polytype crystals. As can be seen in **Figure 1.18**, for clusters larger than 1 nm, the variation of the energy gap with size is a strong function of the polytype. In contrast, for smaller clusters (<1 nm), no distinct differences in the energy gap are observed among the polytypes. This critical size of 1 nm is correlated by authors with the number of bilayers and the stacking sequences within the clusters.

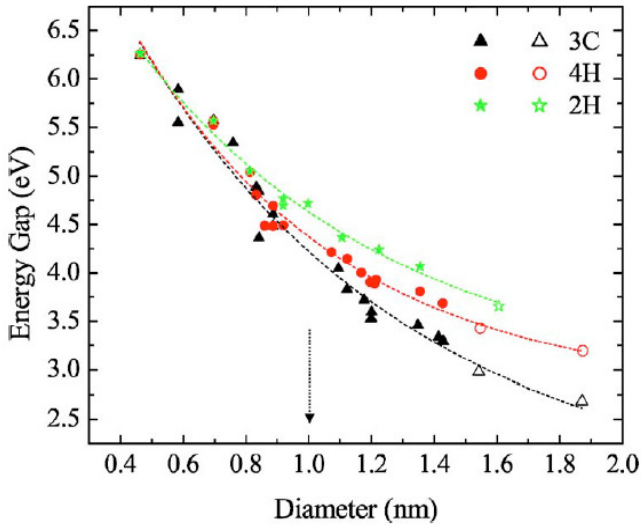

***Figure 1.18**: The variation of the DFT HOMO-LUMO gap with size for 3C (black triangles), 4H (red circles), and 2H (green stars) SiC nanoclusters. The solid data points are the energy gaps of the relaxed clusters. And open data points refer to the gaps of larger geometry-unrelaxed clusters [44].*

One of the first experimental indications on the quantum confinement effects in nanostructured SiC were demonstrated by Chor et al [40]. Authors observed appearance of the UV luminescence peak in emission spectrum of porous 6H-SiC obtained only at certain threshold anodization currents. It was assumed that at higher anodization current densities, small crystallites are formed in porous SiC, resulting in quantum confinement. However, it was also supposed that the luminescence can be associated with native SiO_2 layer of porous SiC.

Clear evidence of quantum confinement effects in 3C-SiC NPs was reported recently by Wu et al [27]. The measurements were performed on the colloidal suspensions of 3C-SiC. The emission spectrum maximum of NCs in the suspension has been shifted from 440 nm to 560 nm when wavelength of the excitation increased. In the same time, as predicted by quantum confinement, the PL intensity shows dependence on the excitation wavelength. In other words, authors have found the correlation between a centric distribution of maximal PL intensity with the size distribution of the NCs.

In another studies [45, 46] Fan et al. explain the absence of detectable luminescence in porous SiC due to the following limitations. Electrochemical etching leads to a structure

which combines quantum-sized SiC crystallites interconnected with large ones. Thus, charge carriers can easily be transferred to the latter ones, where they recombine, limiting appearance of above bandgap emission. However, when porous SiC crumbles into colloidal SiC NPs role of the surface or defect states of large particles is reduced.

In case of 6H-SiC NPs obtained by electrochemical etching method, Botsoa et al. [36, 47] reported similar findings. Initial highly concentrated suspension of nanoparticles demonstrated under bandgap emission attributed to the surface states and N-Al donor-acceptor recombination channel. However, when the suspension was diluted, PL peak position was blue-shifted revealing clear evidence of quantum confinement. It was explained that the dilution of the colloidal suspensions containing SiC NPs leads to the decrease of the probability of "instantaneous interconnections" between NPs, hence favoring the luminescence from quantum-confined excitons in smaller NPs. Similar blue-shift is observed when the suspension was centrifuged. In this way, the centrifugation technique allows efficient separation of the smallest NPs exhibiting quantum confinement from large ones where radiative transitions between the impurity electronic states dominate.

Other fabrication methods, like chemical etching of microscale 3C-SiC grains [29] and laser ablation in reactive liquid [15], have also been efficiently used to fabricate ultra-small particles with PL related to the quantum–size effects.

1.3.2. Nonlinear phenomena

At least two main groups of nonlinear phenomena have been reported to be influenced by nanostructuration and thus dependent on the size of the material. Firstly, second-harmonic generation (SHG), physical process observed in materials with non-zero second-order nonlinear susceptibility. Secondly, physical processes of four-wave interaction, which is described in terms of third-order susceptibility.

Photoinduced SHG (PISHG) of SiC NCs (with sizes ranging from 10 to 30 nm) incorporated into a photopolymer matrix was investigated by Kityk et al. [48, 49]. The SiC nanopowders were synthesized by a CO_2 laser pyrolysis from a gaseous mixture of SiH_4 and C_2H_2. It was shown that depending on the sample preparation, hexagonality (ratio of hexagonal to cubic structural components in the SiC NCs) can be controlled. An increase in the degree of hexagonality was found to cause increase in the PISHG. It was confirmed by calculations, suggesting key role of hexagonal substructures in the observed photoinduced effects. On the other hand, the analogous measurements on SiC nanocrystalline films have

shown that the maximal output SHG signal was five times less. Therefore the large contribution in the appearance of the local non-centrosymmetry belongs also to guest-host interfaces. This causes hyperpolarizabilities considerably higher than those for bulk-like crystals, as for those which appear in polymer-like molecules. These factors were considered to explain certain discrepancies from theoretical PISHG data.

Electro-optical (EO) effect in preliminary stage was experimentally demonstrated by Boucle et al. [50] in large-sized (10 and 30 nm) SiC NCs incorporated in poly(N-vinylcarbazole) (PVK) blended with coumarin (MK). Effective electro-optical parameters of the order of r_e~1 pm/V were measured and seemed to be governed by the polymer/SiC-NC interface, as well as by the local non-centrosymmetry in hexagonal 6H–SiC and cubic 3C–SiC structures involved in SiC-NC. Authors emphasized that the macroscopic second order optical susceptibilities, which are involved in the electro-optical response, are connected with the interface between the NC and the polymer matrices. At this level, reconstructed SiC surfaces, in the thickness range of the nanometer, are involved at the particle surfaces, leading to a planar quantum confined structure at the border between the nano-SiC and the polymer matrix. Thus, the increase of the second order nonlinear susceptibilities comes from the large number of trapping levels created by large reconstructed surface of SiC particles, and also from the difference between the electronic structures involved at the particle boundaries. The size effects were investigated by comparing the EO response from large-sized NC (30 nm) and less extended ones (10 nm). A similar behavior was obtained and in this way indicated that the size confinement is not manifested in the EO responses. This is mainly due to the NC sizes higher than the exciton Bohr radius. Further, in order to point out role of the host polymer and SiC NC interfaces, Boucle et al. [51] performed the comparison of the EO responses in different polymer host matrices (PMMA and PVK). As the result, effective EO parameters up to 26 pm/V were achieved in PMMA. In the later study Boucle et al. [52], also pointed out, that the presence of dangling bonds in the carbon-rich phases on the surface might lead to strong enhancement of the local hyperpolarizabilities in comparison with silicon rich particle surfaces. Thus, the role of surface reconstruction of SiC NCs is very important.

In another investigation Konorov et al. [53] have studied second- and third- harmonic generation in silicon carbide nanopowders embedded in a PMMA film. The second- and third-harmonic yields are shown to display an anomalous, counterintuitive behaviour as functions of the SiC nanopowder content in a polymer film. Whereas harmonic generation in polymer films with a high content of SiC NCs was quenched by the absorption of agglomerating NPs, the influence of absorption was less detrimental in nanocomposite films

with a lower SiC content, leading to the growth of the second- and third-harmonic yields. Further, Konorov et al. [54] experimentally studied second- and third-harmonic generation in the regime of weak scattering, with the NPs diameter D, the elastic scattering length l, the radiation wavelength λ, and the film thickness L meeting the relations D<< λ <<l~ L. The strong wavelength dependence (**Figure 1.19**) of diffuse second- and third-harmonic generation observed under these conditions indicates a significant role of scattering effects in nonlinear optical interactions in nanopowder materials, which allows diffuse harmonic generation to be controlled by varying the ratio of the characteristic size of the NPs to the wavelength of the pump radiation. When the pump wavelength λ=1.35 μm, and D=50 nm, the elastic scattering length l =300 μm exceeds the film thickness (L=200 μm). However, for the pump wavelength reduced to λ=1.15μm, the elastic scattering length, estimated for this wavelength was l ~150μm, thus, becomes less than the thickness of the nanopowder film. The authors claim that the role of scattering is thus to save pump photons for diffuse harmonic generation.

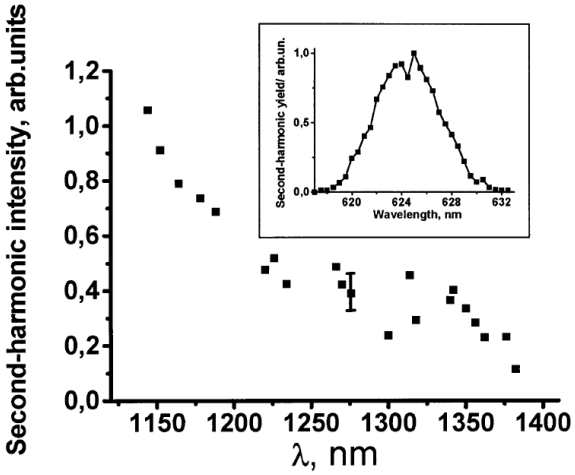

***Figure 1.19**: The intensity of the second harmonic generated in a 200-μm- thick SiC nanopowder film by 100-fs OPA pulses as a function of the wavelength of the OPA radiation. The inset shows a typical spectrum of the second harmonic [54].*

In the investigations of nonlinear refraction, Borshch et al. [55] used nanocrystalline SiC films obtained using a method of direct deposition of carbon and silicon ions with a mean energy of 90–100 eV at low substrate temperatures (900 to 1150 ° C). These structures show that the nonlinear response in SiC NC is much larger (by four orders of magnitude) than that in single-crystal SiC (the nonlinearity coefficient of the refractive index n_2 reaches 1.7×10^{-5} esu and the corresponding real part of nonlinear susceptibility $\chi^{(3)}$ was 3.5×10^{-6} esu). Obtained results are discussed in terms of nonlinear optical response enhancement in a nanocrystalline SiC film caused by the quantum confinement effect. In addition, since a nanocrystalline SiC film has a very developed interface surface between SiC NCs, a large number of defect surface centers, including shallow donors, appear; these are sources of

conduction electrons. That is to say, when conduction electrons excited by laser radiation are involved in intraband transitions, their effective mass, mobility, and the type of scattering of the carriers change, leading to modification of nonlinear response of the material.

The abovementioned considerations and explanations do not provide however any unified information on the size-dependent nonlinear properties of nano-SiC, especially in quantum confinement regimes. The main limitations arise from still much larger than the Bohr radius NCs present in the samples and from significant role of SiC surface state in nonlinear response. The later one should not be underestimated since it can give drastic increase of nonlinear response even in centrosymmetric bulk materials where the second-order susceptibility term $\chi^{(2)}$ is close to zero. For example, in case of nanostructured silicon [56-58], the earlier reported SHG and two-photon excited PL are mostly caused by the broken crystalline symmetry at interfaces and shape irregularities.

Contrary to the SiC, both theoretical and experimental evidence of the quantum confinement effects role (in strong and weak confinement regimes) on the third order nonlinearity have been reported for variety of materials. These studies can give indications on the expected size-dependent tendencies of nano-SiC. From one side it was predicted that increased nonlinearities can be observed with decreasing QD size [59, 60]. In this case infinite distribution redistributed in discrete energy transitions was discussed to be the main reason of the enhanced nonlinear properties. However, there are also reports showing that smaller dots have smaller $\chi^{(3)}$ in case of CuBr [61], ZnO [62], CdSe and CdTe [63]. These findings mostly based on two-photon absorption experiments, are explained by the decrease in the density of states with increasing quantum confinement that overcompensates the increasing oscillator strength of a single two-photon transition as the QD is reduced in size. Recently it has also been shown that for PbS QDs [64] increasing nonlinearity in comparison with bulk material can be observed for smaller QDs even after volume normalization. Obtained results are explained through a combination of strong quantum confinement and highly symmetric distribution of conduction and valence band states in PbS QDs that results in an accumulation of allowed two-photon transitions in narrow spectral regions.

The role of quantum confinement in second harmonic generation process was elucidated, for example by Winter et al [65]. It was shown that under similar excitation conditions, the $\chi^{(2)}$ of ~11.5 nm CdTe QDs can significantly exceed that of the corresponding bulk material. It was suggested that quantum confinement effects do play an important role in SHG and Hyper-Rayleigh scattering (noncoherent second-order nonlinear process). An intuitive physical explanation to this trend was brought by considering the two quantities

affecting the nonlinear susceptibility. Firstly, under two photon resonant excitation of QDs, the density of states clearly increases with a higher excitation frequency, tending to increase the nonlinear susceptibility. However, a higher density of states also implies more rapid decoherence, which has the inverse effect on $\chi^{(2)}$. Thus, authors highlight that the trade-off between these two processes, which dictates the optimal excitation frequency, might be found for different materials.

1.4. Multidisciplinary applications

The great interest that SiC has gathered in latest years is due the possibility to combine in one single material good semiconducting and chemical properties, biocompatibility and sensing potentiality. SiC chemical inertness, wide bandgap, tribological properties and hemocompatibility make it a very promising candidate for biosensors, interface with biological tissues and lab-on-chip medical devices. Moreover, the possibility to realize nanostructures opens the possibility to assembly novel nanoscale devices and arrays by the bottom-up approach, and to enhance the sensing capabilities of the material thanks to the high surface/volume ratio. Low dimensional SiC may exhibit distinctive electronic, optical, thermal and chemical properties, as well as carrier quantum confinement. Many one-dimensional structures have proven to exhibit better properties than the same material with bulk size, and this would permit to combine appropriate building blocks to obtain unique functions, or combinations of functions, in integrated nanosystems [66].

Here, only few of the most notable applications of nano-SiC will be cited. Range of application and issues arising in case of SiC nanowires (NWs) were discussed recently by Zekentes et al [67]. The study of mechanical, thermoelectric and hydrophobic properties of SiC NWs is limited and additional work is necessary towards their complete description, which is necessary for evaluating their potential for related applications. Moreover, there is a series of quality criteria with different weight factors for each application.

Nanowire field effect transistor. For nanoelectronic applications the carrier concentration and mobility should be accurately controlled along the NW. The first experiments on 3C–SiC based NWFETs [68] revealed that the carrier concentration is too high, due to unintentional doping, resulting in very low electron mobility. Possible causes for these high residual doping values are impurities contamination and/or large number of extended defects. It seemed difficult to obtain monocrystalline SiC NWs without extended defects like staking faults and low residual doping with the low cost ‘chemistry-driven’ methods used up to now. Relatively

high cost methods (molecular beam epitaxy, high-purity CVD, etc) used in semiconductor device technology should be used towards the aim of SiC NWFETs fabrication.

Reinforcement coating. For other applications such as mechanical reinforcing these issues of mobility and residual doping are not so critical. Instead of high-quality-crystal production, a high growth method throughput and large length-to-diameter ratio are demanded. The first results related to the use of SiC NWs as reinforcing material are very promising showing a realistic industrial perspective especially for operation at high temperature and/or oxidizing environments [69, 70].

Field emitters. Nanostructures are offering intrinsic advantages for the fabrication of field emitters (FE). In general, for FE applications, a high aspect ratio is highly desirable to obtain a low threshold voltage for emission. In the case of NWs, this aspect ratio is considerably increased compared with bulk materials. Apart from the geometry of the material, another important parameter is the low electron affinity that permits the emission of electrons for lower applied electric fields and leads to higher emission current density. Moreover, the superior chemical and physical stability of SiC would result in a longer lifetime of the device by minimizing emission instabilities. SiC NWs were found to be very promising for FE applications, for example in field emission diodes (FED) and other nanoelectronic devices [71]. Authors report the fabrication of FED devices (**Figure 1.20**) with SiC-NW-based cathodes, which have demonstrated excellent FE properties at low applied voltages/electric fields and stable long-term performance. The calculations of field emission data indicate that the Schottky effect has strong influence on the field emission from SiC NW emitters.

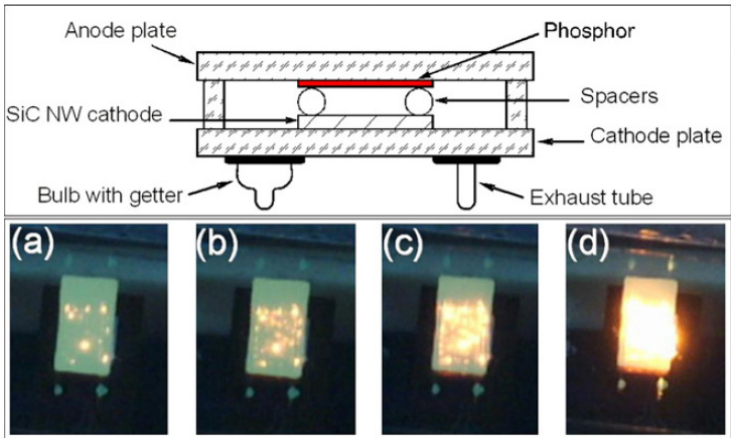

Figure 1.20*: Scheme of an FED device with SiC-NW-based cathode, and field emission (phosphor screen) images recorded at increasing electric field: (a) 2.3 V* μm^{-1}*, (b) 2.7 V* μm^{-1}*, (c) 3.0 V* μm^{-1}*, (d) 3.3 V* μm^{-1}*. The size of the SiC-NW-based cathodes is 5 mm× 5 mm [71].*

Photocatalysis. Large-scale SiC NWs coated with a trace of amorphous silicon oxide layer were synthesized by high-frequency induction heating of SiO powders [72]. Typically, a single nanowire has an average core of 8–20 nm in diameter. The photocatalytic activity of

the obtained SiC NWs was evaluated by the photocatalytic decomposition of gaseous acetaldehyde accompanied by the generation of CO_2. The result shows that the SiC NW exhibits the characteristic of an excellent photocatalyst. Furthermore, it is found that the as-synthesized amorphous SiO_2 coated SiC manifests higher photocatalytic activity than the bare SiC NWs, resulting from their stronger absorption of gaseous acetaldehyde and higher probability of trapping of an excited electron in the conductive band of SiC coated by SiO_2 while holes remain in the SiC valence band.

Bio-labelling. Recently two groups have reported application of SiC QDs for cell imaging applications [73, 28]. Botsoa et al. [28], highlighted high penetration, accumulation, and heterogeneous distribution of the bare QDs in the intracellular environment. The main advantage of the elaborated 3C-SiC QDs, over conventionally used QDs based on II-VI semiconductors is the non-cytotoxicity for in vitro analysis and their potential biocompatibility for in vivo studies. Under the UV/violet excitation, the cells marked by the QDs were very bright while the autofluorescence of unmarked cells was not visible at all. Comparison between the fluorescence micrographs and the microscope photos obtained under white light demonstrates that the fluorescing QDs are strongly localized inside the cells (**Figure 1.21**). Indeed, one can easily notice a heterogeneous distribution of the fluorescence intensity inside the cell. Since the highest intensities correspond to the position of the nuclei, it means that the QDs penetrated into the cells and preferentially concentrated at the nuclei. However, authors left the question whether the QDs entered the nucleus or were just concentrated on the outside of the nucleus membrane.

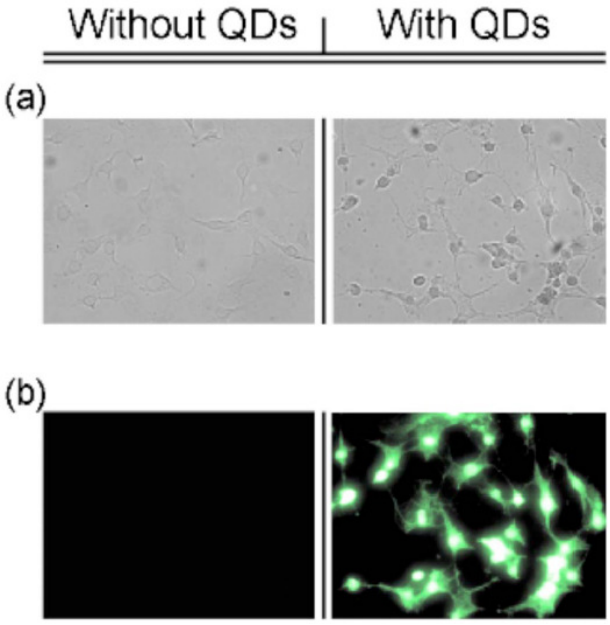

Figure 1.21*: (a) White light microscopy images (100X magnification) of biological cells not having been exposed to QDs (left column) and having been exposed to QDs (right column). (b) Corresponding fluorescence photos (100X magnification) obtained under UV/violet excitation with the same accumulation times [28].*

Nanoporous filtration membranes. Rosenbloom et al. [74] have fabricated free-standing SiC nanoporous membranes obtained by electrochemical etching in both p-type and n-type material. Authors showed that these membranes permit the diffusion of proteins up to 29000 Daltons (1Da=1.660538921×10^{-27} kg), while those of 45000 Da and higher were excluded. The size range of proteins able to cross the membranes includes many important cell signalling molecules, which tend to be small. This suggests that the material may be suitable for biosensor and other applications where permeability of small molecules and small proteins and exclusion of larger molecules is desirable.

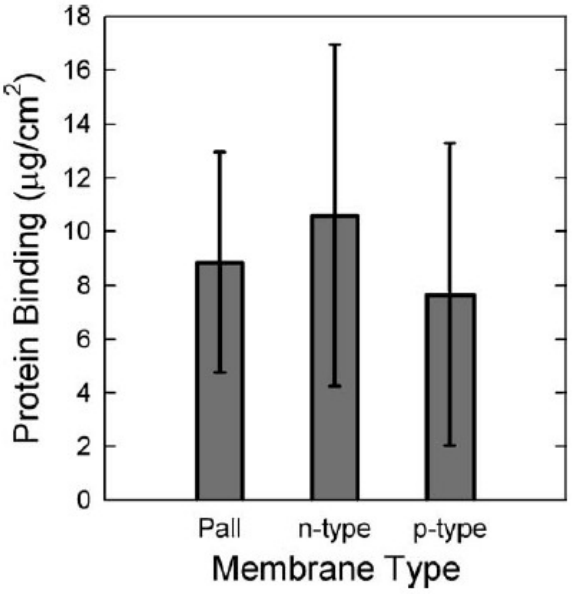

Figure 1.22*: Comparison of albumin I^{125}-labeled protein binding to porous n- and p-type SiC membranes versus the best commercially available low-adsorption polymer membrane. Error bars represent the standard deviation of 3 experiments using different samples of conventional, p-type or n-type membranes [74].*

It was confirmed that porous SiC has very low protein adsorption and comparable to the best commercially available polymer nanoporous membrane. **Figure 1.22** shows the comparative binding of radioactively labeled albumin to porous 6H-SiC (n-type and p-type) versus the Omega membrane from Pall Corporation, adjusted for the area of exposed membrane that contacted the albumin-containing solution. This resistance to protein fouling is another desirable property of this material.

Cancer treatment. Novel implementation of 3C-SiC NPs has been reported recently by Mognetti et al [75]. The authors claim about the selective influence of SiC NPs on viability and proliferation on oral squamous carcinoma (AT-84 and HSC) and immortalized cell lines (S-G). More importantly, reported cytotoxicity was higher for cancer than for immortalized cells. Since one of the limitations of classical antineoplastic drugs is their lack of selectivity, these results open a new way in the search for antiproliferative drugs.

1.5. Conclusions

In this chapter, it was shown that although the properties of the bulk phase are certainly exciting, dealing with silicon carbide at the nanoscale offers novel perspectives. Described fabrication methods ensure silicon carbide nanostructures with various sizes, composition and corresponding physical properties. Especially, the optical properties were found to be very sensitive on the sample preparation. Despite the recent announcement of a clear evidences on quantum confinement effect in 3C-SiC nanocrystals, it remains challenging to precisely control optical emission in UV-visible with a narrow size distribution of nanoparticles. Many luminescence studies carried out were reported on the samples obtained by electrochemical etching of the bulk substrates. Observed below bandgap emission was mainly assigned to the localized impurities, defect and surface states present in the SiC nanostructures. What is more, the presence of carbon-rich phase and enriched SiC-environment interfaces should not be neglected when investigating the complex linear and nonlinear optical response of the elaborated structures.

There are still theoretical and experimental works to be conducted on nano-SiC to fully realize their potential for the manufacture of stable light emitters and for nonlinear optics, while biocompatibility and hydrophilicity of the bulk material make SiC nanostructures an ideal candidate for application in biology and medicine.

1.6. References

1. MORKOC H., STRITE S., GAO G.B., et al. Large-band-gap SiC, III-V nitride, and II-VI ZnSe-based semiconductor device technologies. Journal of Applied Physics, 1994, vol. 76, no. 3, p.1363–1398.
2. SVECHNIKOV G.S., RIZIKOV I.V., IVANOV A.I. Multicolour, radiation-resistant SiC light-emitting diodes. Diamond and Related Materials, 1994, vol. 3, p.1045–1047.
3. ANDRIEVSKI R.A. Synthesis, structure and properties of nanosized silicon carbide. Reviews on Advanced Materials Science, 2009, vol. 22, p.1–20.
4. GOLDBER Y., LEVINSHTEIN M.E., RUMYANTSEV S.L. Properties of Advanced Semiconductor Materials GaN, AlN, SiC, BN, SiC, SiGe. New York: John Wiley & Sons Inc., 2001, p. 93-148.
5. PATRICK L., CHOYKE W. Static Dielectric Constant of SiC. Physical Review B, 1970, vol. 2, no. 6, p.2255–2256.
6. NIEDERMEIER S., SCHILLINGER H., SAUERBREY R., et al. Second-harmonic generation in silicon carbide polytypes. Applied Physics Letters, 1999, vol. 75, no. 5, p.618–620.
7. ADOLPH B., BECHSTEDT F. Influence of crystal structure and quasiparticle effects on second-harmonic generation: Silicon carbide polytypes. Physical Review B, 2000, vol. 62, no. 3, p.1706–1712.
8. RASHKEEV S.N., LAMBRECHT W.R.L., SEGALL B. Second-harmonic generation in SiC polytypes. Physical Review B, 1998, vol. 57, no. 16, p.9705–9715.
9. CHEN J., LEVINE Z.H., WILKINS J.W. Linear and nonlinear optical properties of four polytypes of SiC. Physical Review B, 1994, vol. 50, no. 16, p.11514–11519.
10. MOSS D.J., GHAHRAMANI E., SIPE J.E. Semi-ab initio tight-binding band-structure calculations of $\chi(3)$ (-3ω; ω, ω, ω) in C, Si, Ge, SiC, BP, AIP, AlAs, AlSb, GaP, GaAs, GaSb, InP, InAs, and InSb. Physica Status Solidi (b), 1991, vol. 164, p.587–604.
11. SHI W., ZHENG Y., PENG H., et al. Laser Ablation Synthesis and Optical Characterization of Silicon Carbide Nanowires. Journal of the American Ceramic Society, 2000, vol. 83, no. 12, p.3228–3230.
12. ZHANG H., FENG P., MAKAROV V., et al. Synthesis of nanostructured SiC using the pulsed laser deposition technique. Materials Research Bulletin, 2009, vol. 44, p.184–188.

13. WU X.J., JIA T.Q., ZHAO F.L., et al. Formation mechanisms of uniform arrays of periodic nanoparticles and nanoripples on 6H-SiC crystal surface induced by femtosecond laser ablation. Applied Physics A, 2006, vol. 86, p.491–495.
14. JIA T.Q., ZHAO F.L., HUANG M., et al. Alignment of nanoparticles formed on the surface of 6H-SiC crystals irradiated by two collinear femtosecond laser beams. Applied Physics Letters, 2006, vol. 88, no. 111117.
15. YANG S., CAI W., ZENG H., et al. Ultra-fine β-SiC quantum dots fabricated by laser ablation in reactive liquid at room temperature and their violet emission. Journal of Materials Chemistry, 2009, vol. 19, no. 38, p.7119–7123.
16. BUSCHMANN V., KLEIN S., FUEB H., et al. HREM study of 3C–SiC nanoparticles: influence of growth conditions on crystalline quality. Journal of Crystal Growth, 1998, vol. 193, p.335–341.
17. KLEIN S., WINTERER M., HAHN H. Reduced-Pressure Chemical Vapor Synthesis of Nanocrystalline Silicon Carbide Powders. Chemical Vapor Deposition, 1998, vol. 4, no. 4, p.143–149.
18. ZHANG D., ALKHATEEB A., HAN H., et al. Silicon Carbide Nanosprings. Nano Letters, 2003, vol. 3, no. 7, p.983–987.
19. XI G., PENG Y., WAN S., et al. Lithium-Assisted Synthesis and Characterization of Crystalline 3C−SiC Nanobelts. The Journal of Physical Chemistry B, 2004, vol. 108, no. 52, p.20102–20104.
20. BECHELANY M., BRIOUDE a., STADELMANN P., et al. Very Long SiC-Based Coaxial Nanocables with Tunable Chemical Composition. Advanced Functional Materials, 2007, vol. 17, no. 16, p.3251–3257.
21. CHEN D., LIAO Z.M., WANG L., et al. Photoluminescence from β-SiC nanocrystals embedded in SiO_2 films prepared by ion implantation. Optical Materials, 2003, vol. 23, p.65–69.
22. KÖGLER R., EICHHORN F., KASCHNY J.R., et al. Synthesis of nano-sized SiC precipitates in Si by simultaneous dual-beam implantation of C + and Si + ions. Applied Physics A, 2003, vol. 76, p.827–835.
23. PÉREZ-RODRÍGUEZ A., GONZÁLEZ-VARONA O., GARRIDO B., et al. White luminescence from Si^+ and C^+ ion-implanted SiO_2 films. Journal of Applied Physics, 2003, vol. 94, no. 1, p.254–262.

24. HERLIN-BOIME N., VICENS J., DUFOUR C., et al. Flame Temperature Effect on the Structure of SiC Nanoparticles Grown by Laser Pyrolysis. Journal of Nanoparticle Research, 2004, vol. 6, p.63–70.
25. LECONTE Y., MASKROT H., COMBEMALE L., et al. Application of the laser pyrolysis to the synthesis of SiC, TiC and ZrC pre-ceramics nanopowders. Journal of Analytical and Applied Pyrolysis, 2007, vol. 79, p.465–470.
26. RITTENHOUSE T.L., BOHN P.W., HOSSAIN T.K., et al. Surface-state origin for the blueshifted emission in anodically etched porous silicon carbide. Journal of Applied Physics, 2004, vol. 95, no. 2, p.490–496.
27. WU X.L., FAN J.Y., QIU T., et al. Experimental Evidence for the Quantum Confinement Effect in 3C-SiC Nanocrystallites. Physical Review Letters, 2005, vol. 94, no. 026102.
28. BOTSOA J., LYSENKO V., GÉLOËN A., et al. Application of 3C-SiC quantum dots for living cell imaging. Applied Physics Letters, 2008, vol. 92, no. 173902.
29. ZHU J., LIU Z., WU X.L., et al. Luminescent small-diameter 3C-SiC nanocrystals fabricated via a simple chemical etching method. Nanotechnology, 2007, vol. 18, no. 365603.
30. MATSUMOTO T., TAKAHASHI J., TAMAKI T., et al. Blue-green luminescence from porous silicon carbide. Applied Physics Letters, 1994, vol. 64, no. 2, p.226–228.
31. KONSTANTINOV A.O., HENRY A., HARRIS C.I.I., et al. Photoluminescence studies of porous silicon carbide. Applied Physics Letters, 1995, vol. 66, no. 17, p.2250–2252.
32. JESSENSKY O., MÜLLER F., GÖSELE U. Microstructure and photoluminescence of electrochemically etched porous SiC. Thin Solid Films, 1997, vol. 297, p.224–228.
33. HASSEN F., M'GHAIETH R., MAAREF H., et al. Morphological and optical characterization of porous silicon carbide. Materials Science and Engineering: C, 2001, vol. 15, p.113–115.
34. GUO Y.P., ZHENG J.C., WEE A.T.S., et al. Photoluminescence studies of SiC nanocrystals embedded in a SiO_2 matrix. Chemical Physics Letters, 2001, vol. 339, p.319–322.
35. WU X.L., XIONG S.J., ZHU J., et al. Identification of surface structures on 3C-SiC nanocrystals with hydrogen and hydroxyl bonding by photoluminescence. Nano Letters, 2009, vol. 9, no. 12, p.4053–4060.
36. BOTSOA J., BLUET J.-M., LYSENKO V., et al. Photoluminescence of 6H–SiC nanostructures fabricated by electrochemical etching. Journal of Applied Physics, 2007, vol. 102, no. 083526.

37. PETROVA-KOCH V., SRESELIB O., POLISSKI G., et al. Luminescence enhancement by electrochemical etching of SiC (6H). Thin Solid Films, 1995, vol. 255, no. 17, p.107–110.
38. ZHANG L., YANG W., JIN H., et al. Ultraviolet photoluminescence from 3C-SiC nanorods. Applied Physics Letters, 2006, vol. 89, no. 143101.
39. BOTSOA J. Synthèse de nanostructures de carbure de silicium et étude de leurs propriétés optiques. Lyon: INSA de Lyon, 2008, 146 p.
40. SHOR J.S., BEMIS L., KURTZ A. D., et al. Characterization of nanocrystallites in porous p-type 6H-SiC. Journal of Applied Physics, 1994, vol. 76, no. 7, p.4045–4049.
41. BRUS L. Electronic Wave Functions in Semiconductor Clusters : Experiment and Theory. Journal of Physical Chemistry, 1986, vol. 90, p.2555–2560.
42. FENG D.H., XU Z.Z., JIA T.Q., et al. Quantum size effects on exciton states in indirect-gap quantum dots. Physical Review B, 2003, vol. 68, no. 035334.
43. REBOREDO F.A., PIZZAGALLI L., GALLI G. Computational Engineering of the Stability and Optical Gaps of SiC Quantum Dots. Nano Letters, 2004, vol. 4, no. 5, p.801–804.
44. PENG X.-H., NAYAK S.K., ALIZADEH A., et al. First-principles study of the effects of polytype and size on energy gaps in SiC nanoclusters. Journal of Applied Physics, 2007, vol. 102, no. 024304.
45. FAN J.Y., WU X.L., KONG F., et al. Luminescent silicon carbide nanocrystallites in 3C-SiC/polystyrene films. Applied Physics Letters, 2005, vol. 86, no. 171903.
46. FAN J.Y., WU X.L., LI H.X., et al. Luminescence from colloidal 3C-SiC nanocrystals in different solvents. Applied Physics Letters, 2006, vol. 88, no. 041909.
47. BOTSOA J., BLUET J.-M., LYSENKO V., et al. Luminescence mechanisms in 6H-SiC nanocrystals. Physical Review B, 2009, vol. 80, no. 155317.
48. KITYK I.V., MAKOWSKA-JANUSIK M., KASSIBA A., et al. SiC nanocrystals embedded in oligoetheracrylate photopolymer matrices; new promising nonlinear optical materials. Optical Materials, 2000, vol. 13, p.449–453.
49. KITYK I.V. Non-linear optical phenomena in the large-sized nanocrystallites. Journal of Non-Crystalline Solids, 2001, vol. 292, p.184–201.
50. BOUCLÉ J., KASSIBA A., EMERY J., et al. Local electrooptic effect of the SiC large-sized nanocrystallites incorporated in polymer matrices. Physics Letters A, 2002, vol. 302, no. 4, p.196–202.

51. BOUCLÉ J., KASSIBA A., MAKOWSKA-JANUSIK M., et al. Electro-optic phenomena in guest-host films of PMMA and SiC nanocrystals. Optics Communications, 2005, vol. 246, no. 4-6, p.415–420.
52. BOUCLÉ J., KASSIBA A., MAKOWSKA-JANUSIK M., et al. Linear electro-optical behavior of hybrid nanocomposites based on silicon carbide nanocrystals and polymer matrices. Physical Review B, 2006, vol. 74, no. 205417.
53. KONOROV S.O., AKIMOV D.A., IVANOV A.A., et al. Anomalous behavior of the second and third harmonics generated by femtosecond Cr:forsterite laser pulses in SiC-polymer nanocomposite materials as functions of the SiC nanopowder content. Journal of Raman Spectroscopy, 2003, vol. 34, p.999–1006.
54. KONOROV S.O., SIDOROV-BIRYUKOV D.A., BUGAR I., et al. Diffuse optical harmonic generation in SiC nanopowder films: hunting scattered photons. Applied Physics B, 2004, vol. 78, p.73–77.
55. BORSHCH A.A., BRODYN M.S., VOLKOV V.I., et al. Nonlinear refraction in nanocrystalline silicon carbide films. JETP Letters, 2008, vol. 88, no. 6, p.386–388.
56. NAYFEH M.H., AKCAKIR O., BELOMOIN G., et al. Second harmonic generation in microcrystallite films of ultrasmall Si nanoparticles. Applied Physics Letters, 2000, vol. 77, no. 25, p.4086–4088.
57. JIANG Y., WILSON P.T., DOWNER M.C., et al. Second-harmonic generation from silicon nanocrystals embedded in SiO_2. Applied Physics Letters, 2001, vol. 78, no. 6, p.766–768.
58. HE G.S., ZHENG Q., YONG K.-T., et al. Two- and Three-Photon Absorption and Frequency Upconverted Emission of Silicon Quantum Dots. Nano Letters, 2008, vol. 8, no. 9, p.2688–2692.
59. ROUSSIGNOL P., RICARD D., FLYTZANIS C. Quantum Confinement Mediated Enhancement of Optical Kerr Effect in CdS(x)Se(1-x) Semiconductor Microcrystallites. Applied Physics B, 1990, vol. 51, p.437–442.
60. SCHMITT-RINK S., MILLER D.A.B., CHEMLA D.S. Theory of the linear and nonlinear optical properties of semiconductor microcrystallites. Physical Review B, 1987, vol. 35, no. 15, p.8113–8125.
61. IRIMPAN L., NAMPOORI V.P.N., RADHAKRISHNAN P., et al. Size-dependent enhancement of nonlinear optical properties in nanocolloids of ZnO. Journal of Applied Physics, 2008, vol. 103, no. 033105.

62. LI Y., TAKATA M., NAKAMURA A. Size-dependent enhancement of nonlinear optical susceptibilities due to confined excitons in CuBr nanocrystals. Physical Review B, 1998, vol. 57, no. 15, p.9193–9200.
63. PADILHA L., FU J., HAGAN D., et al. Frequency degenerate and nondegenerate two-photon absorption spectra of semiconductor quantum dots. Physical Review B, 2007, vol. 75, no. 075325.
64. PADILHA L.A., NOOTZ G., OLSZAK P.D., et al. Optimization of band structure and quantum-size-effect tuning for two-photon absorption enhancement in quantum dots. Nano Letters, 2011, vol. 11, p.1227–1231.
65. WINTER S., ZIELINSKI M., CHAUVAT D., et al. The Second Order Nonlinear Susceptibility of Quantum Confined Semiconductors—A Single Dot Study. The Journal of Physical Chemistry C, 2011, vol. 115, p.4558–4563.
66. ATTOLINI G., ROSSI F., FABBRI F., et al. Cubic SiC Nanowires: Growth, Characterization and Applications, Nanowires. Paola Prete (Ed.), Croatia: InTech, 2010, p. 414, ISBN 978-953-7619-79-4.
67. ZEKENTES K., ROGDAKIS K. SiC nanowires: material and devices. Journal of Physics D: Applied Physics, 2011, vol. 44, no. 133001.
68. ROGDAKIS K., LEE S.-Y., BESCOND M., et al. 3C-Silicon Carbide Nanowire FET: An Experimental and Theoretical Approach. IEEE Transactions on Electron Devices, 2008, vol. 55, no. 8, p.1970–1976.
69. SONG H.-J., ZHANG Z.-Z. Investigation of the tribological properties of polyfluo wax/polyurethane composite coating filled with nano-SiC or nano-ZrO2. Materials Science and Engineering: A, 2006, vol. 426, p.59–65.
70. SHIN J.-H., KUMAR B.V.M., KIM J.-H., et al. Tribological Properties of Si_3N_4/SiC Nano-Nano Composite Ceramics. Journal of the American Ceramic Society, 2011, vol. 94, no. 11, p.3683–3685.
71. KIM D.-W., CHOI Y.-J., CHOI K.J., et al. Stable field emission performance of SiC-nanowire-based cathodes. Nanotechnology, 2008, vol. 19, no. 225706.
72. ZHOU W., YAN L., WANG Y., et al. SiC nanowires: A photocatalytic nanomaterial. Applied Physics Letters, 2006, vol. 89, no. 013105.
73. FAN J., LI H., JIANG J., et al. 3C-SiC nanocrystals as fluorescent biological labels. Small, 2008, vol. 4, no. 8, p.1058–1062.

74. ROSENBLOOM A.J., SIPE D.M., SHISHKIN Y., et al. Nanoporous SiC : A Candidate Semi-Permeable Material for Biomedical Applications. Biomedical Microdevices, 2004, vol. 6, no. 4, p.261–267.
75. MOGNETTI B., BARBERIS A., MARINO S., et al. Preferential Killing of Cancer Cells Using Silicon Carbide Quantum Dots. Journal of Nanoscience and Nanotechnology, 2010, vol. 10, no. 12, p.7971–7975.

Chapter 2

Materials and Methods

As it was shown in first chapter, different methods can be implemented to fabricate SiC nanostructures. Simple and efficient electrochemical etching and laser ablation techniques were chosen to be used during this work. In this chapter fabrication steps of the methods will be described in details. Further, to enhance initial optical properties of nano-SiC, planar and colloidal nanohybrids plasmonic nanostructures were produced by depicted procedures. Finally, operation principles of the characterisation techniques, including structural and optical analyses will be discussed.

2.1. Fabrication of SiC nanostructures

2.1.1. Electrochemical etching

Principle of the electrochemical anodization of SiC was discussed in details in Chapter 1. Here, we used two types of electrochemical etching cell presented in **Figure 2.1**. The only difference is in surface area of the porous layer obtained during etching, and thus quantity of nanoparticles. In the first case surface area was ~5cm^2 (**Figure 2.1a**), while the second cell ensures the surface area of ~63 cm^2 (**Figure 2.1b**). Both cells are made of Teflon, the material chemically inert to the strong hydrofluoric (HF) acid used in our experiments. The etching process of a low resistivity grade (<1 Ω*cm) bulk 3C-SiC polycrystalline wafer took place for 2–3 h at a constant current density of 25 mA/cm^2 using a 1:1 HF(50%)/ethanol electrolyte. A copper electrode was used as a backside contact. The counter-electrode was made of platinum immersed into the electrolyte. After the etching, a highly porous network constituted by numerous interconnected 3C-SiC NCs was formed. The ultraporous layer was washed with de-ionized water, naturally dried in ambient air, and then scratched from the wafer. Mechanical dry grinding of the formed free nanoporous layer transformed it into a nanopowder state.

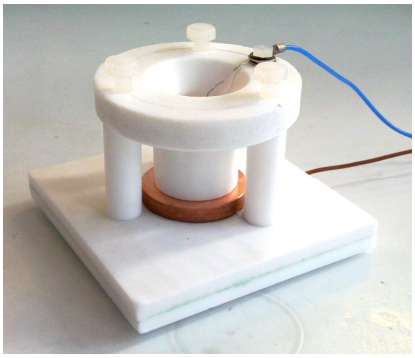

(a)

(b)

***Figure 2.1**: Etching cells for (a) small and (b) large quantity nano-SiC fabrication.*

2.1.2. Laser ablation

Main principle of laser ablation technique for fabrication of nanostructured materials was discussed in chapter 1. In our case, we used modified approach where NPs are directly synthesised in the solution. Schematic view of the procedure can be seen in **Figure 2.2**. The laser ablation was carried out with a Ti/sapphire laser (Hurricane, Spectra Physics Lasers), which provides 110 fs full width at half maximum (FWHM) pulses at wavelength of 800 nm, with

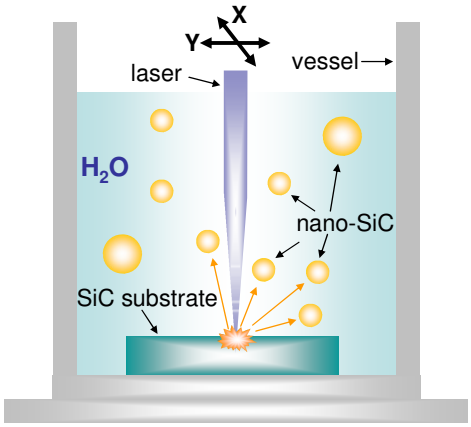

***Figure 2.2**: Scheme of nano-SiC synthesis by laser ablation in water*

maximum energy of 1 mJ/pulse and repetition rate of 1 kHz. The radiation was focused by a 7.5 cm focal length objective on a spot size of about 1 mm in diameter on the 3C polycrystalline silicon carbide substrate placed on the bottom of a 20 mL glass vessel filled with pure deionized water. The height of the water column above the substrate was about 10 mm. The laser spot was scanned on a rectangular shape across the target at a constant moving speed of 0.1 mm/s. The ablation was performed during 2 hours for samples treated with average laser power of 115, 230, 460 mW and for 3 hours for samples ablated by 500 mW laser beam.

2.2. Fabrication of plasmonic nanostructures

2.2.1. Planar nanostructures

A fabrication flowchart describing the realization of the planar plasmonic nanostructures is shown in **Figure 2.3**. First, a SiN_X dielectric layer is deposited on a glass substrate in low frequency plasma enhanced chemical vapor deposition (PECVD) set-up operating at 440 kHz [1, 2]. A gas mixture composed of pure silane (SiH_4) and ammonia (NH_3) is introduced into the reactor at a flowrate of 800 sccm. The pressure and the injected power density are fixed to 1.5 Torr and 0.26 $W*cm^{-2}$, respectively. The depositions are performed at a low temperature of 370°C. The ammonia/silane gas flow ratio determining the stoichiometry of the deposited layers can be varied from 1 to 10. Then, a monolayer of Ag NPs is fabricated on the surface of the SiN_X dielectric film as it was already reported earlier [3]. Briefly, the deposition of the Ag NPs is performed by the immersion of SiN_X layers in an aqueous solution containing 0.14 M of HF acid and 0.5 mM of $AgNO_3$. The samples are then rinsed in de-ionized water and dried into nitrogen flow.

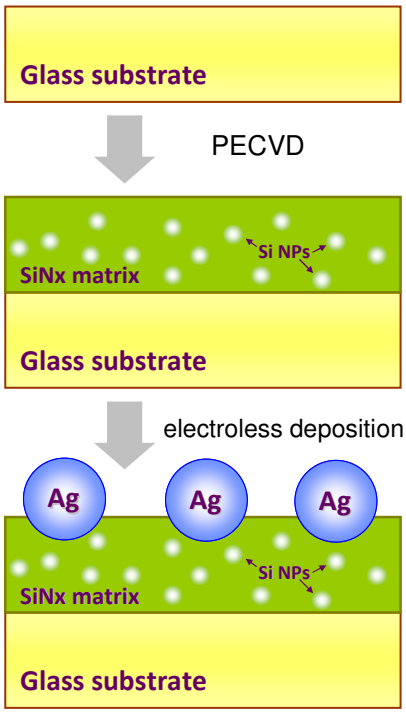

***Figure 2.3**: Fabrication steps of plasmonic nano-Ag/SiN_x/glass substrates.*

2.2.2. Colloidal nanohybrids

Manufacturing steps involved in production of (Au@SiO_2)-SiC nanohybrids (NHs) are sketched in **Figure 2.4**. The colloidal plasmonic NHs are constituted by a gold core covered with a silica shell with controllable thickness. SiC NPs were immobilized at the surface of silica by three different pathways (physical adsorption, electrostatic and covalent bonding) as illustrated. Following sections will discuss in details fabrication of the NHs.

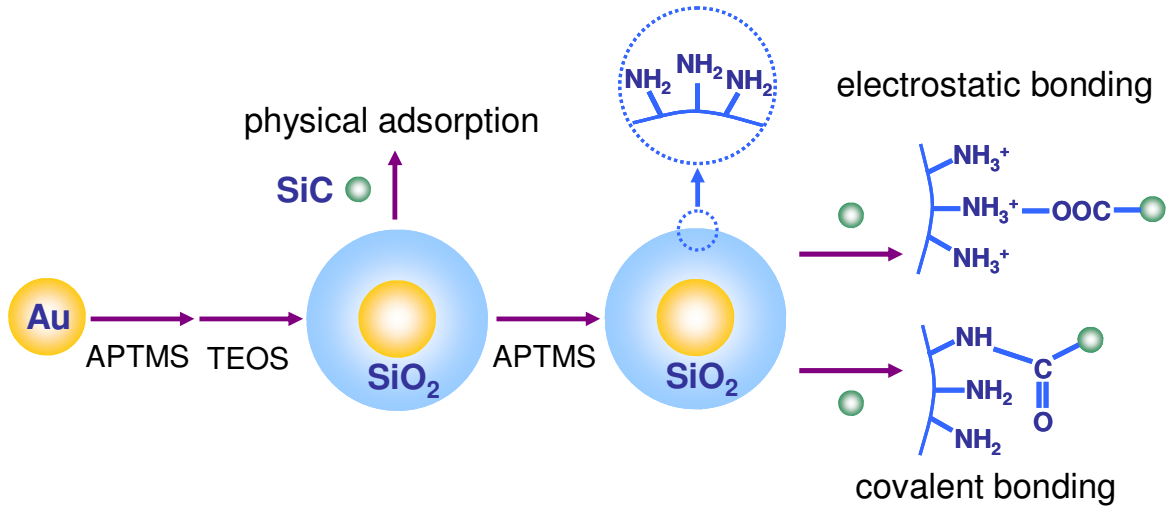

***Figure 2.4**: Synthesis steps and different pathways of SiC NPs immobilization on Au@SiO_2 particles to elaborate NHs.*

2.2.2.1. Chemicals

Gold colloids of 20 nm and 150 nm in diameter were purchased from British BioCell International. Gold colloids of 60 nm in diameter were synthesized according to an already reported procedure [4]. To achieve this synthesis, gold tetrachlorohydrate ($HAuCl_4$) and trisodium citrate were provided by Sigma-Aldrich. Tetra ethyl orthosilicate (TEOS), 3-aminopropyltrimethoxysilane (APTMS), sodium silicate solution ($Na_2(SiO_2)_{3-5}$, 27 wt% SiO_2), ethanol, tetrahydrofuran (THF) and ammonia solution (25-28%) were purchased from Sigma-Aldrich. N, N'-diisopropylcarbodiimide (DCi) and N-hydroxysuccinimide (NHS) were obtained from Fluka. Milli-Q water (18.2 MΩ) was used in all the preparations.

2.2.2.2. Synthesis of Au@SiO_2 particles

The synthesis of Au@SiO_2 nanoparticles was achieved by following reported procedures [5, 6] with some modifications.

Synthesis of Au-20nm@SiO$_2$ nanoparticles. A freshly prepared aqueous solution of APTMS (14.5 µL, 1 mM) was added into 5 mL of commercial 20 nm-gold colloids dispersion ($7x10^{11}$ particles/mL) under vigorous magnetic stirring. After 15 min, a 0.54 wt% sodium silicate solution (200 µL) was added to this dispersion which was stirred for an additional 24 h. At this step, gold nanoparticles with a thin silica shell (~ 2 nm) could be collected by centrifugation (960 g during 1 h). Then these nanoparticles were transferred into 6 mL of a 1:5 water:ethanol mixture, 125 µL of ammonia solution and TEOS were added. The volume of TEOS was set to 0.75 µL and 2.5 µL to obtain 10 nm and 25 nm silica thicknesses, respectively. This dispersion was allowed for reacting overnight under mild magnetic stirring. The product was separated by centrifugation at 10600 g for 10 min, and finally dispersed in 5 mL of ethanol.

Synthesis of Au-60nm@SiO$_2$ nanoparticles. 60 nm gold colloids were first prepared by reduction of $HAuCl_4$ salt by trisodium citrate [4]. 50 mL of a 0.01wt% $HAuCl_4$ solution was heated to reflux. Then, 300 µL of a 1 wt% trisodium citrate solution was added. Solution turned to blue then to red-purple in 2 min. The reaction was continued during 30 min. The silica coating on Au-60 nm was achieved through a modified Stöber process [6]. 5 mL of ethanol, 125 µL of ammonia solution and TEOS were added to 1 mL of gold colloids dispersion in water ($2.3x10^{10}$ nanoparticles/mL). The volume of TEOS was set to 2.5 µL to obtain a 30 nm silica thickness. This dispersion was allowed for reacting overnight under mild magnetic stirring. The product was separated by centrifugation at 10600g for 10 min, and finally dispersed in 5 mL of ethanol.

Synthesis of Au-150nm@SiO$_2$ nanoparticles. The preparation of Au-150nm@SiO_2 nanoparticles is same as the synthesis of Au-60nm@SiO_2. Here, 1 µL of TEOS was added to the mixture of 5 mL of ethanol and 1 mL of gold colloids dispersion ($1.7x10^9$ nanoparticles/mL) to obtain 15 nm silica thickness.

2.2.2.3. Surface functionalization of Au@SiO$_2$ particles

Au@SiO_2 nanoparticles were functionalized with APTMS using a reported method [7]. Various amounts of a 1 mM APTMS solution in ethanol were added to Au@SiO_2 nanoparticles dispersion depending on their diameter. After stirring overnight, the solution was refluxed at 80°C for 2 additional hours. The APTMS-functionalized Au@SiO_2 particles were purified by washing several times with ethanol. The surface density of amino groups was determined by Brillant Coomassie Blue titration.

2.2.2.4. Preparation of (Au@SiO_2)SiC NHs

SiC NPs were prepared by above-mentioned electrochemical etching method. The obtained SiC nanopowder was dispersed in water and then centrifuged at 4900 g for 3 min in order to sediment large crystallites at the bottom of the centrifugation tube and to collect the useful top part of the suspension. These nanoparticles are highly stable in water. At last, the concentration of SiC dispersion was set to 1 g L^{-1}. Three different methods were used to immobilize SiC NPs onto Au@SiO_2 particles (**Figure 2.4**):

***Physical adsorption**:* 200 µL of SiC NPs solution in water (1 g L^{-1}) was mixed with 200 µL of a Au@SiO_2 particles solution (containing 1.4×10^{11} particles) in water. The mixture was sonicated during 10 min, and centrifugated at 6800 rpm during 3 min. Then, the supernatant, which contained the SiC NPs that were not adsorbed on Au@SiO_2 particles, was eliminated and the precipitate was dispersed in water for characterization.

***Electrostatic bonding**:* 200 µL of SiC NPs solution in water (1 g L^{-1}) was mixed with 200 µL of a Au@SiO_2-NH_2 particles, solution (containing 1.4×10^{11} particles) in water. The mixture was sonicated during 10 min, and centrifuged at 6800 rpm during 3 min. Then, the supernatant, which contained the SiC NPs that were not electrostatically bonded onto amino groups, was eliminated and the precipitate was dispersed in water for characterization.

***Covalent bonding**:* the NHs were prepared modifying the reported method [8]. NHS and DCi (molar ratio of NHS/DCi = 1:2.5) were added to 3 µL of SiC NPs solution (1 g L^{-1}) and 200 µL of Au@SiO_2-NH_2 particles (containing 1.4×10^{11} particles) in dry tetrahydrofuran. The mixture was refluxed at 60°C in dry tetrahydrofuran for 4 hours. NHs were purified by centrifugation and washed three times with ethanol. Finally, the precipitate was dispersed in a 1:1 water/ethanol mixture for characterization.

2.3. Characterization methods

During sample preparation discussed in previous sections, it was essential to identify interconnection between the framework of the nanostructures and its influence on the optical properties, in order to optimize the preparation in a controllable way. Different observation techniques were used to measure structural parameters, including transmission electronic microscopy (TEM), scanning electron microscopy (SEM) and atomic force microscopy (AFM). This section also describes complementary absorption and luminescence spectroscopy measurements used during the thesis. While luminescence deals with electronic transitions from excited to the ground states, absorption reveals details about transitions from the ground to the excited states. Together with nonlinear optical characterization techniques these measurements allowed deep investigation of nano-SiC properties.

2.3.1. Structural analysis

2.3.1.1. Atomic-force microscopy

Surface topology of the planar nanostructures was measured by atomic force microscopy (AFM), whose schematic diagram is presented in **Figure 2.5**. In this technique, the tip attached to a cantilever sweeps the surface of the material to be studied, following the relief. The cantilever may be deflected under the action of different types of forces, such as Van der Waals, electrostatic, magnetic, etc. The relative position of the tip to the surface is measured by a position-sensitive photodetector detecting a laser beam reflected by the cantilever carrying the tip. Through a piezoelectric ceramic, tip-cantilever system can be moved along the X and Y directions (in the plane of the sample) and Z (perpendicularly to the sample). Mapping the position of the tip gives precisely the probed surface topography. On some systems, the movement in the XY plane is through the sample and not by the tip-cantilever system. Lateral resolution of AFM is determined by the tip curvature radius, while the vertical resolution is of the order of angstrom: one can easily visualize atomic steps on a clean surface. Viewable surface depends on the piezoelectric ceramic, and can range from hundred nanometres to about 150 microns. The

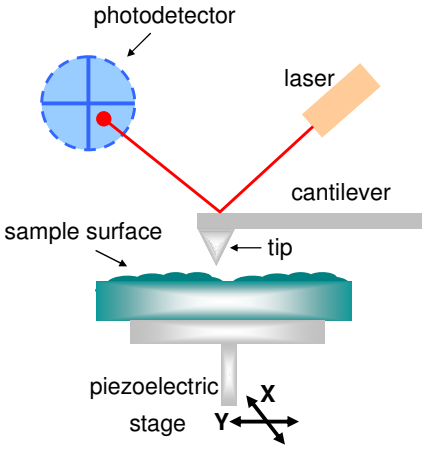

***Figure 2.5** : Function principle of AFM.*

AFM is suitable to any surface, including the insulating surfaces. The AFM also offers the possibility to browse the surface without touching it (non-contact method), or by intermittent contact (tapping mode), to limit the possible damage of a fragile samples.

AFM images were acquired by commercially available Digital 3100 (DI 3100) apparatus.

2.3.1.2. Electron microscopy

In electron microscopy (EM), operating principles are the same as in optical microscopy, but are based on electrons instead of light. Electron microscopes have a greater resolving power than a light-powered optical microscope, because electrons have wavelengths about 100,000 times shorter than visible light (photons), and can theoretically achieve better than 50 pm resolution, whereas ordinary, non-confocal light microscopes are limited by diffraction to about 200 nm resolution.

Images in EM are obtained by the focused electron beam, which illuminate the surface of the sample. Pictures can be seen in many ways - in rays which passed through the object, the reflected rays, by registering secondary electrons or X-rays. Focusing the beam of electrons is ensured by means of electrostatic or electromagnetic lenses as the lenses of the optical microscope.

The schematic principle of TEM is shown in **Figure 2.6a**. The system consists of a vacuum chamber where the electrons are emitted by an electron gun. The electrons are accelerated in the barrel by a high voltage, which defines associated wavelength of the electrons. A second magnetic lens system is used to enlarge the image obtained. The final image, magnified about 10,000 times, is formed in the observation chamber on a fluorescent screen that can be observed visually.

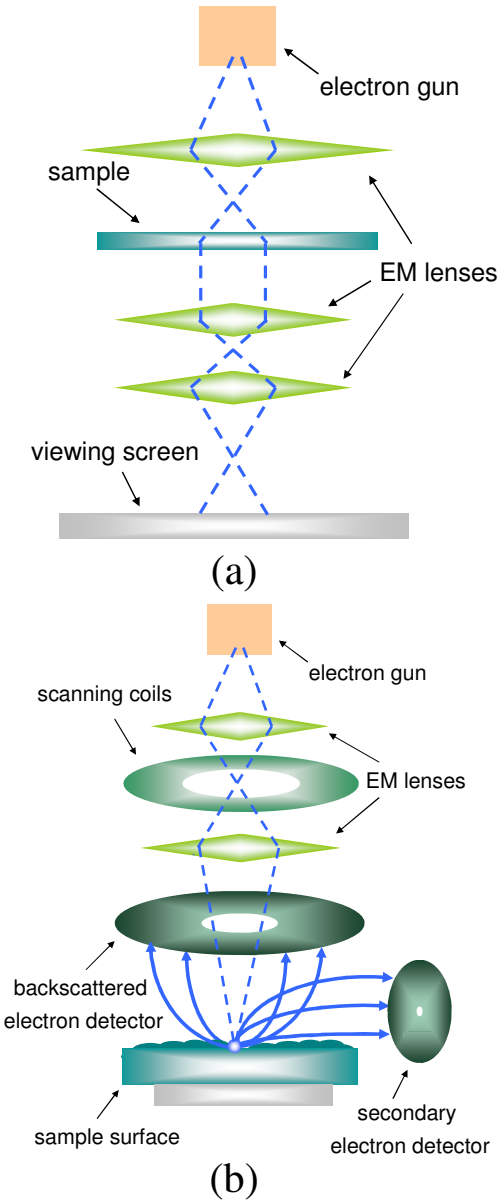

***Figure 2.6**: Function principle of (a) TEM, and (b) SEM.*

When the electron beam passes through the sample, a very large proportion of electrons is transmitted directly, this provides an interpretable image of the specimen.

Unlike the TEM, where electrons of the high voltage beam carry the image of the sample, the electron beam of the scanning electron microscope (SEM) carry only part of it. The SEM produces images by probing the specimen with a focused electron beam that is scanned across a rectangular area of the specimen. The general principle of SEM operation is illustrated in **Figure 2.6b**. As in the TEM, the system consists of a vacuum chamber where the electrons are emitted by an electron gun. Deflection coils of X and Y move the electronic beam over the surface of the sample (XY plane). The primary electrons from the electron gun strike the surface of the sample. Some electrons are scattered elastically (high-energy backscattered electrons), while others, during the impact give part of their kinetic energy to the atoms, causing ionization and ejection of low-energy secondary electrons. The ionized atoms can decay by light emission (cathodoluminescence) or X-ray emission. The backscattered and secondary electrons emitted by the sample are collected by selective detectors. The image displayed by a SEM represents the surface morphology of the sample by corresponding variable intensity of signals from the detectors with the position of the beam on the specimen when the signal was generated. Despite the fact that the image resolution of an SEM is about an order of magnitude poorer than that of a TEM, SEM is able to image bulk samples and relying on surface processes rather than transmission, can produce images that are good representations of the three-dimensional shape of the sample.

TEM pictures were obtained by EM-002B (Topcon, Japan) high-resolution transmission electron microscope operating at 200 kV. SEM observations were performed by means of SEM (Tescan, Czech Republic) or Inspect S50 (FEI, USA).

2.3.1.3. Dynamic/electrophoretic light scattering

The colloidal dispersion of the nanostructures was investigated by means of dynamic light scattering (DLS) technique in order to measure size distribution. Additionally, dispersed in the solution nanostructures acquire a surface charge, either by ionization of surface groups, or adsorption of charged species. In present studies, electrophoretic light scattering (ELS) was utilized in zeta-potential measurements to gain information of this surface charge.

The zeta potential is the electrostatic potential at the particle slipping plane, which is the outer boundary of electrical double layer within which all ions diffuse with the particle (**Figure 2.7**) [9]. Electrical double layer is composed of an inner region, called the Stern layer,

where the ions are strongly bound and an outer, diffuse, region where they are less firmly attached. The zeta potential is a function of the surface charge density, and thus, any change in the surface charge, either valence or ion condensation, will lead to changes in the measured zeta potential. The zeta potential is calculated from the mobility measured during an ELS experiment. In ELS, the velocity of a charged particle is measured by monitoring the frequency shift (Δν) of the light scattered from the particle under the influence of an applied electric field. Light scattered from stationary particles will have the same frequency and wavelength as the incident light, whereas light scattered from particles in motion will be Doppler shifted. In ELS, the velocity or mobility (U_e) of the particle is calculated from the Doppler frequency shift using the expression shown below, where θ is the scattering angle and λ is the wavelength of the incident light.

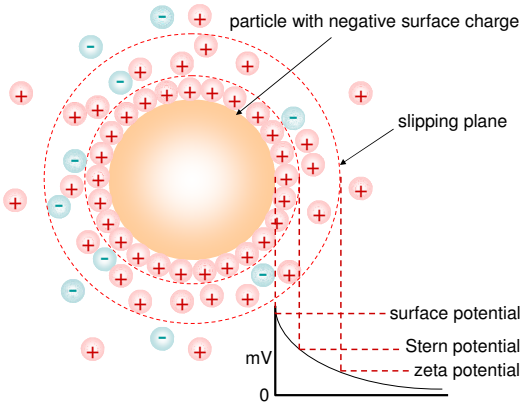

***Figure 2.7**: Ion concentration and potential difference as a function of distance from the charged surface of a particle dispersed in a medium.*

$$\Delta\nu = 2U_e \frac{\sin(\theta/2)}{\lambda} \qquad (2.1)$$

The magnitude of the velocity is dependent upon the strength of electric field or voltage gradient, the dielectric constant of the medium (ε), the viscosity of the medium (η) and the particle surface charge density (or zeta-potential(ζ)):

$$U_e = \frac{2\varepsilon\zeta f(ka)}{3\eta} \qquad (2.2)$$

, where f(ka) is the Henry function which describes the retardation of the mobility arising from the presence of the ionic atmosphere (equal to 1 or 1.5 in Huckel or Smoluchowski limit, respectively).

We can also finally define zeta-potential taking into account (2.1) and (2.2) as:

$$\zeta = \frac{3\eta\,\lambda\,\Delta\nu}{4\varepsilon\sin(\theta/2)f(ka)} \qquad (2.3)$$

DLS, also known as photon correlation spectroscopy, is a technique used to measure the Brownian motion (diffusion) and subsequent size distribution of an ensemble collection of particles in solution. For a collection of particles in solution, illuminated by a monochromatic

light source such as a laser, the scattering intensity measured by a detector located at some point in space will be dependent upon the relative positions of the particles within the scattering volume. The position dependence of the scattering intensity arises from constructive and destructive interference of the scattered light waves. If the particles are static, then one would expect to observe a scattering intensity that is constant with time. In practice however, the particles are diffusing according to Brownian motion, and the scattering intensity fluctuates about an average value equivalent to the static intensity.

Correlation is a second order statistical technique for measuring the degree of non-randomness in an apparently random data set. When applied to a time dependent intensity trace, as measured with a dynamic light scattering instrument, the correlation coefficients are calculated as shown below, where τ is the delay time.

$$G(\tau) = \int_0^\infty I(t)(t+\tau)dt \tag{2.4a}$$

$$G_k(\tau_k) = \sum_{i=0} I(t_i)I(t_i+\tau_k) \tag{2.4b}$$

In DLS, all of the information regarding the motion or diffusion of the particles in the solution is embodied within the measured correlation curve. For monodisperse samples, consisting of a single particle size group, the correlation curve can be fit to a single exponential form as given in the following expression, where (B) is the baseline, (A) is the amplitude or intercept of the correlation function, and (D) is the diffusion coefficient:

$$G(\tau) = \left\langle I(t) \bullet I(t+\tau) \right\rangle = A\left[1 + B \cdot \exp(-2Dq^2\tau)\right] \tag{2.5}$$

The exponential fitting expression can be expanded to account for polydispersity or peak broadening effects, as shown below:

$$G(\tau) = \left\langle I(t) \bullet I(t+\tau) \right\rangle = A\left[1 + B \cdot \exp(-2Dq^2\tau + \mu\tau^2)\right] \tag{2.6}$$

The scattering vector (q) and diffusion coefficient are defined by the following expressions, where (n) is the solvent refractive index, (λ_o) is the vacuum wavelength of the laser, (θ) is the scattering angle, and R_H is the hydrodynamic radius:

$$q = \frac{4\pi n}{\lambda_0}\sin(\frac{\theta}{2}) \tag{2.7}$$

R_H is then calculated from the diffusion coefficient (D) using the Stokes-Einstein equation, where (k) is the Boltzmann constant, (T) is the temperature, and (η) is the medium viscosity:

$$D = \frac{kT}{6\pi\eta R_H} \quad (2.8)$$

One of the possible drawback for measuring small particle distribution by DLS method is based on the fact that the large particles scatter much more light than small particles (the intensity of scattering of a particle is proportional to the sixth power of its diameter (Rayleigh's approximation)), thus calculated size distribution can be mistakenly dominated by small amount of aggregates or larger particles.

Both DLS and ELS measurements were performed by Zetasizer Nano ZS apparatus (Malvern, UK). Schematic operational principle is described in **Figure 2.8**. A laser with emission wavelength λ=633 nm is used to provide a light source to illuminate the sample particles within a cell. Depending on the size distribution or zeta potential measurement, scattered light is registered by either avalanche photodiode detector in 13 degree (forward-scattering) or in 172 degree (back-scattering) geometry, respectively. The intensity of the scattered light must be within a specific range for the detector to successfully measure it. If too much light is detected then the detector will become overloaded. To overcome this, an "attenuator" is used to reduce the intensity of the laser and hence reduce the intensity of the scattering. The scattering intensity signal from the detector is passed to a correlator. This correlator information is then passed to a computer, where the size or zeta-potential information is derived.

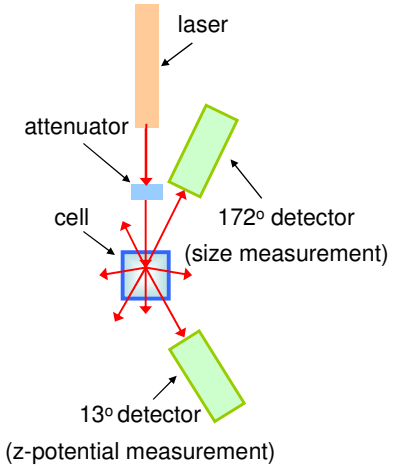

***Figure 2.8**: Schematic principle of DLS/ELS measurements.*

2.3.2. Optical analysis

2.3.2.1. Absorption spectroscopy

Electromagnetic radiation due to its interaction with a sample is absorbed. The intensity of absorbed energy as a function of frequency or wavelength is represented by the absorption spectrum. Absorption spectroscopy is used as a tool to determine the presence and/or quantity

of a particular substance in a sample. In general, infrared spectroscopy (IR/FTIR) allows identification and study of chemical species by absorption of specific energies (wave-numbers, wavelengths). Ultraviolet-visible (UV-Vis) spectroscopy is used for the visualisation of electronic transitions in the sample.

2.3.2.1.1. Uv-Visible spectroscopy

The instruments used in UV-Vis spectroscopy (spectrophotometers) detect the intensity of light passing through a sample "I", and compare to the intensity of the light before passing the sample, "I_0". The ratio "I / I_0" is usually given in percent transmittance (% T). The absorbance (A) is connected to the transmittance according to the equation:

$$A = -\log (\%T/100\%) \quad (2.9)$$

This value is also used in quantitative way to determine concentration of an absorbing species, using the Beer-Lambert law:

$$A = \alpha c L \quad (2.10)$$

,where

α: absorption coefficient

c: concentration

L: the optical path length through the sample.

If, however, the sample contains any other background caused by turbidity or interfering components, determination of the samples absorbance is not always correct. Spectrally it can provoke significant deviations, since Rayleigh scattering efficiency being proportional to the inverse forth power of the light wavelength ($\sim\lambda^{-4}$) conceals small absorption signals at short wavelengths.

A spectrophotometer can be single or double beam and either with single or double-monochromator. Firstly, double beam device has the advantage of simultaneous measurements of T and T_0 to overcome the problems of the excitation lamp drifts during the measurement time. Secondly, in comparison with single-monochromator systems, double monochromator spectophotometer is free of some mistaken absorption signals, which can appear in the samples with detectable photoluminescence.

The schematic diagram of double beam double-monochromator spectrophotometer is given in **Figure 2.9**. The light sources are a tungsten-halogen lamp and deuterium lamps to cover visible and UV spectral range, respectively. The multi-wavelengths light from the

lamps is dispersed by a first monochromator. This beam is chopped by a segmented mirror to perform beam splitting. The two beams pass through a second rotating mirror, synchronized with the first, which consecutively switch beam between the measurement of the reference and the sample.

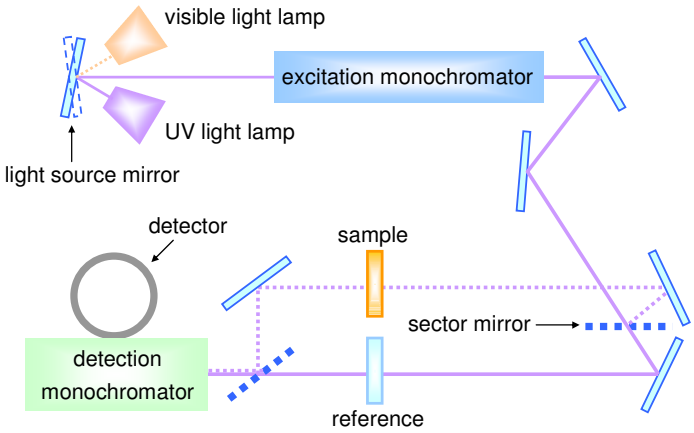

***Figure 2.9**: Schematic diagram of double-beam double-monochromator spectrophotometer.*

The absorption measurements were performed either by double-beam single-monochromator "UV mc2"(SAFAS, Monaco), "Lambda 35" (Perkin Elmer, USA) or double-monochromator "Lambda 1050" (Perkin Elmer, USA) spectrophotometers. For samples with high scattering component, absorption spectra were acquired by means of an integrating sphere RTC-060 (Labsphere, USA) with Spectralon covering coupled to the monochromator-detector system, and Xenon lamp was used as the excitation source.

2.3.2.1.2. Fourier-transform infrared spectroscopy

A common laboratory instrument that uses this technique is Fourier transform infrared (FTIR) spectrometers. They are able to cover wide range of electromagnetic spectrum divided into three regions: the near-infrared (0.8–2.5 μm wavelength), mid-infrared (2.5–25 μm) and far-infrared (25–1000 μm).

The infrared spectrum of a sample is recorded by passing a beam of infrared light through the sample. Examination of the transmitted or reflected light reveals how much energy was absorbed at each frequency (or wavelength). Alternatively to the wavelength scanning using a monochromator, the whole wavelength range is measured at once using a Michelson interferometer with a mobile mirror prior to the sample. The collected signal corresponds then to an interferogram. Digital processing of the interferogram by Fourier transform followed gives then a transmittance spectrum, which may be converted to absorbance using a dedicated procedure. The term *Fourier transform infrared spectroscopy* originates from the need to convert the raw data into the actual spectrum by Fourier

transformation. Analysis of the position, shape and intensity of peaks in this spectrum reveals details about the molecular structure of the sample.

The FITR measurements were performed by Nicolet NEXUS-470 (Thermo Scientific) spectrometer or Vertex 80 (Bruker Optics) apparatus.

2.3.2.2. Photoluminescence spectroscopy

The photoluminescence spectroscopy is used to investigate a backward electronic transition from the excited to ground states of the sample. There are many types of luminescence distinguished by the different radiative channels. The radiative deactivation processes, however, are in competition with non-radiative recombination process limiting total quantum yield of photoluminescence. The quantum yield of photo-excited luminescence is defined as [10]:

QY= (number of photons emitted)/(number of photons absorbed) (2.11)

, nevertheless, in practice we detect only very small and/or unknown fraction of the emitted and absorbed light:

QY= [α*(number of photons emitted)]/[β*(number of photons absorbed)] (2.12)

,where α and β are constants related to the fraction of emitted light entering the light collection optics of the detection system and the intensity of the excitation source at the excitation wavelength, respectively.

As it can be seen it is not trivial task to calculate precisely the number of emitted and absorbed photons by the sample. Thus, two approaches can be adopted to determine the unknowns in the equation (2.12): comparative and absolute. First method relies on the fact that the α and β constants should be quantitatively the same for different sample solutions compared under identical conditions of excitation. In the simplest case, the absorption and luminescence signal of the reference solution with known quantum yield is measured and compared with the sample to be analyzed. With the absolute method one measures directly the values of the numerator and denominator in equation (2.12) by the use of an “integrating sphere”. Firstly, the number of photons absorbed by the sample is determined as the difference between the integrated area (number of photons) at the excitation wavelength reaching the detector for the sample and the reference. Secondly, the integrated area under the corrected luminescence spectrum of the sample represents the number of photons emitted. In this way, constants related to the detection (α and β) in equation (2.12) are equal and cancel out.

Figure 2.10 shows the schematic configuration of the bench used for PL measurements. Depending on the samples and experiments for the room temperature PL spectra, an excitation source either frequency doubled argon-ion laser emitting in the ultraviolet at λ=244 nm (LEXEL, USA), or the tripled frequency (λ=343 nm) of a diode-pumped ytterbium femto-second laser (Amplitude Systems, France), or from an argon-ion laser with λ=458 nm or λ=488 nm (Coherent, USA) was used. Low-pass filters were used to exclude the scattered laser signal. The emission spectra were dispersed using a Horiba Jobin Yvon iHR320 or HRS-2 spectrometer. Detection was performed by means of a liquid nitrogen-cooled charge coupled detector (Horiba Jobin Yvon Symphony CCD) or photomultiplier tube. For absolute quantum yield measurements integrating sphere RTC-060 (Labsphere, USA) with Spectralon covering was connected to the detection system. All of the obtained spectra were corrected by calibration light source to take into account response function of the detection system.

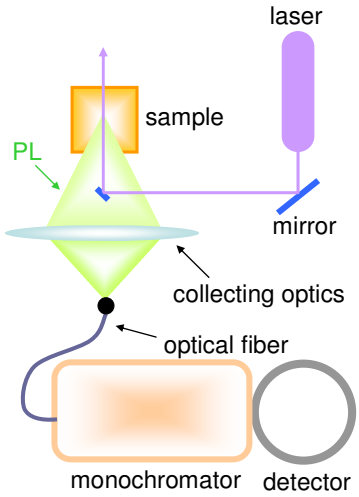

***Figure 2.10**: Basic configuration of PL measurement bench.*

2.3.2.3. *One-photon excitation fluorescence microscopy*

Fluorescence microscopy is an optical imaging technique that commonly uses fluorescence to generate an image of the investigated object. The emitted light, which is usually at a longer wavelength than the illumination, is then imaged through a microscope objective. Two filters are usually used in this technique; an illumination (or excitation) filter, which ensures the illumination at the correct wavelength, and a second emission (or barrier) filter, which ensures none of the excitation light source reaches the detector (**Figure 2.11**). Filter cube is designed to hold a fluorescence filter set (dichroic mirror and excitation and emission filters). The choice of this cube depends on the exact excitation and detection spectrum ranges.

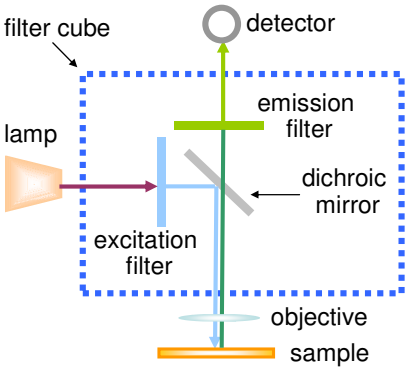

***Figure 2.11**: Schematic of a fluorescence microscope.*

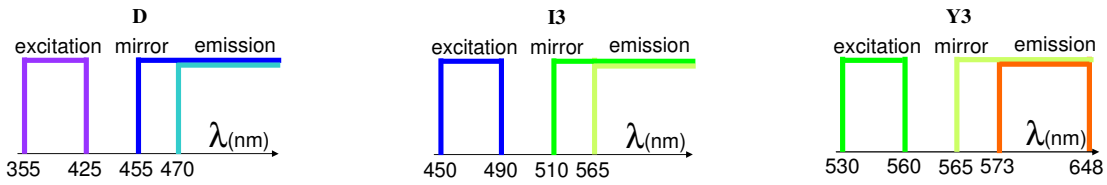

***Figure 2.12**: Transmission and reflection of the components in filter cubes.*

The microscope used in this study is a Leica DMI 4000B. It allows recording fluorescence or contrast white light images. The characteristics of the filter cubes D, I3 Y3 available on this microscope are summarized in **Figure 2.12**.

2.3.2.4. Two-photon excitation microscopy

Two-photon excitation microscopy is the variant of multiphoton fluorescence microscopy and uses pulsed long-wavelength light to excite the specimen being observed. The absorbed energy from two photons, which arrive simultaneously, excites an electron into a higher energy state, from which it can decay. It differs from traditional fluorescence microscopy in which the excitation wavelength is shorter than the emission wavelength, as the summed energies of two long-wavelength exciting photons will produce an emission wavelength shorter than the excitation wavelength. In case of second-harmonic generation microscopy detected light is exactly half the wavelength of the light entering the material.
Multiphoton fluorescence microscopy has similarities to confocal laser scanning microscopy. Both use focused laser beams scanned in a raster pattern to generate images, and both have an optical sectioning effect.

The nonlinear images were acquired using two systems. In a first configuration, a Spectra Physics Mai Tai DeepSee femtosecond oscillator (87 MHz repetition rate) combined to an upfront 2-photon microscope Zeiss 710 NLO. A prism compressor pre-compensating for the pulse group velocity dispersion accumulated through the microscope optics was used to ensure that the pulse duration at the focal plane (~100 fs) was preserved throughout the spectral tunability range of the laser source (700-1000 nm). The latter was focused by a water immersion objective (numerical aperture 1.0) and scanned over an area of 500 x 500 µm with a pixel dwell time of 25.4 µs without further averaging. The detection central wavelength and spectral range could be freely varied with 3 nm resolution.

In the second configuration, the same laser was coupled to Nikon A1R-MultiPhoton inverted microscope. Four independent non-descanned detectors acquire in parallel the epi-collected signal spectrally filtered by four tailored pairs of dichroic mirrors and interference filters, corresponding to 395 (+/-5.5), 485 (+/-10), 531 (+/-20), and 607 (+/-35) nm.

2.4. Conclusions

In this chapter, two different approaches for nano-SiC fabrication have been described. Firstly, SiC nanopowder can be obtained by simple and inexpensive electrochemical etching method. However, this procedure involves extremely toxic and corrosive electrolytes based on hydrofluoric (HF) acids. Moreover, a lot of NPs are lost during the anodization process and numerous rinsing steps of the electrochemically prepared layers contaminated with HF residuals. Thus, direct and clean laser ablation can be used to produce colloidal suspensions of luminescent SiC QDs in water.

For the plasmon enhancement of nano-SiC optical properties, two plasmonic nanostructures fabrication process were described. Planar metallic nanostructures allowed clarification of plasmon-SiC interactions by precisely controllable fabrication steps. Afterwards, colloidal nanohybrids were elaborated to reproduce plasmon-enhancement in much smaller and complex structures.

All of the fabrication steps and physico-chemical properties were correlated by described characterization techniques.

2.5. References

1. PARK N.-M., CHOI C.-J., SEONG T.-Y., et al. Quantum Confinement in Amorphous Silicon Quantum Dots Embedded in Silicon Nitride. Physical Review Letters, 2001, vol. 86, no. 7, p.1355–1357.
2. LELIÈVRE J.-F., DE LA TORRE J., KAMINSKI A., et al. Correlation of optical and photoluminescence properties in amorphous SiNx:H thin films deposited by PECVD or UVCVD. Thin Solid Films, 2006, vol. 511-512, p.103–107.
3. NYCHYPORUK T., ZHOU Z., FAVE A., et al. Electroless deposition of Ag nanoparticles on the surface of SiNx:H dielectric layers. Solar Energy Materials and Solar Cells, 2010, vol. 94, p.2314–2317.
4. FRENS G. Controlled Nucleation for the Regulation of the Particle Size in Monodisperse Gold Suspensions. Nature Physical Science, 1973, vol. 241, p.20–22.
5. LIZ-MARZÁN L.M., GIERSIG M., MULVANEY P. Synthesis of Nanosized Gold−Silica Core−Shell Particles. Langmuir, 1996, vol. 12, no. 18, p.4329–4335.
6. STOBER W., FINK A., BOHN E. Controlled growth of monodisperse silica spheres in the micron size range. Journal of Colloid and Interface Science, 1968, vol. 26, p.62–69.
7. WESTCOTT S.L., OLDENBURG S.J., LEE T.R., et al. Formation and Adsorption of Clusters of Gold Nanoparticles onto Functionalized Silica Nanoparticle Surfaces. Langmuir, 1998, vol. 14, no. 19, p.5396–5401.
8. SUN L., ZANG Y., SUN M., et al. Synthesis of magnetic and fluorescent multifunctional hollow silica nanocomposites for live cell imaging. Journal of Colloid and Interface Science, 2010, vol. 350, p.90–98.
9. Malvern Instruments Technical Support Library, Available online at: <www.malvern.com> (accessed 20.08.2012).
10. Standard for measuring quantum yield, Nanoco Technologies Ltd. Available online at: <www.nanocotechnologies.com/download.aspx?ID=77> (accessed 20.08.2012).

Chapter 3

Initial Physico-Chemical Properties of SiC Nanostructures

Variety of nano-SiC physical properties can be engineered as a function of size, surface structure, and composition. As it was mentioned in first chapter, slight changes in surface termination can drastically alter optical behaviour of nano-SiC. Size tuning, on the other hand, allow controllable appearance of the quantum-confinement effects. Further, interaction with the surrounding media can be important factor of nano-SiC implementation in novel devices with targeted properties.

The starting point of this chapter is a detailed description of physical and chemical properties of SiC nanostructures obtained by electrochemical etching and laser ablation methods. Secondly, special attention will be paid to the size dependent properties, which come into view after filtration and centrifugation procedures. Finally, local field effects on nano-SiC optical properties will be discussed. In particular, the role of dielectric environment and surface charges will be aimed for designing nanostructures with specific optical properties.

3.1. Structural analysis

3.1.1. Nano-SiC obtained by electrochemical etching

3C-SiC nanoporous layer formed by mean of electrochemical anodization can be seen in **Figure 3.1a**. The as-prepared powder (**Figure 3.1b**) can be dispersed in various polar solvents such as ethanol and water. An example of a daylight photo of the optically homogeneous colloidal suspension of the 3C-SiC NPs described in this work is given in **Figure 3.1c**.

(a) (b) (c)

***Figure 3.1**: Pictures of (a) highly porous 3C-SiC layer, (b) SiC nanopowder, and (c) colloidal suspension with dispersed SiC NPs.*

Figure 3.2a shows a TEM image of the spherical-like 3C-SiC NPs with dimensions smaller than 10 nm. These NPs constitute the powder and the colloidal suspensions shown in **Figure 3.1b** and **3.1c**, respectively. The lattice fringes corresponding to the (111) interatomic plane of 3C-SiC can be seen on a high-resolution TEM (HRTEM) image of a single NP given in **Figure 3.2b**. The typical size distribution of the 3C-SiC NPs obtained from the analysis of the TEM images is presented in **Figure 3.2c**.

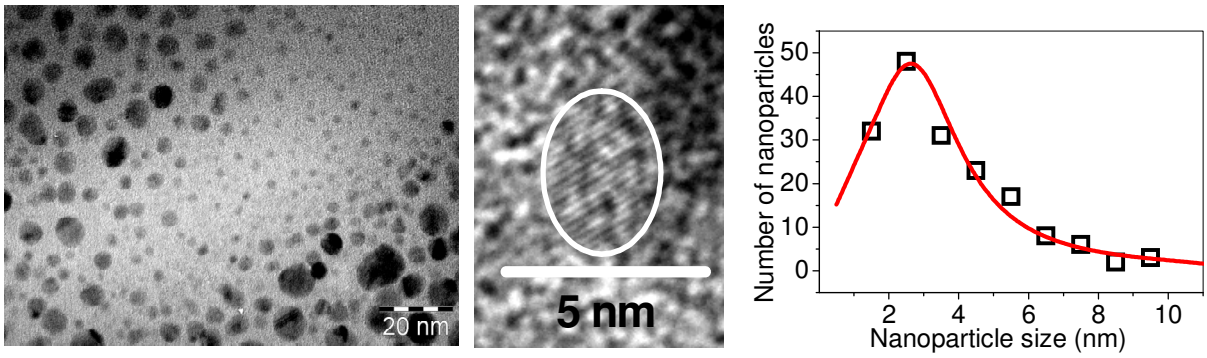

(a) (b) (c)

***Figure 3.2**: (a) TEM image of SiC NPs, (b) high resolution TEM image of a single SiC NP, and (c) typical size distribution diagram of the SiC NPs.*

As one can see, the NP dimensions range from 1 to 9 nm and most of them have dimensions between 1 and 3 nm. Namely, these NPs with dimensions smaller than the Bohr's

diameter of excitons in bulk SiC (~5.4 nm) may exhibit highly efficient luminescence above the bandgap value of bulk 3C-SiC substrates due to quantum confinement effect of the photogenerated charge carriers [1].

3.1.2. Nano-SiC obtained by laser ablation

An example of a daylight photo of the opaque and optically homogeneous colloidal suspension of the SiC NPs obtained by laser ablation is given in **Figure 3.3a**. Contrary to NPs obtained by electrochemical etching method, one can observe pearl colour indicating low light absorption in the visible spectral range.

TEM was used to observe SiC NPs formed by laser ablation in water. Toward this end, a drop of the aqueous solution containing the suspended SiC NPs was deposited on a graphite grid. **Figure 3.3b** shows a TEM image of the spherical-like SiC NPs with dimensions smaller than 10 nm. As one can see, most of the NP dimensions are found to be below 5 nm. As it was in the case of NPs obtained by electrochemical etching, strong quantum confinement effects are highly probable in these NPs.

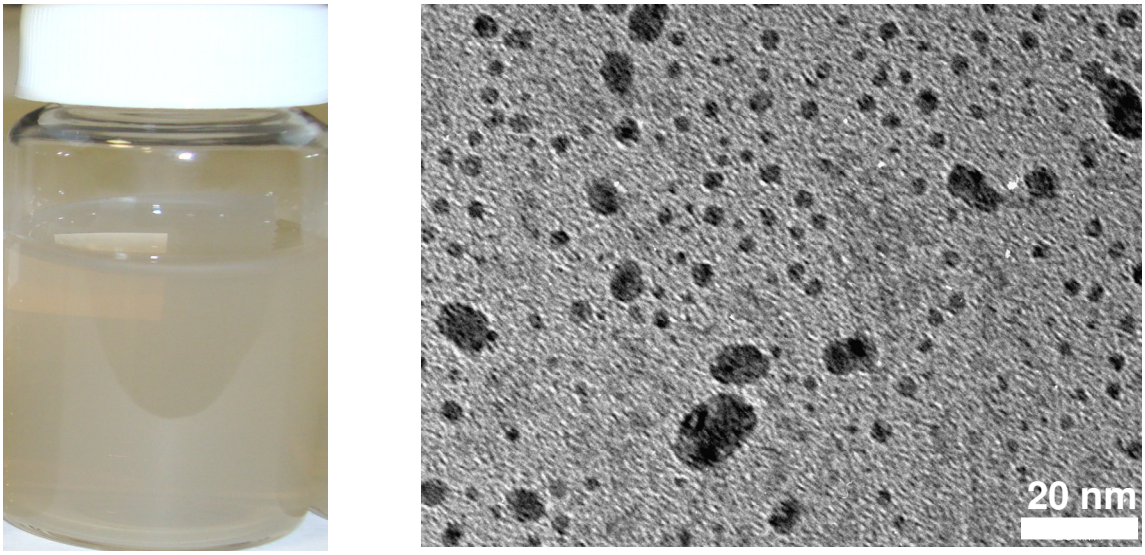

(a) (b)

Figure 3.3*: (a) Picture of colloidal suspension with dispersed SiC NPs, and (b) general TEM image of the formed SiC NPs.*

HRTEM was also performed on some of these NPs. Results obtained on two of them are presented in **Figure 3.4a** and **Figure 3.4c**. In order to enhance the imaging of the planes of these particles, a Fast Fourier Transform (FFT) was done first, then a filter is applied on the FFT to keep only the response of the planes and a reverse FFT (FFT^{-1}) is finally performed. The resulting images are presented in **Figure 3.4b** and **Figure 3.4d**.

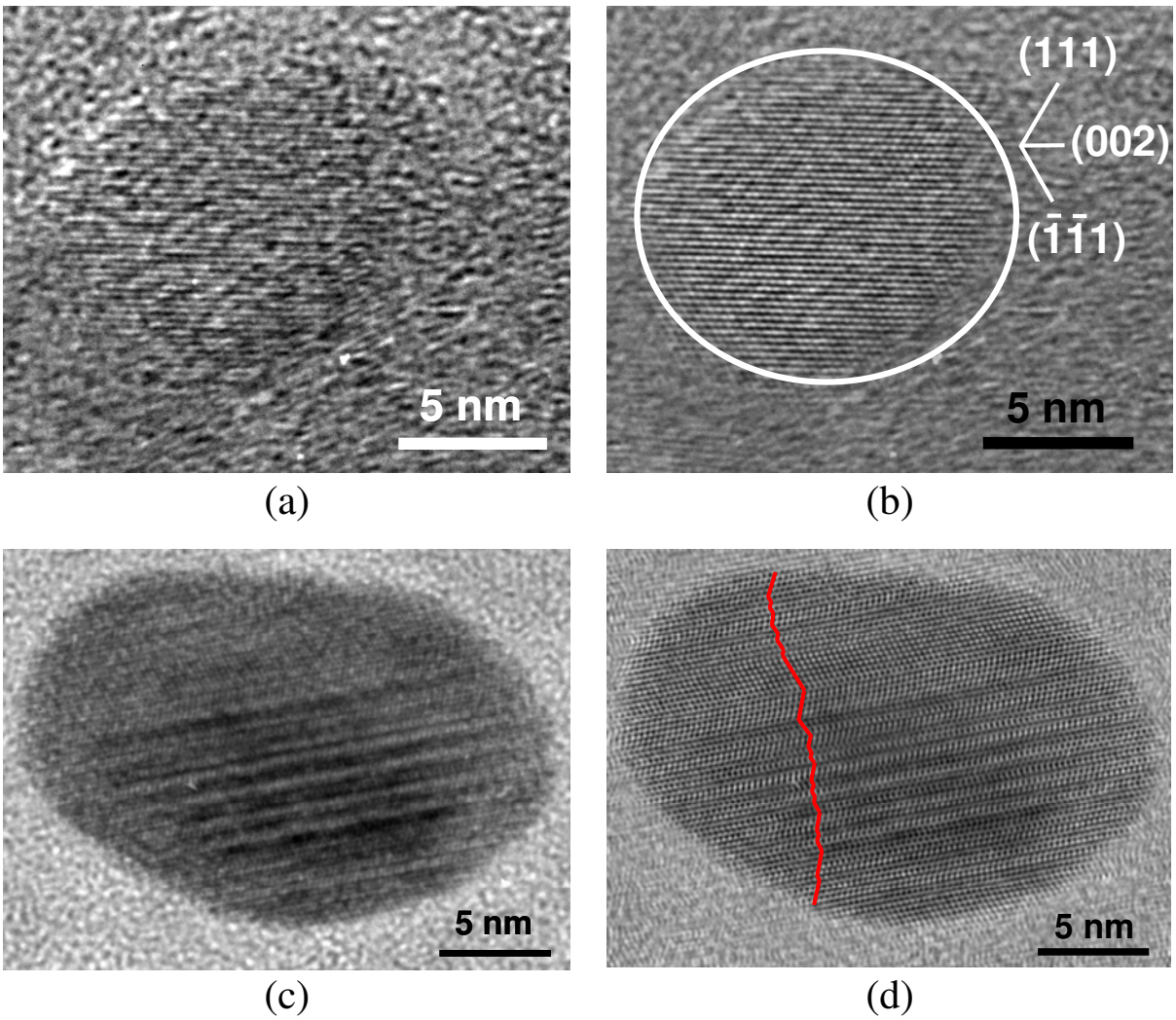

***Figure 3.4**: (a), (c) Two different SiC NPs observed by HRTEM, and (b), (d) the same NPs after an enforcement of the compact planes imaging by FFT filtering.*

While small NPs with diameters <5-7 nm do not present any noticeable changes of crystalline direction (**Figure 3.4b**), numerous non-periodical changes of the crystalline directions illustrated by a red line in **Figure 3.4d** can be observed for larger NPs (>10 nm) suggesting the presence of stacking faults and/or micro-twins. The defect formation can be conditioned by a thermal shock undergone by the NPs during their structural relaxation from laser-induced overheated state to room temperature state when they are ejected by the laser into the surrounding water. Thus, small elastic SiC NPs formed by laser ablation seem to support much better this relaxation contrary to the larger ones plastically relaxing with creation of numerous defects.

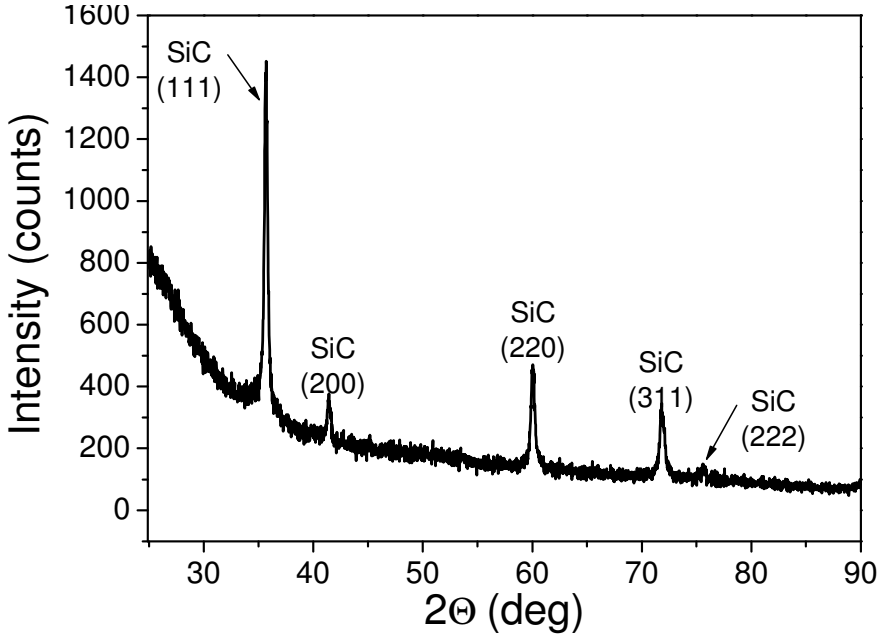

***Figure 3.5**: X-ray diffraction spectrum of the 3C-SiC NPs produced at 460 mW.*

X-ray diffraction spectrum presented in **Figure 3.5** and HRTEM of a single small NP shown in **Figures 3.4b** confirm cubic crystalline nature of the formed SiC NPs. However, for large NPs non-periodic orientation changes complicate determination of exact polytype (**Figure 3.4d**). It worth noting that as it was recently discussed [2], determination of a polytype from XRD spectrum is not straightforward in many cases. Thus, it should be a subject to additional investigation.

3.2. Chemical Composition

3.2.1. Energy-dispersive X-ray spectroscopy

The elemental analysis of the SiC NPs obtained by electrochemical etching was performed by energy-dispersive X-ray (EDX) method. As the energy of the X-rays are characteristic of the atomic structure of the element from which they were emitted, this allows the elemental composition of the specimen to be measured. Typical EDX spectrum of the SiC NPs obtained by electrochemical etching can be seen in **Figure 3.6**. It represents the sequence of unique peaks with increasing energies corresponding to

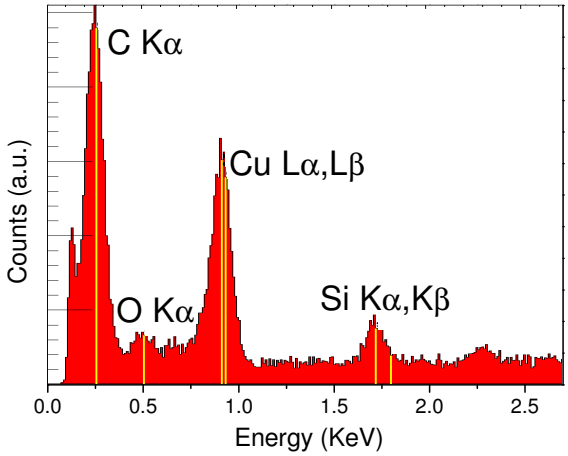

***Figure 3.6**: EDX spectrum of SiC NPs.*

carbon, oxygen, copper and silicon atoms, respectively. Signal from copper atoms is observed in the spectrum due to the copper grid on which drop of SiC NPs suspension was dried. The presence of reasonable proportion of carbon and silicon atoms detected by EDX confirms formation of SiC nanostructures during fabrication procedure.

3.2.2. Temperature-programmed desorption mass spectrometry

Temperature programmed desorption mass spectrometry (TPD-MS) measurements were carried out by heating of the studied samples under vacuum (<10^{-3} Pa) at a heating rate of 0.167 K/s. The heating induced evolved products that were analyzed by MS (EI, -70 eV) on an MX7304A instrument (Selmi, Ukraine). Before the TPD-MS measurements, the samples were pre-evacuated at 10^{-3} Pa for 20 min.

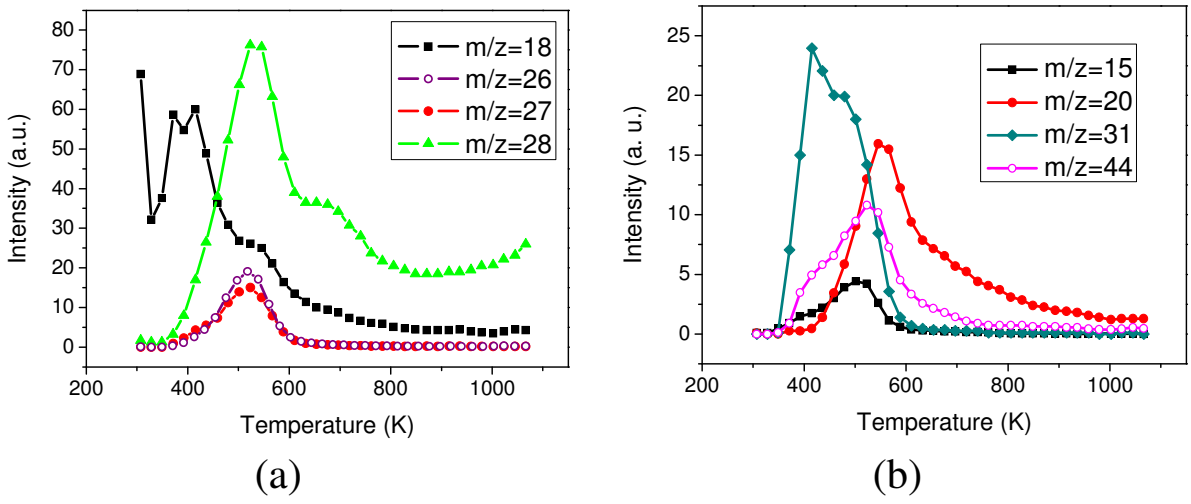

***Figure 3.7**: TPD-MS profiles of porous 3C-SiC for the ions: (a) with m/z= 18 (H_2O^+), 26 ($C_2H_2^+$), 27 ($C_2H_3^+$), and 28 (CO^+ + $C_2H_4^+$); and (b) with m/z= 15 (CH_3^+), 20 (HF^+), 31 (CH_3O^+), and 44 (CO_2^+).*

TPD-MS profiles of 3C-SiC powder are shown in **Figure 3.7**. Intense CO_2 [ions with m/z=44 (CO^{2+}), 28 (CO^+)] and ethylene [ions with m/z= 27 ($C_2H_3^+$), 26 ($C_2H_2^+$)] evolutions, which are assigned to the decomposition of —CO_2H and CH_x surface fragments, respectively, take place approximately at 520 K. These features are similar to those observed for porous 6H-SiC nanostructures [3]. However, some differences can be highlighted between the TPD-MS profiles of porous 6H-SiC and 3C-SiC nanostructures. For example, the intensity of ion with m/z=28 (CO^+) in the spectrum of 3C-SiC is much higher than the intensities of ions with m/z=27 ($C_2H_3^+$) and 44 (CO_2^+). It can indicate that the process resulting in CO formation is

probably due to the thermally induced decomposition of —CO_2H groups bonded directly to Si atoms at the specific surface of the 3C-SiC nanopowder according to the following scheme:

$$\equiv Si - CO_2H \rightarrow \equiv Si - OH + CO$$

In addition, intense peaks of ions with m/z=15 (CH_3^+), 20 (HF^+), shown in **Figure 3.7b**, indicate, respectively, the presence of relatively high fractions of ≡Si—CH_3, and Si—F surface groups in the 3C-SiC nanopowder. Peaks with m/z=31 (CH_3O^+) (**Figure 3.7b**) and 45 ($C_2H_5O^+$) (not shown) can be probably related to the desorption of ethanol due to the reaction between ≡Si—OC_2H_5 and ≡Si—OH surface fragments. In general, the intensities of the peaks on the TPD-MS profiles corresponding to 3C-SiC nanopowder are significantly higher than those on the profiles of porous 6H-SiC nanostructures, observed previously [3]. It means that the concentration of the surface groups due to larger specific surface area of the former is much higher.

3.2.3. Fourier-transform infrared spectroscopy

3.2.3.1. Nano-SiC obtained by electrochemical etching

The infrared spectra were recorded in the 400–4000 cm^{-1} range with resolution of 4 cm^{-1}. Transmission mode in ambient conditions was applied for samples pelletized with KBr. Diffuse reflectance FTIR spectra were recorded in ambient conditions using ground samples deposited as a thin layer on a stainless-steel support. In this case, the spectrum of the support was used as a measurement background.

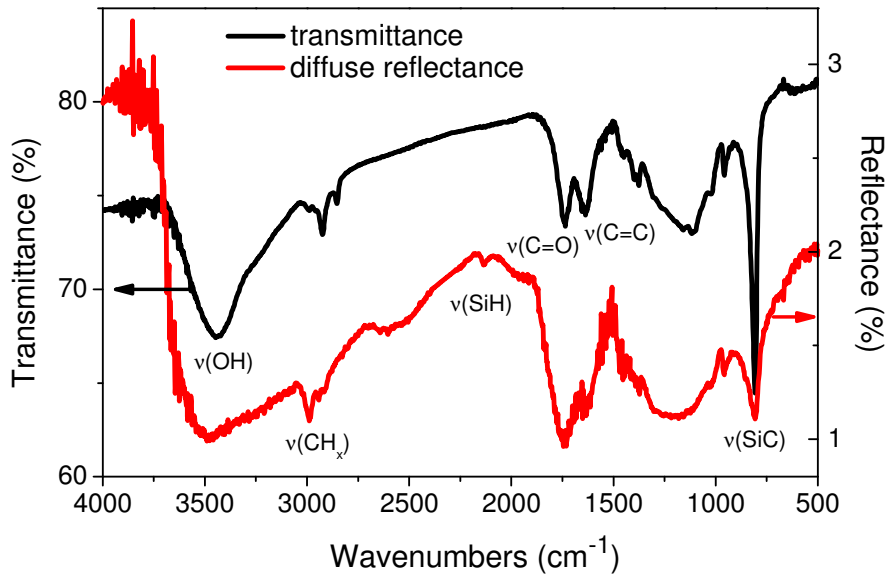

***Figure 3.8**: FTIR spectra (transmittance and diffuse reflectance) of palletized and ground SiC samples.*

The presence of carboxylic acid groups onto the specific surface area of the 3C-SiC NPs is confirmed by FTIR spectra shown in **Figure 3.8**. Indeed, intense ν(C=O) band at 1735 cm^{-1} is clearly seen in the spectra of the 3C-SiC nanopowder recorded both in transmittance and diffuse reflectance modes. Extremely low intensity of ν(Si—H) band reflects the fact that the silane groups are not present on the NP surface in detectable concentration. Rather intense bands at 2989, 2943, and 2914 cm^{-1} reveal the presence of different aliphatic CH_x groups in the nanopowder. Large ν(OH) band centred at about 3500 cm^{-1} corresponds to the adsorbed water molecules as well as to Si—OH groups. Finally, sharp and intense peak at 800 cm^{-1} is attributed to the ν(SiC) band.

All of these chemical groups situated at the surface of 3C-SiC NPs are schematically represented in **Figure 3.9**. The analysis described above allows us to conclude that the surface groups of the 3C-SiC nanopowder are very similar to those of recently studied 6H-SiC porous nanostructures. In addition, we have to mention that in accordance with Shin et al. [4] the 3C-SiC NP surface contains a carbon-enriched layer appearing mainly due to the preferential removing of Si atoms during the electrochemically assisted nanopowder formation.

Dissociation of the carboxylic (Si—COOH) and/or silanol (Si—OH) acid groups in polar solvents leads to the appearance of negative electric charges at the NP surface as it is illustrated by the scheme in **Figure 3.9b**. Presence of these charges was confirmed by measurements of zeta-potentials (-29.8 mV). In particular, they are responsible for the extremely stable and optically homogeneous colloidal suspensions obtained from dispersion of 3C-SiC NPs dispersed in solvents (**Figure 3.1c**).

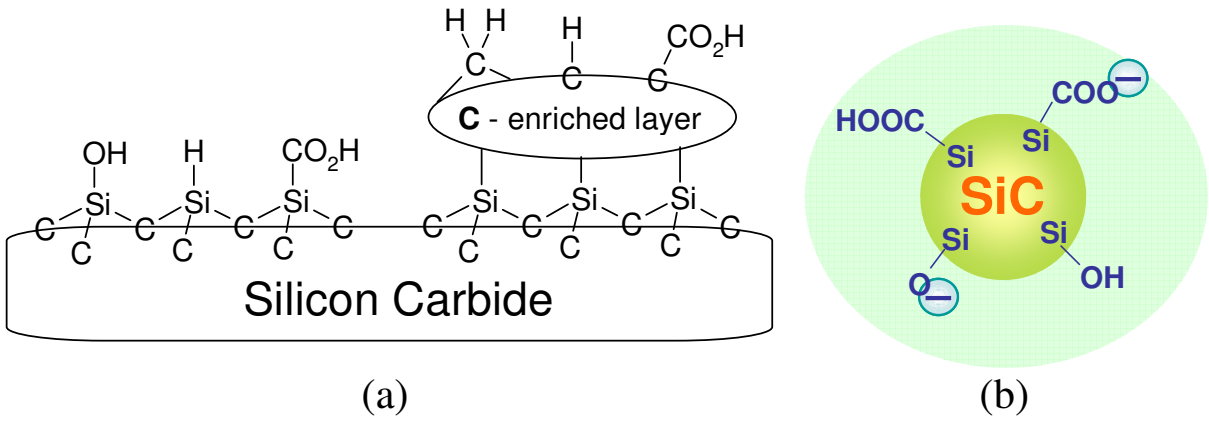

***Figure 3.9**: Schematic representation of (a) general surface chemistry of as-prepared SiC NPs and (b) surface charges of NPs dispersed in polar liquids.*

3.2.3.2. Nano-SiC obtained by laser ablation

Very rich surface chemistry of the SiC NPs obtained by laser ablation suspended in water was studied by means of IR absorption spectroscopy as shown in **Figure 3.10a**. The laser ablation technique probably induced the rupture of the Si-C bonds, rendering them extremely chemically reactive with water molecules and only low intensity signal can be detected in 782-794cm^{-1} region. For example, oxidation of the Si bonds in water is manifested by a very intense IR spectral band related to asymmetric stretching vibrations of Si-O bonds (1000-1150 cm^{-1}). A very wide band situated between 3000 cm^{-1} and 3600 cm^{-1} corresponds to stretching vibrations of O-H bonds at the NP/water interface, suggesting that the formed silicon oxide is quite well hydrated. The peak centred at 3670 cm^{-1} can be related to stretching vibration of O-H bonds isolated from the water environment. The isolated O-H groups are probably inside the formed NPs on silicon or carbon atoms. The absorption bands situated in 2900-3000 cm^{-1} spectral range and near 1250 cm^{-1} reveal the presence of different aliphatic CH_x groups.

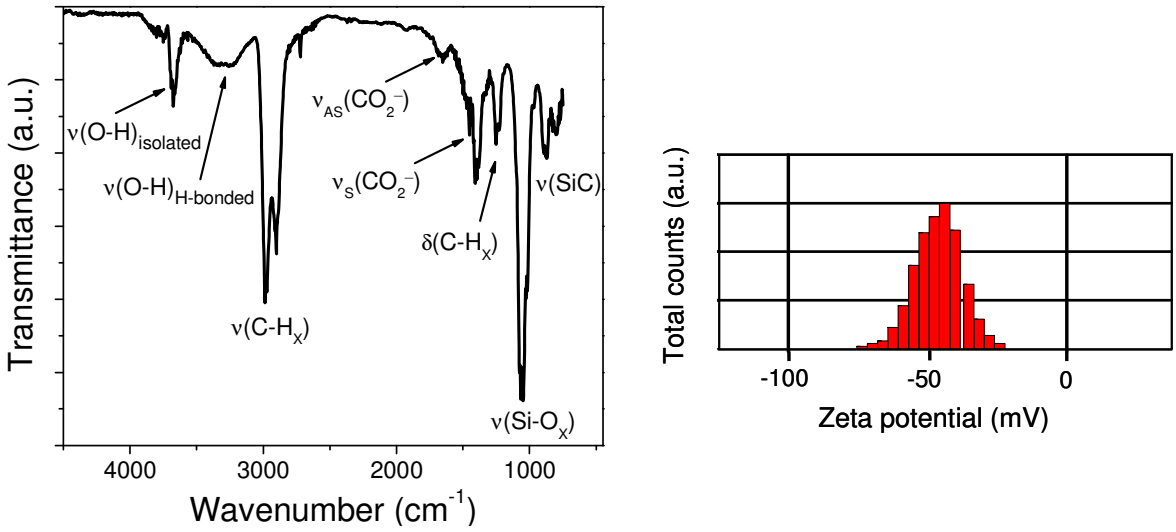

***Figure 3.10**: (a) FTIR spectrum of the SiC NPs suspended in pure water, (b) zeta-potential of the colloidal suspensions based on the SiC NPs.*

Two other specific bands centred at 1400 cm^{-1} and 1650 cm^{-1} correspond to carboxylate anions CO_2^- appeared at the NP surface after dissociation of carboxylic acid groups (—CO_2H) in water. Presence of the negative electric charges was quantitatively proved by measurements of zeta-potentials (-49 ± 13 mV) in the colloidal dispersions containing the suspended SiC NPs as it is illustrated by **Figure 3.10b**. This high value of zeta-potentials is at the origin of the high colloidal stability of the laser-produced particles.

3.3. Size dependent properties

As it was shown in Chapter 1, physical and chemical properties of NPs are significantly dependent on their size, shape and size distribution. Thus, the implementation of effective particle separation methods should be conducted for fundamental studies as well as for applications of NPs. Herein, two approaches for the separation of SiC NPs in liquids will be discussed.

3.3.1. Size segregation by filtration

Recently it was reported by Serdiuk et al. [5] an interesting size tuning method of luminescent silicon NPs. Basically, macro-porous free-standing silicon membranes were successfully used to separate particles only few nanometres in size. Scheme of similar filtering set-up used in this work can be seen in **Figure 3.11**. The porous Si membrane was mounted on a 1 mL cell filled with ethanol. The upper part represents drop of the initial ethanol solution with dispersed and highly concentrated SiC NPs. Since ethanol solution was present in the both cells and inside the pores, the SiC NPs in ethanol could migrate through the meso-porous network. During evaporation of ethanol and filtration procedure SiC NPs were supplied drop by drop to the upper part. Surface area and thickness of free-standing membrane was 0.8 cm^2 and 200 µm, respectively.

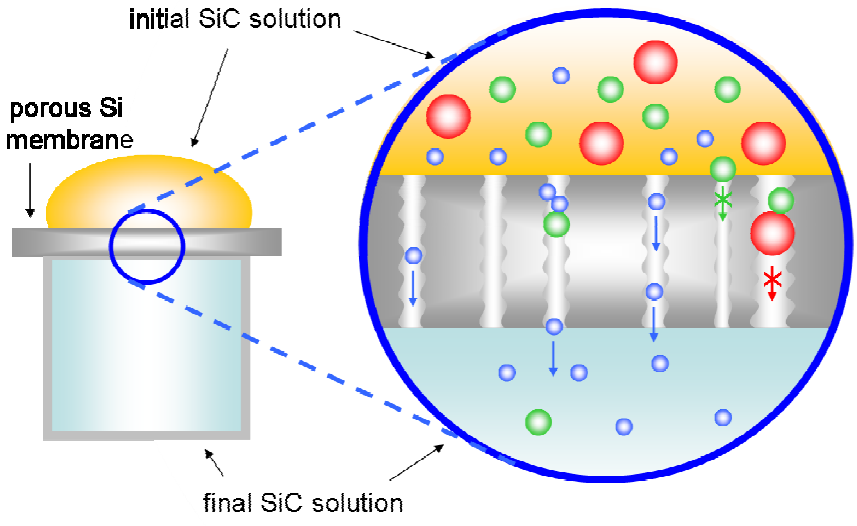

***Figure 3.11**: Schematic procedure of SiC NPs filtration via free-porous Si layers.*

By changing dimensions of the nanopores in Si layers, it is possible to control size of the particles, which can naturally diffuse through membranes to the receiver cell. Moreover, during the filtration process accumulation of large SiC NPs is likely to occur, leading to the additional auto-filtering of the NPs.

Typical PL spectra (λ_{ex}=343 nm) of original colloidal suspension (at high and low concentration) and filtered via two Si membranes with different pore dimensions can be seen in **Figure 3.12.** Initial NPs suspension at high concentration demonstrates double-feature PL peak centred around 490 nm. Previously [6], similar structure of PL spectrum was attributed to the presence of large and small NPs in the suspension. Firstly, short-wavelength (~400-470 nm) feature with corresponding transition energies higher than the bandgap of bulk 3C-SiC substrate stems from the quantum confinement effect. Secondly, intense long-wavelength shoulder (~480-550 nm) may be related to the band-band transition in medium-sized bulk-like NPs with spatial confinement of charge carriers (NPs size D>5-10 nm). Finally, intense emission in far under band gap spectral region is due to the localized energy states in the largest NPs (D>20 nm), as profoundly discussed in Chapter 1.

It is also worth noting, that excitation wavelengths play an important role on the visualization of PL signal from small and large NPs. Wu et al. [6] reported observation of excitation wavelength-dependent PL peak position of SiC NPs. When excitation wavelength was shorter than 350 nm, the PL spectra only showed a blue band at a fixed peak location. When the excitation wavelength was increased to 350 nm, an additional green band started to emerge as a shoulder. Although colloidal suspensions are different from discussed, the general tendencies remain. Thus, excitation laser at λ_{ex}=343 nm was chosen to be able to excite both small and large SiC NPs, and to maximize visualization of filtration effect.

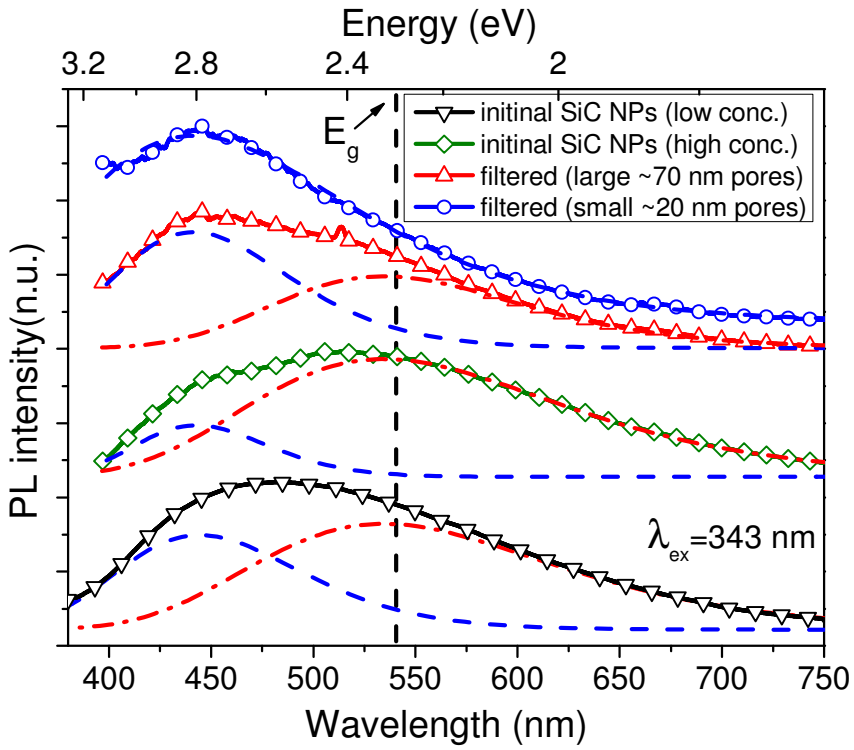

***Figure 3.12**: PL spectra of initial SiC NPs suspension at high and low concentrations, and after filtration via porous Si membranes.*

For clarity of the discussion, PL spectra were fitted by two Gaussians centred at 445 and 535 nm representing radiative transition in the small and large NPs, respectively. After filtration of SiC NPs through porous-Si layers one can observe changed ratio between these components leading to the blue-shift of PL peak (related only to the smallest NPs). The double-Gaussian fitting may be argued since it is somehow artificial and corresponds to transition in ensemble of NPs with possibly different by nature radiative channels; however, it appears to be reasonable enough for clear and simple interpretation of the observed filtration effect on the PL spectra. Despite the estimated value for the smallest pore size to be around 20 nm, efficient separation of small NPs (<5 nm) from NPs ensemble present in initial colloidal suspension is observed. As it was mentioned before, this above-threshold separation can be governed by auto-filtering of accumulated SiC NPs in porous layer.

Role of inner-filter effect should be considered for interpretation of observed spectral changes, as elucidated in **Figure 3.12**. Mainly, this effect is observed at high concentrations of absorbing NPs when reabsorption of light occurs. Reasonable spectral changes can be observed for very broad size distribution of SiC NPs with electronic transitions covering wide spectral range (400-700 nm). In this case, light emitted by small NPs at λ=400-470 nm is reabsorbed by large particles emitting at 500-700 nm. As the result, ratio between Gaussian components is altered and PL spectra are mistakenly attributed to the dominant presence of large NPs. Filtration via porous membranes naturally leads to the decreased concentration of SiC NPs in final suspension when compared to initial one. Thus, in order to clarify role of filtration and dilution, concentration of non-filtered suspension was further decreased. PL peak position remained unchanged at 470-480 nm, and could not be shifted up to 450 nm as for filtered samples. As the consequence, observed spectral changes of filtered suspensions can not be exclusively attributed to either filtration or dilution effects.

3.3.2. Size segregation by centrifugation

Second method used to segregate SiC NPs was by mean of centrifugation. As it was highlighted by Zheng et al. [7] spatial separation of small and large particles is a result of interplay between the electrostatic repulsion forces (f_R) and the short-range van der Waals attraction forces (f_A). As mentioned before, dissociation of the carboxylic (Si—COOH) and/or silanol (Si—OH) acid groups on the surface of SiC NPs leads to the appearance of negative electric charges, resulting in electrostatic interparticle repulsion, thus stabilizing the particles. Furthermore, the colloidal stability of NPs is known to decrease with increasing particle size.

This effect has been explained to arise from the increased interparticle van der Waals forces since f_A^L (large NPs) > f_A^S (small NPs) [7]. As the consequence, during centrifugation, increased rate of the interparticle interactions leads to much efficient precipitation for NPs with $f_A > f_R$.

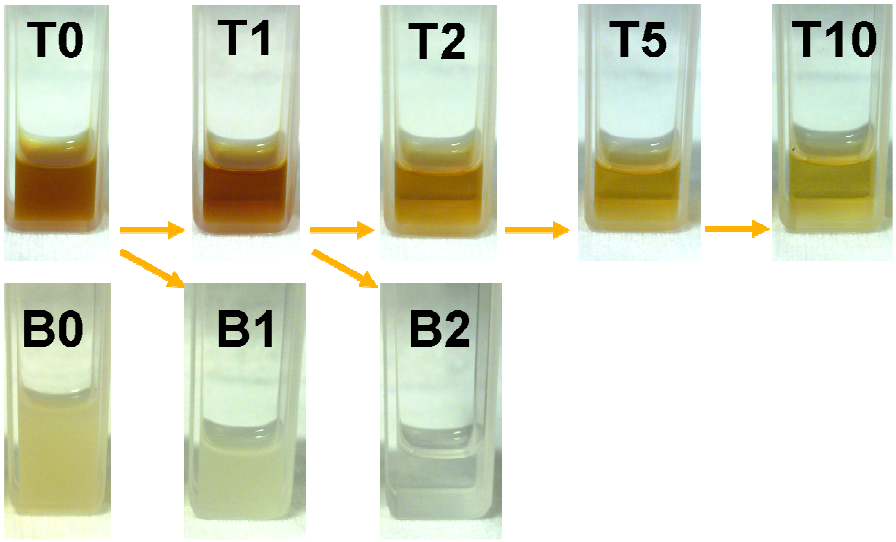

***Figure 3.13**: Images of initially collected supernatant and precipitated SiC NPs (T0, B0), and after centrifugation (T1-B1,T2-B2,T5,T10).*

Gradient centrifugation was implemented to gradually separate the biggest NPs from the initial highly concentrated SiC NPs suspension. In sample labelling, symbols "T" and "B", correspond to supernatant (top) and precipitate (bottom), respectively. The digits stand for acceleration (in thousands of "g") used during centrifugation to obtain the suspension. At the beginning, highly concentrated ethanol dispersion of SiC NPs was left for one week to collect first supernatant (T0) and naturally precipitated (B0) NPs. Afterwards, suspension T0 (2mL) was centrifuged at 1000 g for 15 min. Collected top part (T1) (1.8mL) was divided on two equal portions (2x0.9mL): to be used for characterization and for the next centrifugation with increased acceleration. The latter one was diluted to obtain once again 2mL of suspension. All samples with precipitated NPs (B0, B1, B2) were three times re-dispersed and centrifuged to wash out small quantities of supernatant. After centrifugation at 5000 g no precipitation was observed. In **Figure 3.13**, photos of suspensions and derivation scheme is presented. The decreasing optical density and corresponding colour (from dark brown to light yellow) for samples T1, T2, T5, T10 (T20 not shown) is due to the mentioned dilution. The precipitated NPs form opaque colloidal suspension with high degree of light scattering, while whitish colour indicates low light absorption in visible range.

3.3.2.1. Structural and chemical analysis

Single drops of last supernatant (T20) and precipitated dispersions were deposited on the carbon covered copper grid for TEM investigations. Typical TEM images of the corresponding samples can be seen in **Figure 3.14a** and **c** (for supernatant and precipitate, respectively). TEM image of the supernatant suspension (**Figure 3.14a**) systematically indicate the presence of layered objects surprisingly similar to carbon-based nanostructures like multiwalled carbon nanotubes and carbon onions [8]. EDX elemental analysis (**Figure 3.14b**) evidences carbon atoms while no reasonable signal for silicon atoms was detected. The carbon nanostructures have a lattice distance of 0.34 nm which corresponds to the (002) plane of graphite. On the other hand, NPs with sizes ranging from tens to few nanometres can be seen in TEM images obtained from the precipitated samples (**Figure 3.14c**). High intensity peak related to the silicon atoms in the EDX spectrum (**Figure 3.14d**) confirms observation of SiC NPs.

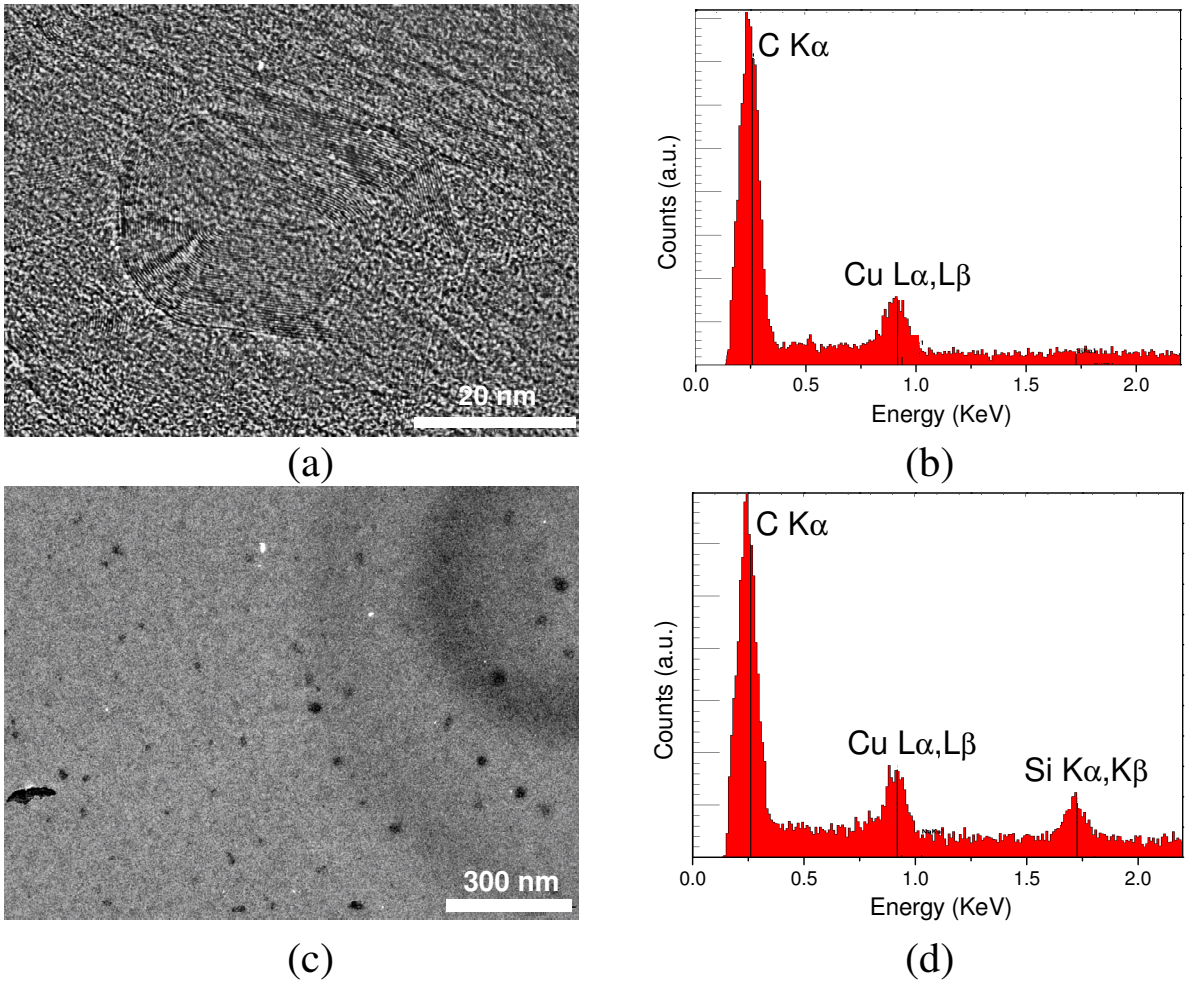

***Figure 3.14**: Typical (a),(c) TEM images, and (b),(d) EDX spectra of highly centrifuged samples ((a) and (b) for T20 ;(c) and (d) for B2).*

More general TEM image of the various carbon-based nanostructures found in the supernatant suspensions is shown in **Figure 3.15**. Most of the objects exhibit different irregular shapes and sizes ranging from few to tens of nanometres. More precise elemental analysis reveals that supernatant of highly centrifuged samples is composed of C 48.20 %, H 4.18 %, F 14.8%, Si <0.5% and the remaining 32.3% (calculated) is possibly oxygen, since no other elements should exist during preparation. Such small quantity of silicon atoms in the suspension explains that SiC NPs are undetectable by TEM. However they can be still present in the suspension due to rather moderate centrifugation speeds (20000 g maximum). Furthermore, large amount of oxygen and carbon can be bounded in form of carbon or graphite oxide. In the same time previously discussed carboxylic acid groups (COOH) can be present on the surfaces of both SiC and carbon nanostructures. In the latter case, surface density of these groups can be considerably higher (i.e. larger surface charge) ensuring stability against centrifugation, while heavier SiC in the same size range precipitates (**Figure 3.14a,c**).

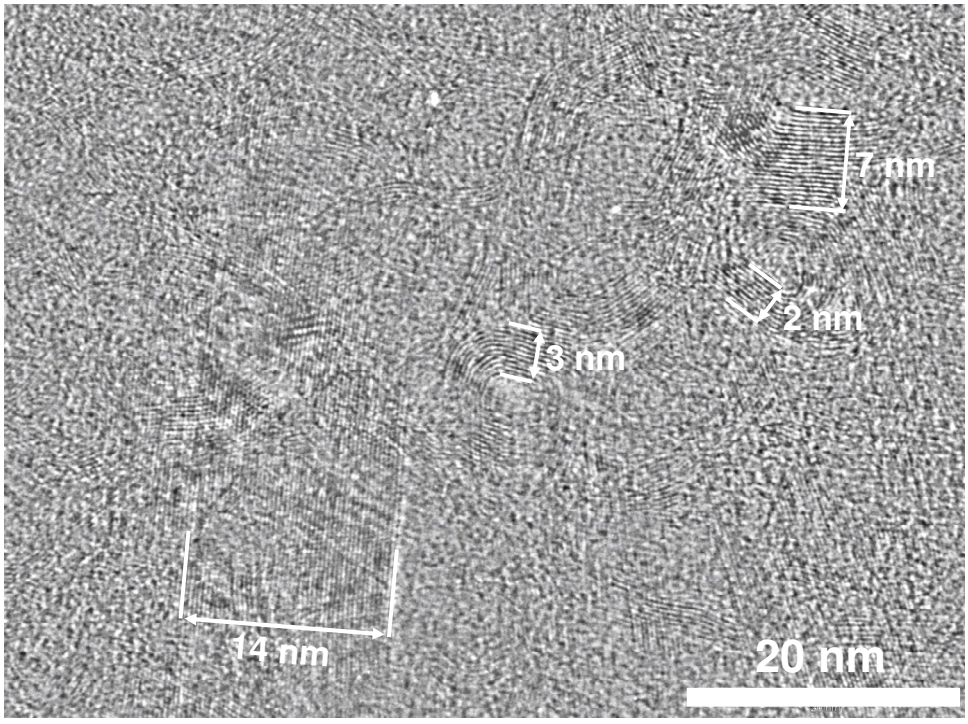

***Figure 3.15**: General TEM image of the dried supernatant suspension (T20).*

The most probable reasons lying in the formation of these carbon nanostructures are related to the polycrystallinity of the initial SiC bulk substrate. Depending on the orientation of the crystallites relatively to the electric current, regions with different levels of silicon atoms preferential removal consisting with either carbon or silicon carbide structures are created. Moreover, similar carbon nanostructures were obtained by the electrochemical

exfoliation of graphite electrode in highly ionic liquids [9]. Authors discuss several formation steps, which can be adopted for electrochemical etching of SiC substrate in HF electrolyte:

(1) Anodic oxidation of water produced hydroxyl and oxygen radicals.

anode: $H_2O \xrightarrow{-e} \cdot OH + H^+ \xrightarrow{-e} \cdot O + H^+$

The hydroxylation or oxidation of SiC by these radicals results in the formation of nanocrystals. The corrosion process occurs initially at edge sites, grain boundaries, or defect sites.

(2) The oxidation of the edge planes opens up the edge sheets, facilitating intercalation by the anionic F^-, which leads to the depolarization and expansion of the SiC.

(3) Oxidative cleavage of the expanded carbon sheets generates nanoribbons.

Finally, post-etching mechanical grinding of the dried porous layers leads to the additional structural changes.

TEM images of supernatant suspensions are in good agreement with previously discussed FTIR spectra of the initially prepared nanopowder (**Figure 3.8**) evidencing graphite formation (sp^2 carbon), since a peak at 1624 cm^{-1} arising from a conjugated C=C stretching vibration can be observed [10].

In summary, after electrochemical etching of SiC substrate, obtained nanopowder contains high amount of carbon based structures. During natural or centrifugation-induced precipitation of dispersed nanopowder in solvents large amount of SiC nanostructures is segregated from carbon-based materials found in the supernatant. Nevertheless, small-sized SiC NPs still remain in the supernatant manifesting by the relatively small amount of silicon atoms (<0.5%) evidenced from elemental analysis. It is possible, that in initial nanopowder both SiC and carbon phases form a single nanostructures, which during centrifugation are spatially separated in a liquid due to different densities and thus are affected by different values of centrifugal forces.

3.3.2.2. UV-Visible spectroscopy

Series of supernatant and precipitated suspensions were diluted for further investigation by UV-Vis spectroscopy. Extinction and absorption spectra of T0, T1, T2, T5, B0 can be seen in **Figure 3.16a,b**, respectively. All of the supernatants spectra were corrected by dilution parameters to correspond to a constant concentration. Absorption and extinction spectra of

B1, B2 samples are not presented due to very low absorption intensities. Regarding sample B0, extinction and absorption levels should not be compared to the ones for supernatants, since concentration correction factor can not be estimated.

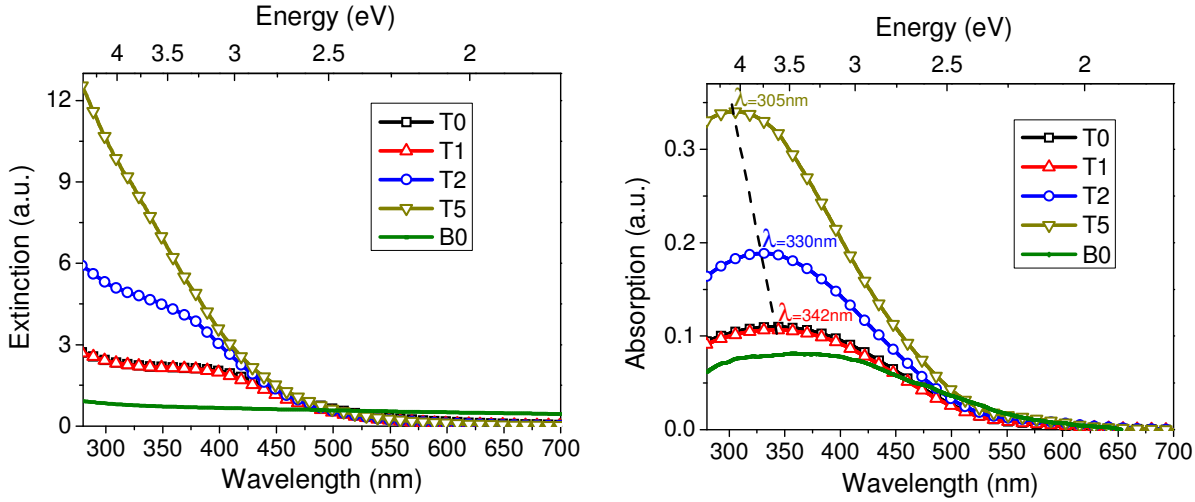

***Figure 3.16**: Extinction (a), and absorption (b) spectra of initial and centrifuged suspensions.*

Extinction spectrum of the initial suspension (T0) presents a shoulder around ~ 400 nm which turns into plateau at ~350nm and then monotonically increase at shorter wavelengths. Initial precipitates are manifesting in monotonic increase of extinction with no significant spectral features. When extinction spectra are compared with corresponding absorption spectra (**Figure 3.16 a,b**) one can remark slight differences. From one side, rising continuum at shorter wavelengths is not present in absorption spectra. This discrepancy is caused by a Rayleigh scattering which is proportional to the inverse fourth power of the wavelength (λ^{-4}) manifesting in the extinction spectra (extinction=absorption + scattering). Secondly, an intensity enhancement and a blue-shift of the absorption band are also observed after successive centrifugations. However its spectral positions for extinction and absorption spectra are shifted by almost 50 nm (~400 versus 350 nm, respectively). Observed spectral deviation can be understood in terms of resonance light scattering (RLS) observed in aggregates of absorbing species [11].

In general, two processes occur when light passes through a suspension of aggregates. If the solvent itself is non absorbing, energy is removed from the incident light through absorption and scattering by the aggregates. The light scattering component is a consequence of differences in polarizability between the aggregates and the solvent. The incident electromagnetic wave induces an oscillating dipole in the assembly, which radiates light in all directions. The ratio of the rate of energy absorption from the incident beam to the intensity of

the incident beam is called the absorption cross section, C_{abs}. The ratio of the rate of energy scattering out of the incident beam (in all directions) to the intensity of the incident beam is called the scattering cross section, C_{sca}. If the induced dipole can be considered ideal, which is usually a valid assumption if the size of the aggregate is small compared to the wavelength of the light in the solvent λ_m, both cross sections are related to the polarizability of the aggregates in simple ways:

$$C_{abs} = k_m \alpha_i \tag{3.1}$$

$$C_{sca} = \frac{k_m^4}{6\pi}|\alpha|^2 = \frac{k_m^4}{6\pi}(\alpha_r^2 + \alpha_i^2) \tag{3.2}$$

, where k_m is the wave vector of light in the solvent, $k_m = 2\pi/\lambda_m$, and α_r and α_i are the real and imaginary parts of the polarizability of the aggregates. Absorption at a certain wavelength band by a suspension of aggregates can be understood as the result of a maximum in the imaginary part of the polarizability in that region of the spectrum. On the other hand, the absorbance A of a sample is proportional to the number of aggregates per unit volume (N/V). The real and imaginary parts of α are related to each other, so that when α_i is maximized in some wavelength range, α also behaves anomalously in this region, which also results in increased scattering. Under normal conditions this increased scattering is difficult or impossible to detect because of the increased absorption and the weakness of the enhanced scattering effect. However, when this effect is investigated for aggregates of chromophores, the enhanced RLS can be enormous. The absorption depends on the first power of the polarizability, which in turn depends linearly on the volume of the aggregate. Thus, a suspension with a fixed concentration of the aggregating component will exhibit no change in absorption as aggregation occurs, because the product of N/V and α_i remains constant. However, the amount of scattering depends on the square of the volume of the aggregate, and thus it increases as a consequence of aggregation; RLS is therefore extremely sensitive to even low concentrations of extended aggregates.

These considerations suggest a model, where gradient centrifugation induces de-aggregation and/or fractioning of the absorbing elements leading to the vanishing of RLS in extinction spectra. In present case absorption maximum of the aggregated structures is situated in ~350 nm region and RLS manifests at near spectral region of ~400 nm in the extinction spectra. However theory of RLS in the simplest form is based on the assumption that absorption intensity and spectral features are not a function of aggregation state. It is

somewhat opposite to the changes observed after centrifugations (**Figure 3.16 b**). Following reflections complement the understanding of the involved physical processes and clarify the possible origins of this absorption band and its increasing magnitude at higher centrifugations strengths.

i) Large amount of oxygen from the elemental analysis points out the oxidized state of the observed nanostructures. Hence from TEM structural analysis one can state that they look like graphene/graphite oxide (GO) structures. It can be expected that oxidation produced a disruption of the graphene π network and opened a direct electronic band gap, and that the size of these gaps will increase with the degree of oxidation [9].

ii) The main absorbance peak attributed to π– π* transitions of C=C in as-synthesized GO occurs at around ~200 nm, which red shifts to ~260 nm upon reduction. A shoulder around 320nm observed for as-synthesized GO was attributed to n– π* transitions of C=O [15, 17]. A higher graphitization degree induces a red-shift of the absorption resulting from the enhanced degree of π conjugation and the decreased band gaps [10]. The calculated energy gap of π– π* of C=C is shown in **Figure 3.17** [12]. One can see that size variation of nanostructures leads to the transition energies covering UV-visible spectral range.

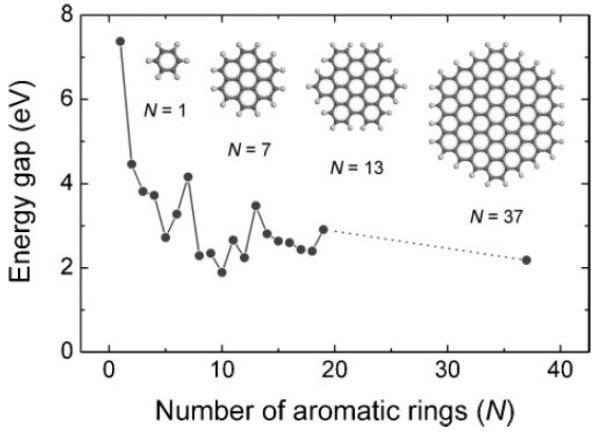

***Figure 3.17**: Energy gap of π– π* transitions calculated based on Density Functional Theory as a function of the number of fused aromatic rings (N). The inset shows the structures of the graphene molecules used for calculation [12].*

In current studies, the broad absorption spectra that extend up to 500-600 nm indicate the absence of a well-defined bandedge. Since the bandgap depends on the size, shape, fraction of the sp^2 domains, and level of oxidation, one can assume that observed optical properties are related to carbon structures seen in TEM images, while absorption level of SiC structures is considerably lower due to low concentration of the related structures. Together with increased RLS in initial suspension, blue-shifted and increased absorption levels upon centrifugation are related to the fractioning and detaching of carbon-based nanostructures

from the initial complex carbon-SiC hybrid structures. Emphasized role of SiC in observed spectral and intensity changes can be understood since absorption band of precipitated SiC NPs is similar to the one of aggregated carbon nanostructures (B0 in **Figure 3.16b**). Probably this band can be attributed to the small sp^2 carbon clusters attached to the surface of SiC NPs still present in precipitate. SiC can play additional role by changing effective dielectric environment of carbon structures lowering energy (red-shifting) and oscillator strengths (lower absorption) of the electronic transitions in SiC-carbon complexes. Nature of this interaction is still unclear and should be subject to additional studies.

3.3.2.3. PL spectroscopy

Extra optical properties of the centrifuged suspensions were studied by PL spectroscopy as shown in **Figure 3.18**. All samples were diluted in ethanol to compare low concentration suspensions where concentration dependent spectral changes do not occur. Measured spectra were normalized and shifted by a constant value for clarity. Only slight spectral shift (<20 nm) can be observed for samples B0->B2 and T0->T20. No additional spectral changes like peak broadening can be deduced from spectra. Similarities of peak positions in both precipitated (B0, B2) and centrifuged (T0, T20) samples suggest common nature of the observed PL.

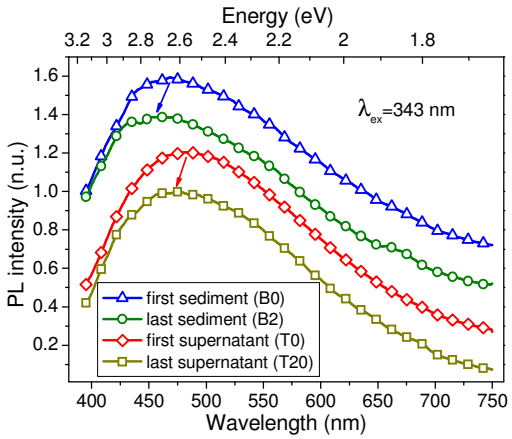

***Figure 3.18**: PL spectra of first and last sediment and supernatant suspensions.*

It is worth to remark that PL maxima (~450-470nm) are located far above corresponding bandgap of SiC substrate (~540 nm). It is even more surprisingly for naturally sediment sample (B0), where only the biggest SiC NPs with bandgap energy emission should be found. This observation is probably related to an appearance of small structural features in fragments of nanoporous network with interconnected NPs, which were not transformed into small NPs (carbon and/or SiC) during nanopowder preparation. Very low PL intensity was observed from the sample supporting this assumption, since larger nanostructures favour

higher delocalization of created electron-hole pairs. After centrifugation for sample B2 with sediment, SiC NPs manifest in slight spectral shift. On the other hand for the supernatant suspension only the smallest SiC NPs should be observed. For this sample (T20) more probable is recombination in carbon-based nanostructures due to the relatively higher concentration of carbon found in supernatant. Moreover, PL in wide UV-vis spectral region was reported for similar carbon structures [9-10,12-15].

For example, PL spectra of the carbon NPs are generally broad and dependent on excitation wavelengths, which have been attributed to the size heterogeneity and distribution of different emissive sites on the carbon NPs [9]. Further in some reports, the difference in emission lights was attributed to the excessive growth of graphite nanodomains in carbon nanostructures, which led to the continuous red shifts of fluorescent emissions (even to no fluorescence) by much larger carbon components [10]. Previously discussed absorption bands were also correlated with observed PL due to the energy gap between the π and π^* states which generally depends on the size of sp^2 clusters or conjugation length [12]. Thus, authors expected increase in the PL intensity without energy shift during the initial sample preparation due to the increased concentration of such sp^2 fragments. Furthermore, the subsequent PL quenching with larger structures may be the result of percolation among sp^2 carbon clusters, facilitating transport of excitons to nonradiative recombination sites. In case of the PL from carbon dots authors emphasized that it may be attributed to the presence of surface energy traps that become emissive upon stabilization as a result of the surface passivation. Additionally, a large surface-to-volume ratio in a particle is necessary in order to observe strong influence of surface passivation upon PL. There was experimental evidence supporting such a mechanistic argument. Larger carbon particles (30-50 nm in average diameter, for example) with the same surface passivation were found to be much less luminescent. Conversely, it might be expected that even higher PL quantum yields can be achieved in smaller carbon dots with the same or similar surface morphology and passivation [14]. Previously discussed filtration via porous membranes may favours segregation of large SiC-carbon and/or carbon clusters that supports model where large structures are responsible for spectral broadening of PL peak to IR region (see **Figure 3.12**).

3.3.2.4. PL quantum yield measurements

The luminescence quantum yields (QY) of the supernatant suspensions (T0, T1, T2) were measured against an ethanol solution of rhodamine 123 (QY=0.9 [16]) as presented in **Figure**

3.19 (λ_{exc}=343 nm). Very low QY of T0 sample is suggested by high laser absorption (lower scattering) in comparison with rhodamine, while PL intensity remains much lower (see insets in **Figure 3.19**). For T0, T1, T2 samples calculated QY gives 0.56%, 0.57%, 0.74%, respectively. As one can see, increased centrifugation value leads to QY rise. From one side, it can be related to the enhanced absorption in UV region by higher concentration of small carbon clusters. As discussed before, they can carry higher QY due to localization of e-h pairs, resulting in overall increase of calculated QY. On the other hand, centrifugation leads to elimination of the biggest SiC NPs from the suspensions. QY of these particles is rather low (far below detection limit of the system) since resembles QY of bulk material (with indirect bandgap). In the consequence, precipitated NPs lower overall QY (before centrifugation).

Calculated values are around 20 times lower when compared to the reported QY for similar SiC NPs (17%) obtained by electrochemical etching of bulk substrates [17] and around 10 times lower than other carbon nanomaterials QY [9, 14-15]. In general, higher QY reported in the literature can be explained by different fabrication and treatment procedures involved. For example PL QY of the surface functionalized carbogenic QDs was about 3%, and virtually independent of the excitation wavelength in the 400–500 nm range [15]. Another investigations of surface passivated quantum-sized carbon dots at 400 nm excitation, communicate QY from about 4% to more than 10%, where the variation were probably dependent on the effectiveness of the reaction for surface passivation [14]. The exfoliated carbon NPs produced in water-poor ionic liquids had strong PL with a QY of 2.8-5.2% (emission window extending from 400 to 600 nm) [9].

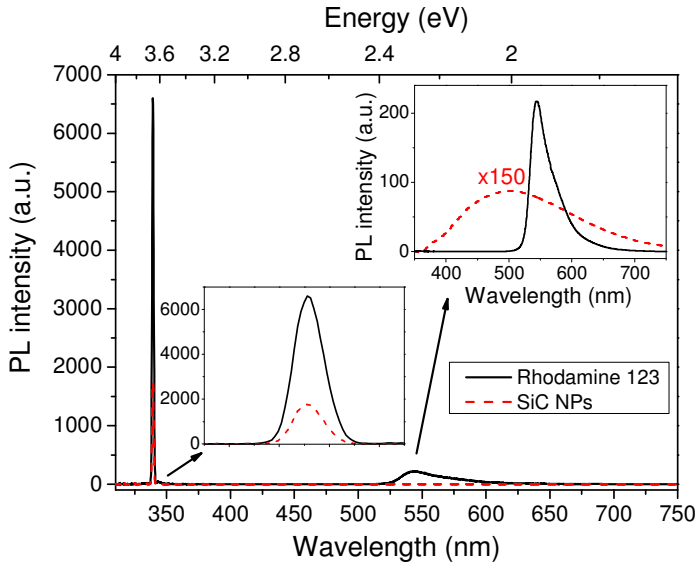

***Figure 3.19**: Spectrally corrected laser scattering peaks and emission spectra for ethanol solutions of Rhodamine 123 and SiC NPs (T0). Corresponding spectral regions are magnified in the insets.*

3.3.2.5. PL comparison of as-prepared dry and oxidized SiC nanopowder

To facilitate interpretation of PL signal in UV-blue spectral region carbon structures were eliminated by thermal annealing (at 400 °C in air for 1 h) of the as-prepared SiC nanopowder. Images of as-prepared and annealed porous SiC layers can be seen in **Figure 3.20**. One can remark colour changes after thermal treatment. Interestingly, similar colour differences can be observed in supernatant and sediment suspension after centrifugation.

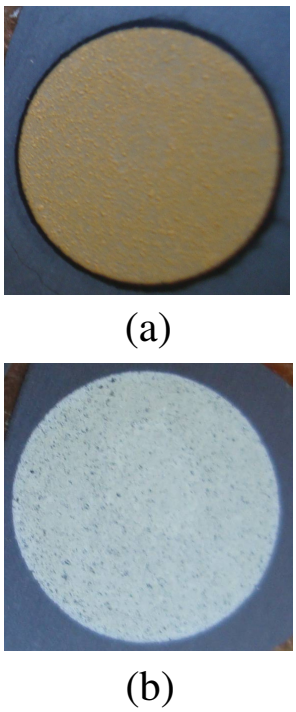

***Figure 3.20**: General view of as-prepared (a), and annealed (b) porous SiC layer.*

First of all, the room temperature PL measurements on dry as-prepared and annealed nanopowders were performed and compared with the PL signal from bulk polycrystalline 3C-SiC wafer. The corresponding PL spectra are shown in **Figure 3.21**. The dashed vertical line represents the energy gap of the bulk material (Eg). In comparison to the PL signal of the bulk polycrystalline wafer, the PL intensity of the as-prepared SiC nanopowder is more than 1000 times higher and the spectral position of its PL peak is slightly shifted toward lower energies. Nevertheless, the high-energy tail (>Eg) of the PL spectrum is well pronounced. After low temperature oxidation of the nanopowder, the PL peak maximum is considerably blueshifted and is situated above the Eg. Though the PL intensity of this peak is remarkably lower than the intensity of the as-prepared sample, it still remains much higher than the PL signal obtained from the bulk wafer.

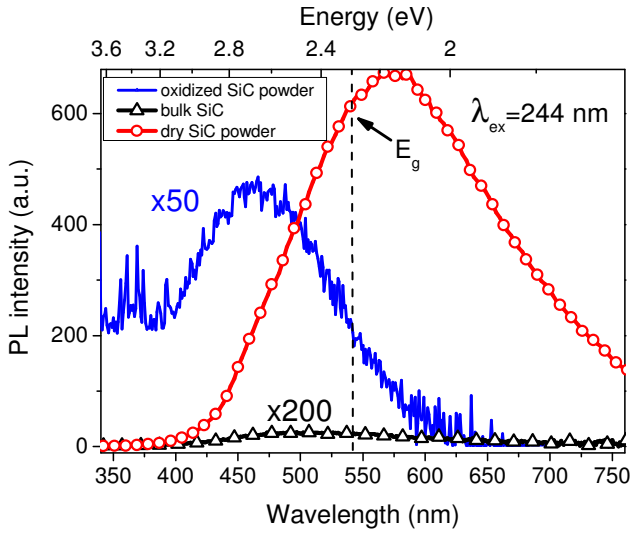

***Figure 3.21**: PL spectra of dry as-prepared and oxidized SiC nanopowder compared to polycrystalline 3C-SiC wafer.*

In general, much higher PL intensities of the nanopowder compared to the PL of the bulk substrate all over the spectral range can be explained by the spatial confinement of the photogenerated charge carriers inside the very small NPs. The high PL signal with energies <Eg can be associated with radiative recombination processes involving deep defect and/or surface states in the as-prepared nanopowder [18]. Especially radiative recombination via numerous localized energy states related to the huge specific surface of the SiC nanopowder may explain the increased integrated PL intensities compared to the very poor PL signal detected from the initial bulk substrate [18]. In addition, PL from bulk polycrystalline substrate is quenched especially due to nonradiative states corresponding to the grain boundaries, which are suppressed in the nanopowder. Oxidation induced passivation of the radiative surface states leads to their elimination from the energy band gap and, consequently, to almost complete extinction of the PL signal with energies <Eg, as it can be seen in **Figure 3.21**. At the same time, the low temperature oxidation ensuring formation of a rather poor quality oxide shell can provoke appearance of numerous new nonradiative states leading to the decrease in the whole integrated PL intensity. The PL signal above the band gap (>Eg) can be attributed to the recombination of quantumly confined photogenerated charge carriers in small NPs constituting the nanopowder or to some radiative defects in the formed oxide sheet. To check this point the formed surface oxide layer was removed by HF-based solutions. No changes in the PL spectrum were detected (not shown). Thus, one can conclude that the PL signal is provided by radiative recombination of the charge carriers inside the SiC core.

3.3.2.6. PL comparison of SiC NPs obtained by electrochemical etching and laser ablation

Figure 3.22 shows room temperature PL spectra of the SiC NPs prepared in water at four different laser powers. PL signal from water without the NPs is given for comparison. One can state that the PL intensities increase with laser power. Maximum values of all the detected PL spectra are centred at 440 nm (2.8 eV) and corresponding energy is higher than the band gap value (E_g) of the bulk 3C-SiC substrate (2.3 eV). The PL signals above the E_g value can be attributed to the recombination of quantumly confined photogenerated charge carriers in SiC NPs.

Since no shift of the PL spectral maxima is detected for different ablating laser powers, one can suppose that the size distribution of the formed SiC NPs is independent on

the laser power which influences only the NPs concentration in water. The non-negligible PL intensities with energies $<E_g$ can be associated with radiative recombination processes involving band tails, defect and/or surface states. The defect states can correspond to the discussed above defects visible in **Figure 3.4d** and the radiative recombinations via the surface states can be related to the defects present at the huge specific surface of the formed SiC NPs with dimensions < 5 nm. Nevertheless, relative PL intensity in this region is considerably lower in comparison with PL signal of NPs obtained by electrochemical etching. On the one hand, laser ablation leads to the formation of exclusively SiC NPs which due to the small sizes exhibit PL in above 3C-SiC bandgap energy region; on the other hand, electrochemical etching leads to the high content of carbon-based nanostructures which significantly manifest in the under 3C-SiC bandgap part of PL spectra.

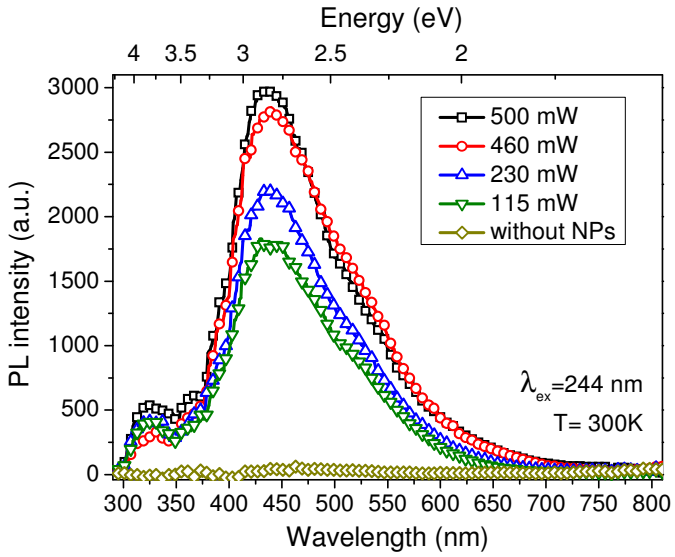

***Figure 3.22**: Room temperature PL spectra of colloidal suspensions containing SiC NPs formed by laser ablation at four different laser powers.*

An interesting PL spectral particularity, which is not connected to the discussion on carbon species presence, can be observed in the 300-350 nm wavelength range. Small peaks centred at 322 nm (3.85 eV) can be observed for all three laser ablation powers. Since the spectral position of these peaks is very similar to the PL spectrum of 6H-SiC NPs obtained by electrochemical etching [19], one can speculate that a very small amount of the formed SiC NPs described in this work were transformed during the laser ablation treatment from cubic crystalline structure (3C) of the initial bulk substrate to hexagonal structure (6H, for example). A similar effect was already observed during laser ablation of Ti in liquid environment [20]. The main physical reasons for such a laser-induced structural transformation of the NPs are: (i) huge energy coming from the ablating laser and (ii) enhanced elasticity of the smallest SiC NPs for such a structural re-organization. However,

since hexagonal structural ordering is more complicated in comparison with cubic one, only a small amount of the 6H-SiC NPs can be created in such a way.

3.3.2.7. Nonlinear optical properties

Nonlinear optical properties of T0 and B1 suspensions were experimentally investigated by SHG and TPPL measurements (excitation laser λ=800 nm, τ=100 fs) on a samples prepared by single drop drying on a glass cover slip. Corresponding microscope images are presented in **Figure 3.23.** Initial supernatant suspension T0 (**Figure 3.23a**) demonstrates high emission signals around SH wavelength (λ=395 nm) and at 600 nm (TPPL process), while first precipitated suspension B1 (**Figure 3.23b**) exhibits only SHG with practically the same intensity as T0. As discussed in Chapter 1, SiC possess good nonlinear optical properties, which can be enhanced by nanostructurization. Therefore, high SHG intensities observed in both suspensions are due to the presence of SiC NPs.

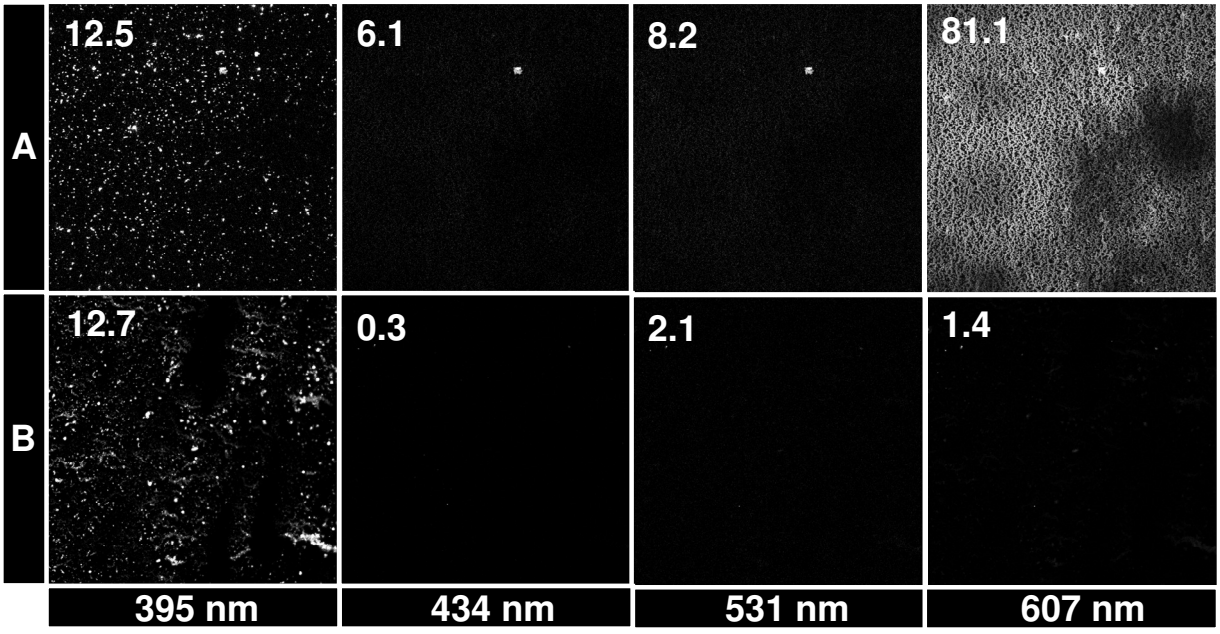

Figure 3.23*: Room temperature SHG (395 nm) and TPPL (434, 531, 607 nm) microscopy images (317x317 μm^2) and corresponding luminosities of (a) initial supernatant (T0) and (b) first centrifuged sediment suspension (B1) excited with pulsed 800 nm (τ=100 fs) laser.*

It should be noted, however, that there are also number of theoretical and experimental studies reporting on nonlinear optical properties of carbon-based materials like HHG in carbon nanotubes and graphite/graphene films [21-25]. Especially, the presented nonlinear properties have been attributed to the structural properties since nonlinear phenomena related to the second-order nonlinear susceptibility are not allowed in centrosymmetric crystals. In

view of a diversity of carbon nanostructures observed in supernatant (see **Figure 3.15**), featuring different symmetry ruptures at the scale of the single objects with broad size distribution, one can expect high nonlinear response. Nevertheless, SHG in the suspensions are likely to be SiC-related due to higher bulk nonlinear response of SiC.

Remarkably, no TPPL (λ=434, 531, 607 nm) signal can be detected for B1 suspension. Physical reasons of such low TPPL signal in comparison with T0 sample is related to the fact that TPPL is a two step process composed of nonlinear two-photon absorption and radiative recombination of the created e-h pairs. In the latter case as it was shown previously, PL QY of precipitated SiC NPs is rather low, and after centrifugation relative amount of carbon nanomaterials with high QY has increased.

3.3.3. Model of nanostructured SiC size-dependent properties

To summarize observed results concluding interpretation based on the following statements and assumptions should be described in details.

Near-field interactions between carbon and SiC electronic structures were confirmed by centrifugation-induced blue-shifted and enhanced absorption band of supernatants (**Figure 3.16**).

Depending on the size of carbon and SiC nanostructures these interactions manifest in various changes all over spectral range. For example, for large carbon and/or SiC NPs red-IR changes are evident by:

i) Filtration-induced blue-shift of PL (**Figure 3.12**).

ii) PL comparison of annealed in oxygen ambient and dry SiC nanopowder (**Figure 3.21**).

There are several indications on the optical properties congruence in UV-blue spectral region with presence of small NPs:

i) Previously reported PL of carbon-based nanostructures [9-10, 12-15] and quantum confinement effects in SiC NPs [6, 26-28].

ii) PL peak of SiC NPs obtained by laser ablation is centred at around 440 nm (**Figure 3.22**)

iii) PL peak of annealed SiC nanopowder in oxygen ambient is centred around 470 nm(**Figure 3.21**)

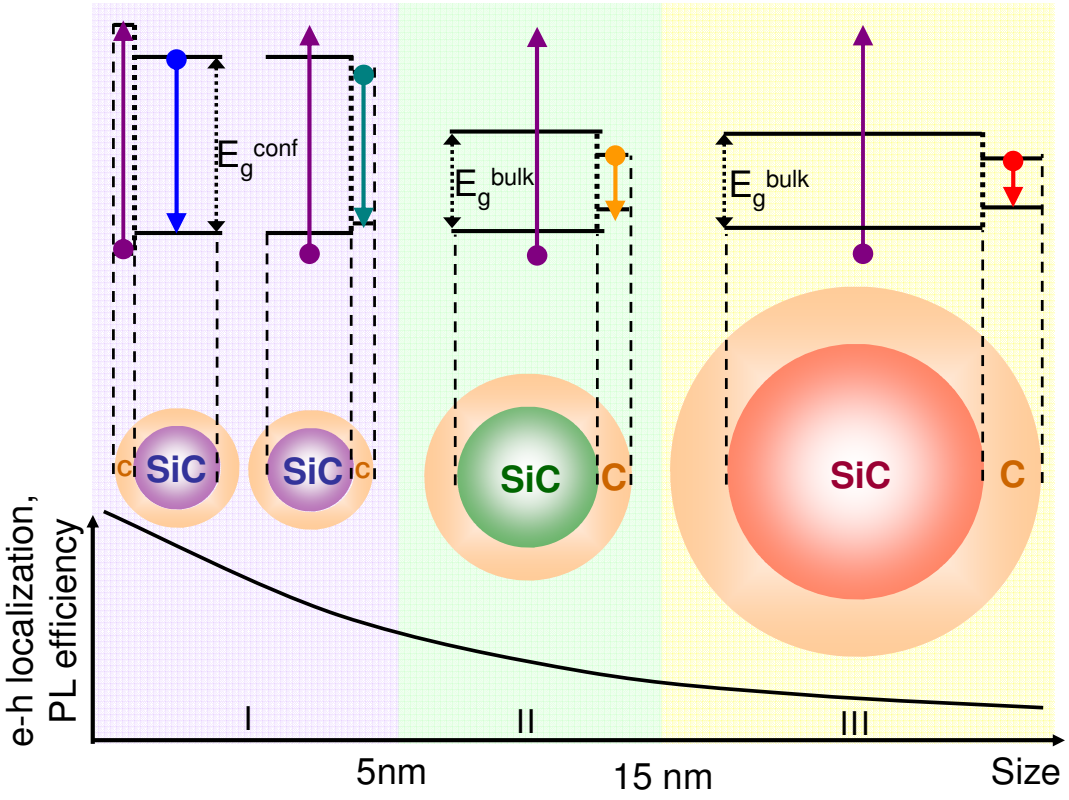

***Figure 3.24**: Schematic interpretation of the observed optical processes as a function of nanostructure size.*

Schematic of various radiative recombination channels for different sizes and interacting nanostructures is described in **Figure 3.24.** It can be easily expanded to the separated carbon or SiC components; however size dependence should remain the same. Proposed scheme is divided onto three region arbitrary corresponding to three characteristic size ranges. For the largest NPs (region 3), absorbed energy (upward arrow) is converted to e-h pair (not localized) where the probability of radiative recombination is low, however they can recombine more efficiently when trapped at localized energy states caused by carbon nanomaterials (downward arrow). For the medium-sized NPs (region 2), spatial confinement is possible, and band-to-band transition of bulk SiC is observed. Additionally, recombination via surface states is enhanced due to increased surface to volume ratio. Finally, for the smallest NPs (region 1), quantum and spatial confinement effects lead to increased above-bandgap light emission. Since optical properties of carbon nanoclusters and SiC NPs in this size range can be extremely sensitive to slight size and shape deviations it is worth to assume that both can behave as absorbing and luminescent sites.

Although proposed scheme is somehow simplified, it is in a perfect agreement with the numerous experimental results. Thus, model of interacting carbon and SiC NPs will be applied for future discussions on the observed optical properties. Importance of the surface

interactions should not be neglected. For instance, pure SiC NPs as can be seen from PL spectrum of oxidized SiC nanopowder (**Figure 3.21)** demonstrate low efficient luminescence with maximum at 470 nm. When carbon nanomaterials are introduced into system of SiC NPs, PL peak is red-shifted with increased intensity (compare with dry initial SiC nanopowder). These spectral changes can be related to purely additive role of carbon materials, i.e. they only add increased PL signal all over the spectrum. On the other hand they can enhance radiative emission by introducing additional localized energy states. Similar use of carbon nano-variations were reported for enhanced light emission in ZnO/carbon nanostructures [29]. Carbon-based molecules can also play a role of surface passivating agents, as it is in the case of organically capped Si NCs [30].

3.4. Local field dependent optical properties

It is now becoming clear that carbon-SiC interaction plays an important role in the optical properties of SiC NPs. The control of optical features via manipulation with electronic wavefunctions is also promising. Firstly, the inherited surface charges during dissolution in polar liquids and external local fields associated change both electron and hole localization in NPs. Secondly, the dielectric environment leads to altered internal fields manifesting in additional dielectric electron-hole confinement and changed binding energies of excitons and localized energy states. Although these approaches are based on similar local field effects, their combined contribution can show rich phenomena, which manifest differently depending on the studied nanostructures. In this section, both aspects of dielectric confinement and local fields induced by external charges will be discussed in details.

3.4.1. Environmental effect

In order to investigate the role of surrounding media with different dielectric constant, the same quantity of nanostructured SiC powder was dispersed in three different solvents: dichloromethane (ε_{static}=9.1), ethanol (ε_{static} =24), and water (ε_{static} =80). The approximate concentration of NPs in the suspensions was 0.05 mg/mL. **Figure 3.25a** shows absolute PL spectra of the SiC NPs dispersed in these solvents. No spectral changes can be observed in PL spectra for different solvents. This behaviour is in agreement with the results reported by Fan et al. [26], but in contrast to those reported by Beke et al. [27] where solvent polarity rise results in a PL emission red shift. On the other hand, opposite dielectric effect was reported

for porous Si nanostructures in which a blue-shift of the PL was observed when the samples were wetted by a solvent with high dielectric constants [31] or embedded in a polymer [32]. Considering a hydrogenoid impurity model, Timoshenko et al. [33] showed that in the case of mesoporous Si layers, the increased effective dielectric constant of the medium (solvent+NPs) leads to an important ionization energy decrease in the donor- and acceptor-like energy states inside the energy band gap.

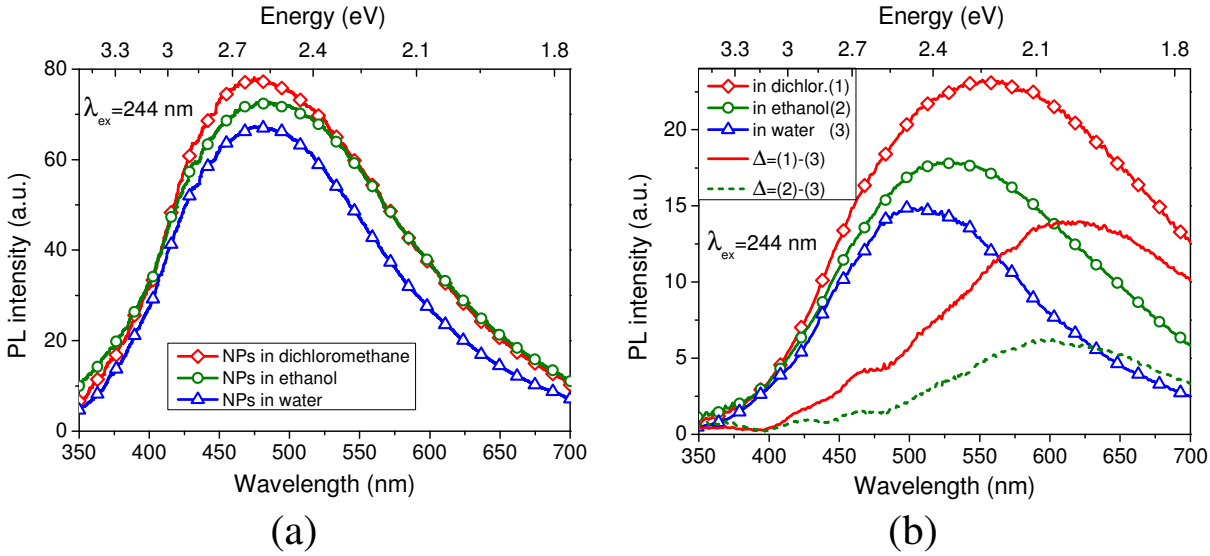

***Figure 3.25**: PL spectra of the (a) low and (b) high concentration SiC NPs suspensions with different static dielectric constants: dichloromethane (ε_{static}=9.1), ethanol (ε_{static}=24), and water (ε_{static}=80).*

As discussed before, most of the localized energy states manifesting in above bandgap PL signal are localized in large NPs. Thus, one could expect that the role of dielectric environment on PL will be pronounced in large NPs. In order to optically "activate" these large NPs in comparison to small ones, concentration of NPs in suspension was increased. In this case, under same excitation condition (λ=244 nm) large NPs signal rise up over small NPs one due to discussed concentration/inner filter effect. As the results, PL spectra for concentrated (~1mg/mL) SiC NPs suspensions with variable dielectric constant can be seen in **Figure 3.25b**. In particular, the higher the dielectric constant is, the thinner and, therefore, more blueshifted the corresponding PL peak is. Indeed, the full widths at half maximum of the PL peaks for dichloromethane, ethanol, and water are equal to 1.16, 1, and 0.8 eV, respectively. Especially, a much more important influence of the solvent nature on the below-gap PL intensities with energies <Eg is clearly visible. To facilitate interpretation of this broadening, PL spectrum of SiC NPs in water was subtracted from corresponding spectra obtained for ethanol and dichloromethane. Apparently, increased density of states at around 600-650 nm is responsible for the spectral changes.

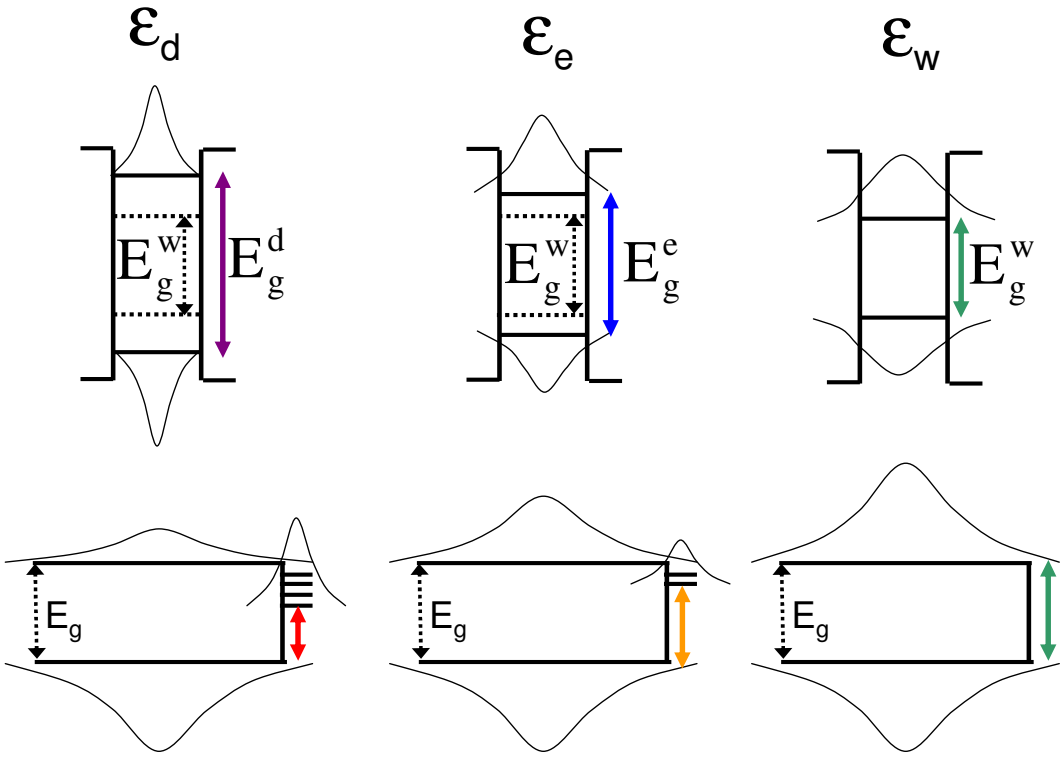

***Figure 3.26**: Schematics of the polarity influence for dichloromethane ε_d (first column), ethanol ε_e (second column), and water ε_w (third column) in small (top row) and large (bottom row) NPs. Illustrative electron/hole wavefunctions are represented by thin solid lines. The arrows indicate possible channels for the electronic transitions.*

The observed effect as well as diversity of those reported in literature can be explained as follows [34]. Two different systems of large (with PL energies < E_g) and small NPs (PL energies >E_g) should be considered in the interpretation as illustrated in **Figure 3.26**. Due to the dielectric mismatch, the confined carriers (top row, i.e small NPs) induce polarization charges on the NPs surface. Depending on the dielectric constant of the environment, two cases can be considered. Firstly, when the NP is embedded in a medium of low dielectric constant the sign of the induced charges is the opposite of that of the source charges ($\varepsilon_{NP}<\varepsilon_{media}$). This means that the self-interaction between the source and induced charges is slightly attractive and the dielectric charge confinement is high. Conversely, the electron–hole Coulomb polarization interaction is less repulsive and exciton binding energy is higher. Secondly, when the NP is embedded in a medium of high dielectric constant the self-interaction between the source and induced charges is highly attractive and the dielectric charge confinement is low. Conversely, the electron–hole Coulomb polarization interaction is more repulsive and exciton binding energy is lower. While these two contributions tend to compensate (probable reason of PL independence on dielectric constant in [26] and **Figure 3.25a**), sometimes the cancelation is not exact. Depending on the system under investigation,

with increasing dielectric constant of the environment the self-interaction (possibly as in [27]) or electron-hole polarization interaction term prevails, leading to red-shift (as illustrated in **Figure 3.26**, top row), or blue-shift, respectively. For large NPs (bottom row in **Figure 3.26**), dielectric confinement due to self-interaction is neglectable, and in polar media with lower dielectric constants, the radiative energy states (excitonic and/or impurity-like) distributed over a large energy range inside the band gap ensure wider PL spectra of the NPs (see in **Figure 3.25b** for dichloromethane). As it is illustrated by the scheme in **Figure 3.26** (bottom row, i.e. large NPs), the redistribution of localized energy states induced by highly polar media leads to: (i) the observed narrowing of the whole PL spectrum and, in consequence, to (ii) the apparent blue-shifts of the PL peaks.

3.4.2. Surface charge effect

Qualitative analysis of the negative charges at the NP surface was performed by adding anionic sodium lauryl sulfate (SLS) and cationic cetyltrimethylammonium bromide (CTMA) surfactants to the water suspension of SiC NPs. Schematic representations of the ions formed due to the dissociation of the surfactants in polar solvents are shown in **Figure 3.27a**.

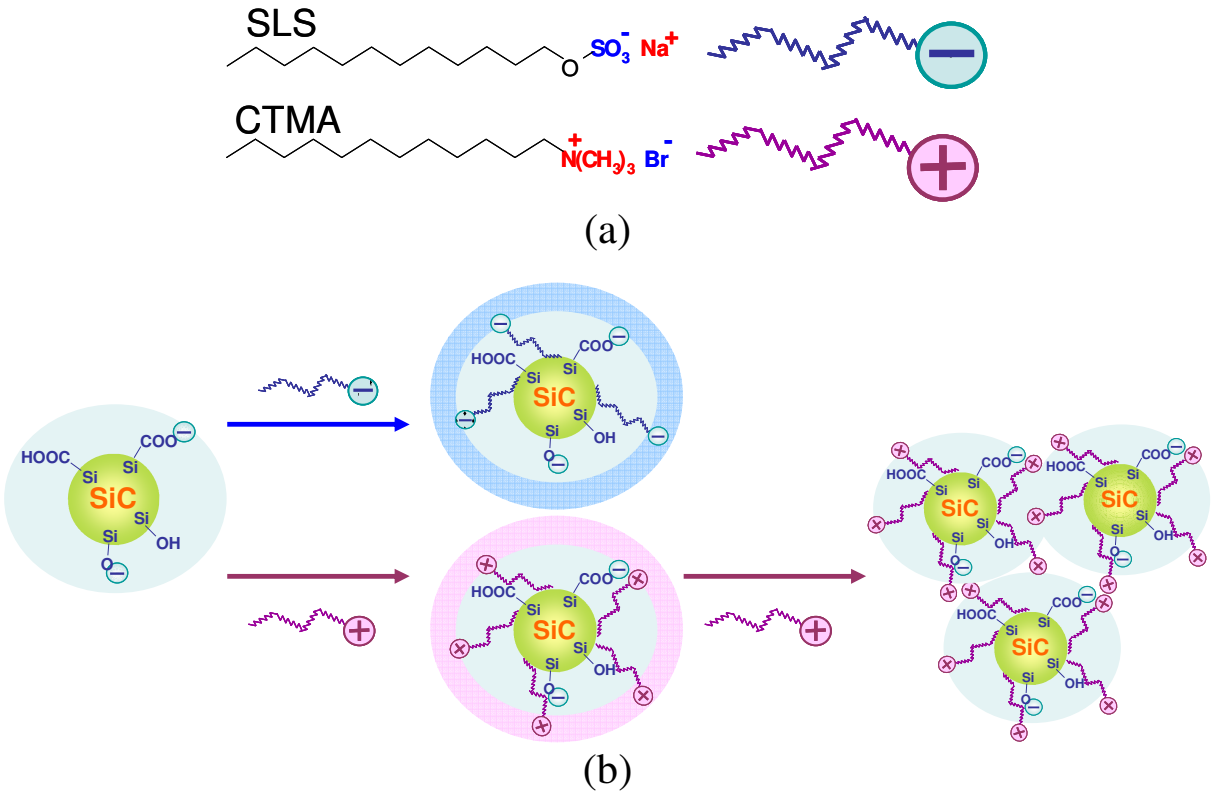

***Figure 3.27**: Schematic representation (a) of the cationic and anionic surfactants, (b) possible interaction between the surfactants and SiC NPs.*

Figure 3.27b illustrates possible ways of interaction between the charged surfactants and NPs. Adsorption of the SLS molecules on the NP surface takes place due to poor solvation of the surfactant hydrophobic tails by polar solvents and results in increase in overall negative charge of the NPs. Adsorption of the CTMA takes place mainly due to the electrostatic interaction, which results in the compensation of the negative surface charge of the NPs. Charge compensation, as well as hydrophobic interaction, between alkyl tails of adsorbed CTMA molecules favours the NP agglomeration and coagulation.

This interaction analysis is very well accorded with images given in **Figure 3.28** presenting different NPs suspensions without and just after adding surfactants. The NPs concentrations in all suspensions were kept the same. The colloidal suspension containing SLS molecules is optically denser than the suspension without this surfactant. For the suspension with the CTMA molecules, aggregation of a lot of NP can be clearly seen. Further, suspensions were ultra-sonicated to destroy created agglomerates. Quantitative study giving information on the NP surface charges was performed by measurements of Z-potential. First of all, the measured negative value of the Z-potential (-29.8 mV) of NPs in the suspensions without surfactants is in perfect agreement with the TPD-MS and FTIR measurements presented in part 3.2. Adding anionic SLS surfactant leads to a slight increase in the initial negative Z-potential value up to -34 mV. This reflects the enhancement of the negative charges on the NP surface. The Z-potential of the suspensions with CTMA surfactant presenting strong coagulation of the NPs was found to be positive (+48.3 mV).

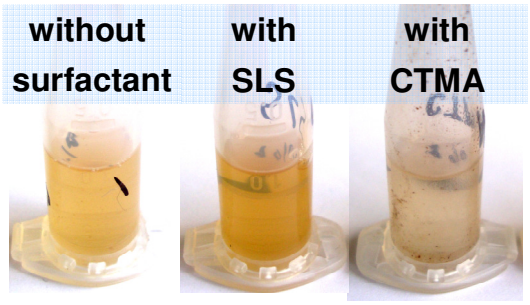

***Figure 3.28**: General views of the solutions containing SiC NPs and surfactants (constant concentration).*

The impact of surface charges on absorption and PL of the SiC NPs in aqueous solutions is reported in **Figure 3.29**. First, one can remark that the absorption and PL spectra of the NPs in water differ considerably from the corresponding spectra obtained in water+CTMA suspensions. This difference is especially pronounced for the spectral range >450 nm. In particular, the absorption and PL signals were found to be systematically higher in the water+CTMA suspensions. A redshift (about 25 nm) of the PL peak position corresponding to the NPs dispersed in water+CTMA suspensions can also be observed.

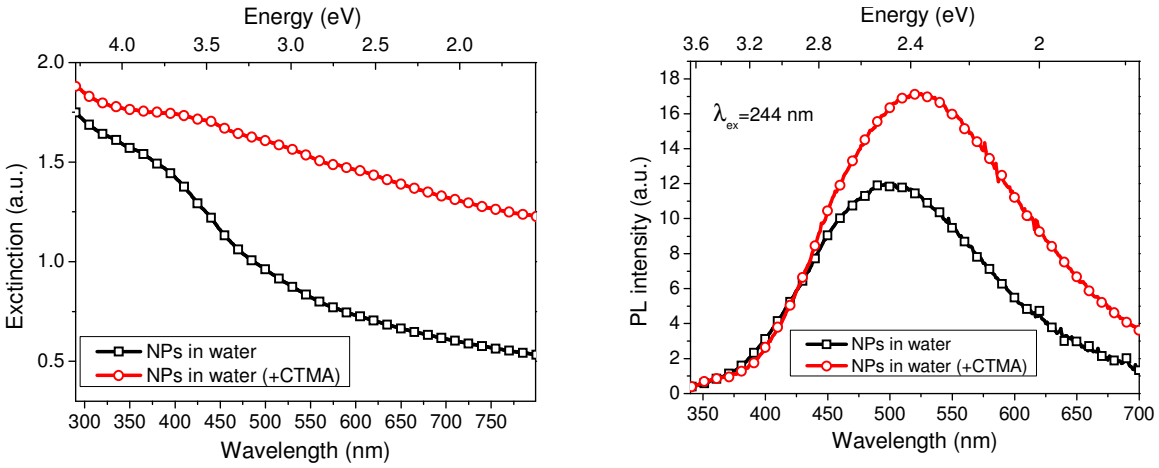

***Figure 3.29**: (a) Extinction and (b) PL spectra of aqueous suspensions containing SiC NPs with and without surfactant.*

To clarify the impact of the electrical charges, more detailed variation of surface charge was performed. Toward this end, small amounts of CTMA surfactant were added to the suspension. Surface charges of the NPs were controlled by zeta-potential measurements. Increasing dependence of zeta-potential versus amount of the added surfactant can be seen in **Figure 3.30**. It is worth noting that zeta-potential does not exactly corresponds to the intensity of local fields inside NPs. Measured value is influenced by counter-ions which cover charged particle. In that way, samples with the zero internal fields may not necessarily be characterized by zero zeta-potential.

Furthermore, level of optical absorption at excitation (λ=244 nm) and below band-gap region (λ=562 nm) was recorded as illustrated in **Figure 3.31.** In the case of close to zero zeta-potential, the colloidal suspensions became unstable and no reliable optical measurements can be carried out because of a strong light scattering. Nevertheless, two main tendencies can be seen. Firstly, with increasing amount of surfactant added to the suspension (decreasing of negative charge) below bandgap absorption is enhanced, as observed in **Figure 3.29a**. As in case of different dielectric environments, it can be caused by increased density of states in corresponding energy region. Secondly, by decreasing value of zeta-potential (internal field) of NPs, absorption band at

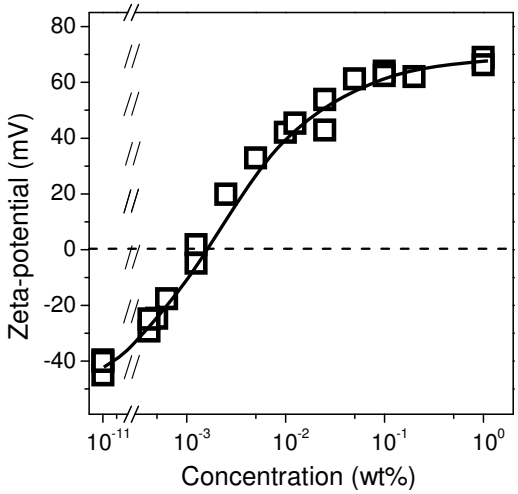

***Figure 3.30**: Dependence of zeta-potential on surfactant concentration (solid line for eye guidance).*

short wavelengths region (λ=244 nm) also decrease.

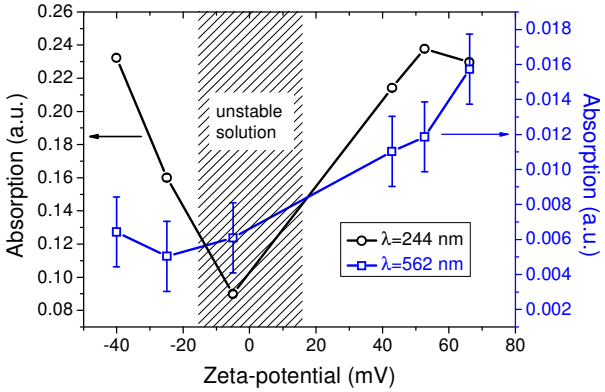

***Figure 3.31**: Long (λ=562 nm) and short (λ =244 nm) wavelength optical absorption as a function of zeta-potential.*

PL spectra of several samples with corresponding zeta-potential are shown in **Figure 3.32a**. PL intensity with increasing amount of added surfactant tends to decrease and after some threshold at ζ =+53 mV is almost restored to its previous magnitude. Similar tendency can be found for spectral changes, where maximum red-shift is reached at around the same zeta-potential value (ζ =50-60 mV). Normalized PL spectra of two extreme samples are shown in **Figure 3.32b**. Sample with high electric fields for negative charges (ζ=-39 mV) is marked as S1. Sample S2 corresponds to the suspension with the lowest PL intensity (ζ=+50 mV). Contrary to the spectrum of the sample S1, S2 has two remarkable spectral features: below and above band gap value (2.3 eV) of bulk 3C-SiC substrate. Spectrum of dry SiC nanopowder is also shown for additional comparison. Dry nanopowder is constituted only by neutral NPs with zero fields, since there is almost no dissociation of surface chemical groups in air. One can easily state that the spectra S1 and of dry nanopowder reflect high and low energy features of the spectrum S2, respectively.

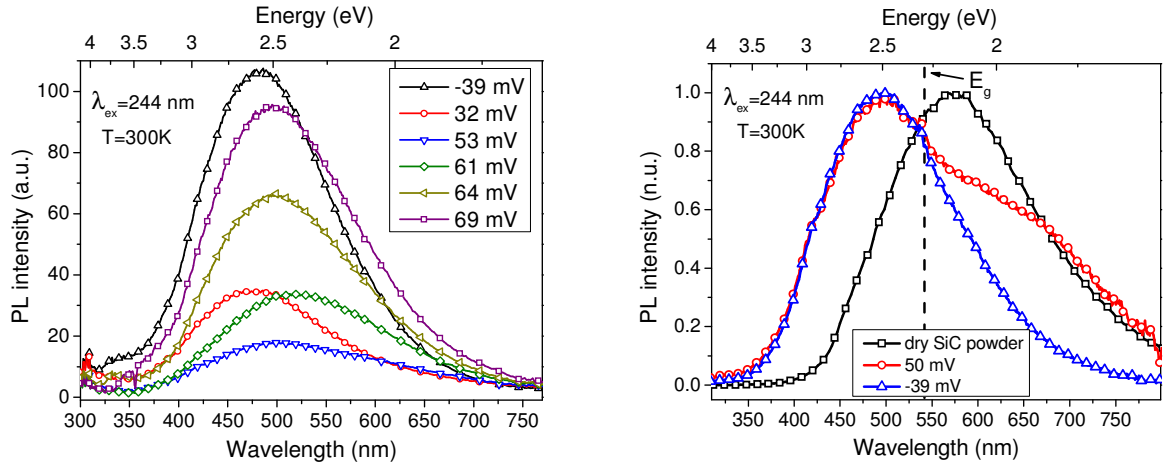

***Figure 3.32**: (a) Variation of PL spectra for a few zeta-potential values, and (b) normalized PL spectra of suspensions with high electric field strengths (ζ=-39 mV), with lowest PL intensity (ζ=50 mV) and spectrum of dry SiC powder.*

As it was discussed before, origin of low-energy feature is related to the localized energy states, especially in the largest particles, when the charge transfer from the smallest ones may occur. On the other hand, high-energy PL is believed to be related to band-to-band transitions of quantumly confined charge carriers in very small NPs. Moreover, influence of surface charges onto particles with various sizes should be different. Possible interactions of electrons and holes with external fields induced by surface charges are summarized in **Figure 3.33**. Influence of high local fields caused by negative (E^-) and positive (E^+) charges are represented in first and third column, respectively. For large NPs (bottom row) with zero external field (second column), localized energy states play dominant role. Sequent adding of the positive surfactant to the initially negative SiC NPs increase density of states in this energy region which correlates well with absorption rise in **Figure 3.29a** and **3.31.** This reflects slightly in redshifted PL in **Figure 3.29b** and **3.32,** however most of the spectral changes are emphasized when low energy component becomes visible due to quenching of high energy peak.

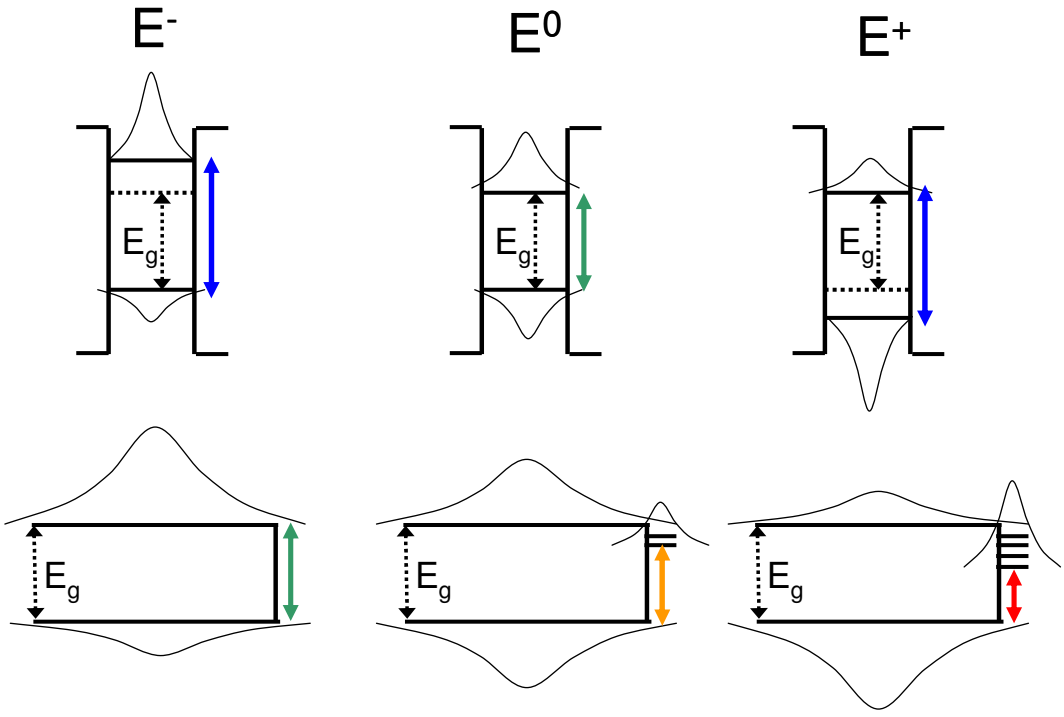

***Figure 3.33**: Schematic representation of the influence of negative (first column), positive (third column) surface charges in comparison with zero (second column) charges in small (top row) and large (bottom row) NPs. Illustrative electron/hole wavefunctions are represented by thin solid lines. The arrows indicate possible channels for the electronic transitions.*

PL dependence related to radiative recombination in small NPs on applied external field is illustrated in **Figure 3.33** (top row). For the initially dissolved SiC NPs (ζ=-39 mV),

negative surface charges increase localization of electron inside NP (first column), in comparison with neutral NP (second column). On the other hand, holes become more attracted to the surface leading to delocalization. Opposite localization of electrons closer to surface and holes inside NP is anticipated for positive surface charges. It should be emphasized that electron-hole wave-functions and delocalization in **Figure 3.33** are for illustration only. Exact localization may lead to more complex dependencies of PL intensity on applied external field. In current studies, larger surface charge (positive or negative) results in the increased electron-hole wave-function overlap and thus higher PL intensity. Additionally, due to field-induced localization of charge carriers, one could expect energy changes in the electronic transitions. Magnitude of the corresponding spectral shift (example of blue-shift in **Figure 3.33**, top row) is governed by the difference in effective masses of electrons and holes. However, the system of highly polysized SiC NPs with wide distribution of discrete energy levels prevents from detection of reasonable Stark shift.

Finally, in order to estimate emission efficiency as a function of zeta-potential (**Figure 3.34**), absorption level at excitation wavelength (λ=244 nm) in **Figure 3.31** and PL signal in **Figure 3.32a** were taken into account. One can remark constant efficiency in negative zeta-potential region. Secondly, about 5-fold efficiency modulation can be observed at around ζ=+50 mV. This region corresponds to NPs with zero-external field. As mentioned before, shifted value is a result of counter-ions near NPs.

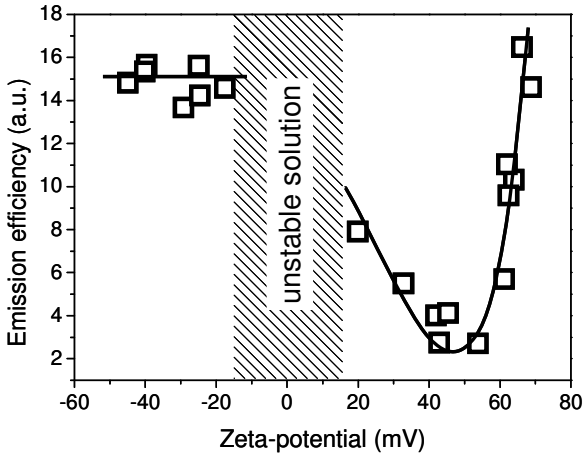

***Figure 3.34**: Dependence of emission efficiency on zeta-potential (solid line for eye guidance).*

3.5. Conclusions

In the course of this chapter, main physico-chemical properties of SiC nanostructures obtained by electrochemical anodization and laser ablation methods were discussed. Both fabrication procedures allow formation of NPs with size sufficiently small to observe quantum-confinement effects. Additionally, described surface chemistry of the NPs can ensure, in future, their chemical functionalization for various multidisciplinary applications. Size dependence of complex optical response from the elaborated nanostructures was verified after filtration and centrifugation techniques. It was also confirmed by structural and elemental analysis that electrochemical etching method allows supplementary creation of large amount of carbon-based nanostructures. These objects were reported in literature to be also optically active in UV-Visible region. Moreover, near-field interaction between carbon and SiC nanostructures were evidenced from PL and optical absorption studies. For example, oxidation-induced carbon removal allows visualization of the transitions between energy levels in the SiC NPs in which photo-generated charge carriers are quantumly confined.

The most importantly, the chemical environment influences strongly the electronic transitions in the carbon-SiC NPs. In particular, the solvent nature and the surface charges of the NPs have to be considered in terms of local field effects to understand the spectral features of the absorption and PL spectra. Observed dependencies were described by electron-hole wavefunction overlapping and redistribution of localized energy states in the band-gap.

3.6. References

1. WU X.L., FAN J.Y., QIU T., et al. Experimental Evidence for the Quantum Confinement Effect in 3C-SiC Nanocrystallites. Physical Review Letters, 2005, vol. 94, no. 026102.
2. ZEKENTES K., ROGDAKIS K. SiC nanowires: material and devices. Journal of Physics D: Applied Physics, 2011, vol. 44, no. 133001.
3. ALEKSEEV S.A., ZAITSEV V.N., BOTSOA J., et al. Fourier Transform Infrared Spectroscopy and Temperature-Programmed Desorption Mass Spectrometry Study of Surface Chemistry of Porous 6H-SiC. Chemistry of Materials, 2007, vol. 19, p.2189–2194.
4. SHIN W., SEO W., TAKAI O., et al. Surface chemistry of porous silicon carbide. Journal of Electronic Materials, 1998, vol. 27, no. 4, p.304–307.
5. SERDIUK T., LYSENKO V., ALEKSEEV S.A., et al. Size tuning of luminescent silicon nanoparticles with meso-porous silicon membranes. Journal of Colloid and Interface Science, 2011, vol. 364, p.65–70.
6. WU X.L., XIONG S.J., ZHU J., et al. Identification of surface structures on 3C-SiC nanocrystals with hydrogen and hydroxyl bonding by photoluminescence. Nano Letters, 2009, vol. 9, no. 12, p.4053–4060.
7. ZHENG Y., LALANDER C.H., BACH U. Nanoscale force induced size-selective separation and self-assembly of metal nanoparticles: sharp colloidal stability thresholds and hcp ordering. Chemical Communications, 2010, vol. 46, p.7963–7965.
8. SUBRAMONEY S. Novel Nanocarbons—Structure, Properties, and Potential Applications. Advanced Materials, 1998, vol. 10, no. 15, p.1157–1171.
9. LU J., YANG J., WANG J., et al. One-pot synthesis of fluorescent carbon nanoribbons, nanoparticles, and graphene by the exfoliation of graphite in ionic liquids. ACS Nano, 2009, vol. 3, no. 8, p.2367–2375.
10. FANG Y., GUO S., LI D., et al. Easy synthesis and imaging applications of cross-linked green fluorescent hollow carbon nanoparticles. ACS Nano, 2012, vol. 6, no. 1, p.400–409.
11. PASTERNACK R.F., COLLINGS P.J. Resonance light scattering: a new technique for studying chromophore aggregation. Science, 1995, vol. 269, p.935–939.
12. EDA G., LIN Y.-Y., MATTEVI C., et al. Blue photoluminescence from chemically derived graphene oxide. Advanced Materials, 2010, vol. 21, p.1–5.

13. ZHAO Q.-L., ZHANG Z.-L., HUANG B.-H., et al. Facile preparation of low cytotoxicity fluorescent carbon nanocrystals by electrooxidation of graphite. Chemical Communications, 2008, vol. 41, p.5116–5118.
14. SUN Y.-P., ZHOU B., LIN Y., et al. Quantum-sized carbon dots for bright and colorful photoluminescence. Journal of the American Chemical Society, 2006, vol. 128, no. 24, p.7756–7757.
15. BOURLINOS A.B., STASSINOPOULOS A., ANGLOS D., et al. Surface functionalized carbogenic quantum dots. Small, 2008, vol. 4, no. 4, p.455–8.
16. KUBIN R.F., FLETCHER A.N. Fluorescence quantum yield of some rhodamine dyes. Journal of Luminescence, 1982, vol. 27, p.455–462.
17. FAN J., LI H., JIANG J., et al. 3C-SiC nanocrystals as fluorescent biological labels. Small, 2008, vol. 4, no. 8, p.1058–1062.
18. SHIM H.W., KIM K.C., SEO Y.H., et al. Anomalous photoluminescence from 3C-SiC grown on Si(111) by rapid thermal chemical vapor deposition. Applied Physics Letters, 1997, vol. 70, no. 13, p.1757–1759.
19. BOTSOA J., BLUET J.-M., LYSENKO V., et al. Luminescence mechanisms in 6H-SiC nanocrystals. Physical Review B, 2009, vol. 80, no. 155317.
20. DOLGAEV S.I., SIMAKIN A.V., VORONOV V.V., et al. Nanoparticles produced by laser ablation of solids in liquid environment. Applied Surface Science, 2002, vol. 186, p.546–551.
21. STANCIU C., EHLICH R., PETROV V., et al. Experimental and theoretical study of third-order harmonic generation in carbon nanotubes. Applied Physics Letters, 2002, vol. 81, no. 21, p.4064–4066.
22. DE DOMINICIS L., BOTTI S., ASILYAN L.S., et al. Second- and third-harmonic generation in single-walled carbon nanotubes at nanosecond time scale. Applied Physics Letters, 2004, vol. 85, no. 8, p.1418–1420.
23. GUPTA A.K., ALON O.E., MOISEYEV N. Generation and control of high-order harmonics by the interaction of an infrared laser with a thin graphite layer. Physical Review B, 2003, vol. 68, no. 205101.
24. DEAN J.J., VAN DRIEL H.M. Second harmonic generation from graphene and graphitic films. Applied Physics Letters, 2009, vol. 95, no. 261910.
25. WU S., MAO L., JONES A.M., et al. Quantum-enhanced tunable second-order optical nonlinearity in bilayer graphene. Nano Letters, 2012, vol. 12, p.2032–2036.

26. FAN J.Y., WU X.L., LI H.X., et al. Luminescence from colloidal 3C-SiC nanocrystals in different solvents. Applied Physics Letters, 2006, vol. 88, no. 041909.
27. BEKE D., SZEKRÉNYES Z., BALOGH I., et al. Characterization of luminescent silicon carbide nanocrystals prepared by reactive bonding and subsequent wet chemical etching. Applied Physics Letters, 2011, vol. 99, no. 213108.
28. YANG S., CAI W., ZENG H., et al. Ultra-fine β-SiC quantum dots fabricated by laser ablation in reactive liquid at room temperature and their violet emission. Journal of Materials Chemistry, 2009, vol. 19, no. 38, p.7119–7123.
29. GUPTA B.K., GROVER V., GUPTA G., et al. Highly efficient luminescence from hybrid structures of ZnO/multi-walled carbon nanotubes for high performance display applications. Nanotechnology, 2010, vol. 21, no. 475701.
30. KŮSOVÁ K., CIBULKA O., DOHNALOVÁ K., et al. Brightly luminescent organically capped silicon nanocrystals fabricated at room temperature and atmospheric pressure. ACS Nano, 2010, vol. 4, no. 8, p.4495–4504.
31. CHAZALVIEL J.-N., OZANAM F., DUBIN V.M. Role od dielectric effects in the red-green switching of porous silicon luminescence. Journal De Physique I, 1994, vol. 4, no. 9, p.1325–1339.
32. LOPEZ H.A., CHEN X.L., JENEKHE S.A., et al. Tunability of the photoluminescence in porous silicon due to different polymer dielectric environments. Journal of Luminescence, 1998, vol. 80, p.115–118.
33. TIMOSHENKO V.Y., DITTRICH T., LYSENKO V., et al. Free charge carriers in mesoporous silicon. Physical Review B, 2001, vol. 64, no. 085314.
34. ROYO M., CLIMENTE J.I., MOVILLA J.L., et al. Dielectric confinement of excitons in type-I and type-II semiconductor nanorods. Journal of Physics: Condensed Matter, 2011, vol. 23, no. 015301.

Chapter 4

Plasmon-Enhanced Optical Properties of SiC Nanostructures

Recent progress in fabrication techniques of plasmon nanostructures has already boosted the rapid growth of plasmon enhanced fluorescence [1-5], high harmonic generation [6-9] and photovoltaic [10] research. Special interest has been devoted to the implementation of plasmonics in biology and medicine [11-13].

Original optical properties of SiC nanostructures allowed their various promising applications as light-emitting agents [14-17]. Unfortunately, despite their higher emission efficiency in comparison with bulk SiC materials, the overall brightness of SiC NPs is still very low compared to those of dyes and direct band gap emitters.

At the same time, SiC is known to have extremely interesting non-linear optical (NLO) properties [18-23]. Furthermore, the initial NLO properties of SiC nanostructures can be significantly enriched due to defects, crystalline symmetry and shape distortions as well as due to any broken symmetry at interfaces [24-28]. However, in comparison with commonly used non-linear crystals, the reported NLO characteristics of SiC nanostructures have to be enhanced.

This chapter focuses on the plasmon enhancement of both linear and nonlinear optical properties of SiC nanostructures obtained by electrochemical etching. Initially, the physics of localized surface plasmon in metallic NPs will be described. Further, the theory of plasmonic field enhancement will be linked with the observed experimental results.

4.1. Localized surface plasmons: general overview

Incident light can interact strongly with metal NPs by inducing coherent oscillations of free electrons, i.e. plasmons. On resonance, the strong polarizability of NP effectively converts the energy of incident electromagnetic wave into the particle. As the result, field is concentrated in the nanoscale volume both inside and outside (in near-field) the particle. Plasmon-enhanced optical properties are attributed to this enhanced local field.

At the beginning of this section, localized surface plasmons will be considered for the small metallic NPs interacting with electromagnetic wave. The discussion will be based on quasistatic approximation, where the electric field is assumed to be practically constant over the volume. Further, additional consideration will be given for analysis of optical response in large NPs. Finally, more complex structures like near-field interacting particles yielding multi-featured resonance spectra will be discussed.

The three-dimensional electromagnetic simulations were used to solve Maxwell's equations by finite-difference time-domain (FDTD) method (Lumerical Solutions Inc., http://www.lumerical.com). In such a way far-field absorption and scattering spectra as well as near-field intensity enhancement were easily calculated. Dielectric data for bulk silver were taken from Palik [29] and parametrized using software in the corresponding spectral range.

4.1.1. Local plasmons in small particles

The plasmon resonance for a small spherical particle of radius **r** can be analyzed in the electrostatic limit where $\mathbf{d} \ll \boldsymbol{\lambda}$, i.e. particles is much smaller than the wavelength of incident light. In a dielectric environment with dielectric constant $\boldsymbol{\varepsilon_m}$, the applied electric field $\mathbf{E_0}$ induces polarizability $\boldsymbol{\alpha}$, defined via polarization **p**:

$$\mathbf{p} = 4\pi\varepsilon_0\varepsilon_m\alpha\mathbf{E_0} \tag{4.1}$$

The dependence of polarizibility on the dielectric response of the sphere described by complex dielectric function $\boldsymbol{\varepsilon}(\omega)$ is given by [30]:

$$\alpha = 4\pi r^3 \frac{\varepsilon(\omega) - \varepsilon_m}{\varepsilon(\omega) + 2\varepsilon_m} \tag{4.2}$$

In general, dielectric function $\varepsilon(\omega) = \varepsilon_1(\omega) + i\varepsilon_2(\omega)$ is mutually linked to the complex refractive index $\tilde{n}(\omega) = n(\omega) + ik(\omega)$, defined as $\tilde{n} = \sqrt{\varepsilon}$ and yielding:

$$\varepsilon_1 = n^2 - k^2 \tag{4.3a}$$

$$\varepsilon_2 = 2nk \tag{4.3b}$$

$$n^2 = \frac{\varepsilon_1}{2} + \frac{1}{2}\sqrt{\varepsilon_1^2 + \varepsilon_2^2} \tag{4.3c}$$

$$k = \frac{\varepsilon_2}{2n} \tag{4.3d}$$

,where k is called the extinction coefficient.

As one can see from (4.2), the polarizability is resonantly amplified under Frohlich condition, where $|\boldsymbol{\varepsilon}+2\boldsymbol{\varepsilon}_m|$ is a minimum. The resonance condition simplifies to:

$$\mathrm{Re}[\varepsilon(\omega)] = -2\varepsilon_m \tag{4.4}$$

This relationship expresses the strong dependence of the resonance frequency on the dielectric environment and dielectric function of metal itself. For the metal particle characterized by a free-electron gas (Drude model) resonance red-shifts as $\boldsymbol{\varepsilon}_m$ (or **n)** is increased [31]. This red-shift can be significant in visible spectral range as illustrated in **Figure 4.1a**. Here, extinction spectra of D=40 nm silver particle is plotted as a function of refractive index of the surrounding environment. At the resonance wavelengths extinction efficiency is enhanced, but still limited by incomplete vanishing of denominator in (4.2). Moreover, $\mathrm{Im}[\varepsilon(\omega)] \neq 0$ also rise at longer wavelength, as reflected by increased extinction (absorption) for higher refractive index. This in turn leads to higher concentration of electromagnetic energy into localized fields around particle as plotted in **Figure 4.1b-d**. Field distributions are represented for corresponding resonance wavelengths.

The absorption and scattering cross sections (C_{abs}, C_{sca}) can be given analytically [30]:

$$C_{abs} = k\,\mathrm{Im}[\alpha] = 4\pi k r^3\,\mathrm{Im}\left[\frac{\varepsilon - \varepsilon_m}{\varepsilon + 2\varepsilon_m}\right] \tag{4.5a}$$

$$C_{sca} = \frac{k^4}{6\pi}|\alpha|^2 = \frac{8\pi}{3}k^4 r^6\left|\frac{\varepsilon - \varepsilon_m}{\varepsilon + 2\varepsilon_m}\right|^2 \tag{4.5b}$$

, with *k* being the wavevector in the surrounding medium. It turns out that absorption efficiency scales with r^3 whereas scattering scales with r^6. Consequently, for large particles, extinction is dominated by scattering whereas for small particles it is associated with absorption.

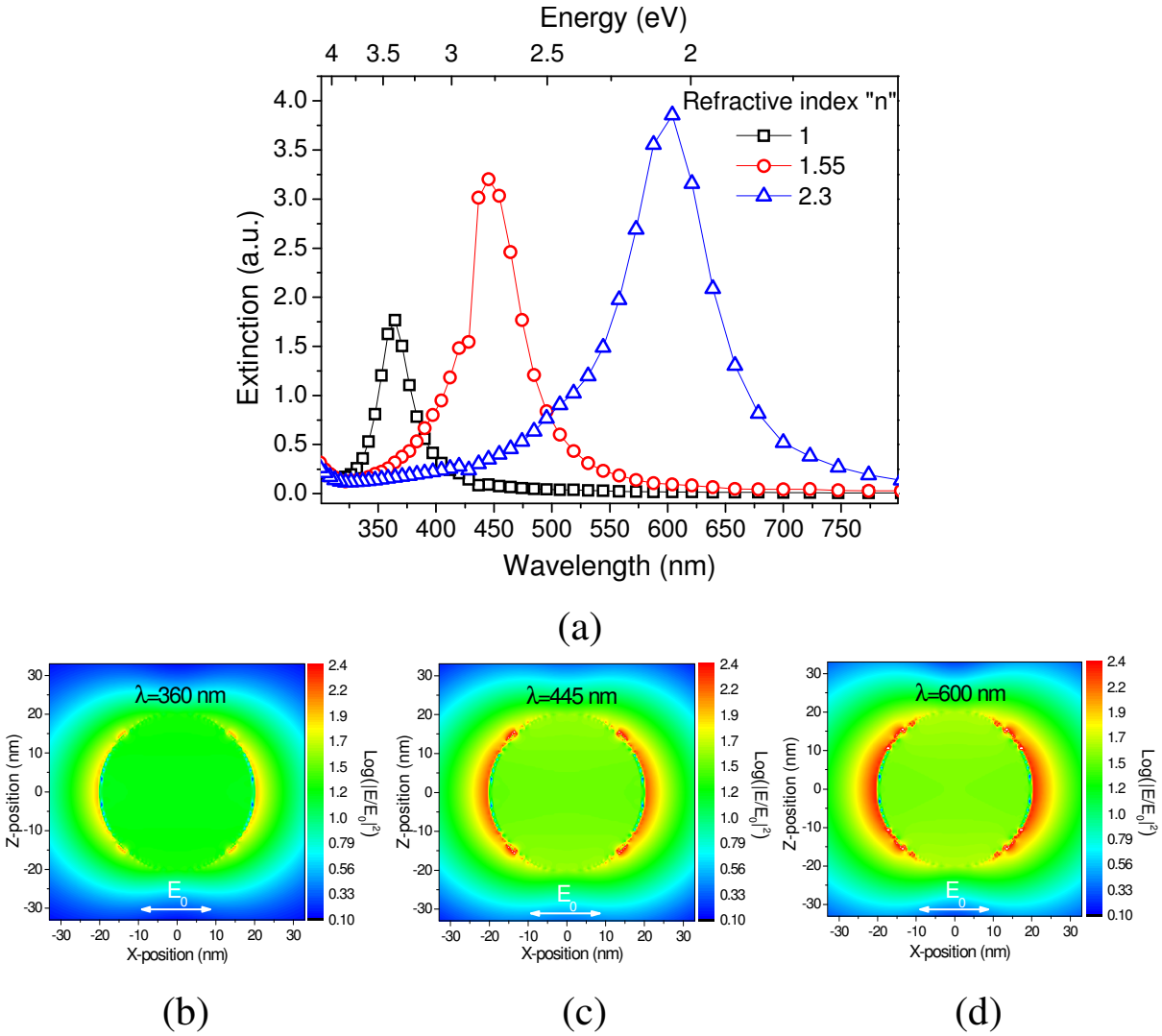

***Figure 4.1**: FDTD calculated (a) extinction spectra of Ag NP with size D=40 nm for three different surrounding environments with corresponding spatial distribution of the field enhancements at maxima of each extinction spectrum: (b) refractive index n=1 (black squares); (c) n=1.55 (red circles) and (d) n=2.3 (blue triangles).*

4.1.2. Local plasmons in large particles

For larger particles, the spectral response is modified due to retardation effects and the excitation of higher-order (quadrupole and higher) modes. In the first case, redshift of dipole plasmon mode is observed with increased size since conduction electrons do not all move in phase anymore, leading to reduction of the depolarization field [31].

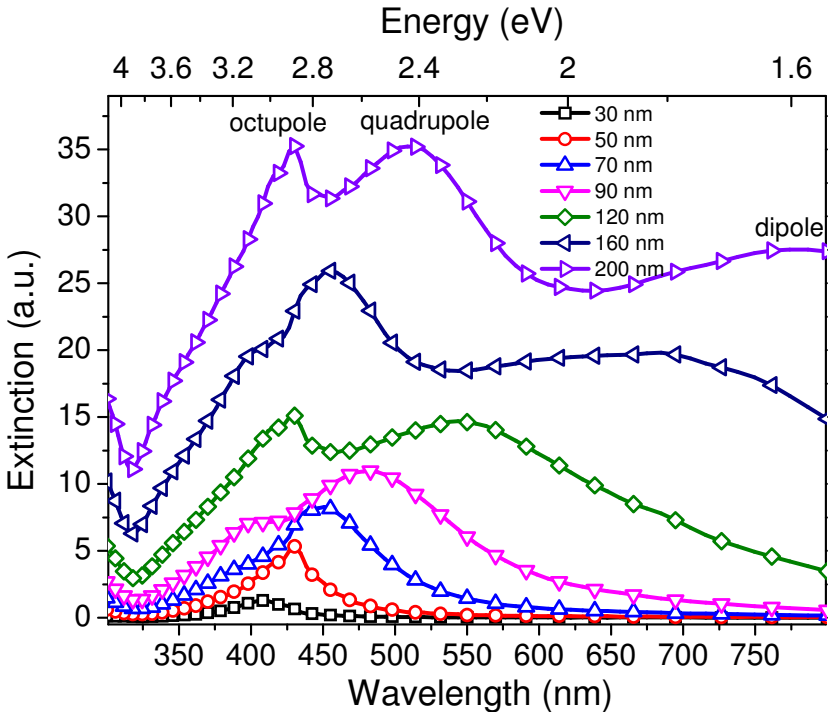

***Figure 4.2**: Calculated extinction spectra of different sized Ag NPs surrounded by water (n=1.33).*

FDTD calculations have been used to investigate the role of silver NP's size embedded in water (n=1.33) on the resonance frequencies. Extinction spectra for particles in 30 to 200 nm size range are plotted in **Figure 4.2**. Fort he smallest particles, the spectrum reveals the presence of a dipole plasmon resonance at 420 nm. As the particle size increases, the dipole resonance progressively red shifts. For 90 nm Ag NPs, the dipole resonance is located at 490 nm, and a new band corresponding to the quadrupole mode appears in the spectrum at 400 nm. When the size of the particles is around 160 nm, the dipole and quadrupole resonances shift to 660 and 460 nm, respectively, and a new band corresponding to the octupole mode emerges in the spectrum at 400 nm. Further, this band gradually evolves into a distinct peak that also shifts to the red spectral range with the increase of the particle size (200 nm). The observation of these modes perfectly correlated with those reported for chemically synthesized Ag NPs [32].

4.1.3. Near-field coupling between particles

As it was shown, the localized plasmon resonance of single metallic particle can be varied in frequency by altering particle size and dielectric environment. Additional shifts are expected in NP ensembles where electromagnetic interaction between localized modes takes place. For small particles these interaction are essentially of a dipolar nature. However, when interparticles distance is very small the polarization induced by neighbouring particles can

lead to more complex electron oscillations. Collective plasmon modes in interacting particles are also strongly dependent on the polarization of the incident excitation.

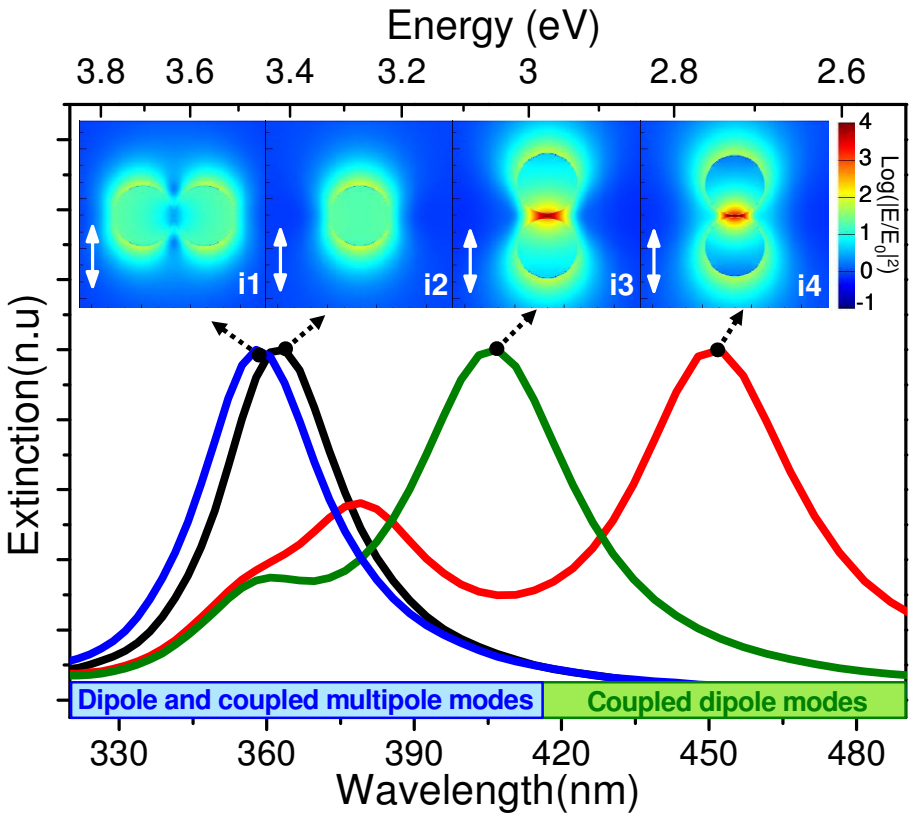

***Figure 4.3**: FDTD calculated extinction spectra of Ag NPs with size D=36 nm for four different configurations: single NP (black curve); NP dimer with surface-to-surface distance s=1nm: transverse excitation (blue curve), longitudinal excitation (red curve); and with surface-to-surface distance s=3 nm, longitudinal orientation (green curve). Insets show spatial distribution of the field enhancements corresponding to maxima of each extinction spectrum.*

As an example, **Figure 4.3** represents calculated extinction spectra and in-plane distribution of the electric field enhancement factors (see insets) for four different configurations: i) single 36 nm Ag NP (black curve; inset i2); Ag NP dimer with inter-particle (surface-to-surface) distance s=1 nm for both ii) longitudinal (red curve; inset i4); and iii) transverse (blue curve; inset i1) polarizations; iv) NP dimer with inter-particle distance s=3 nm for longitudinal light polarization (green curve; inset i3). Each in-plain mapping picture of the electric field enhancement was obtained for the wavelength of the corresponding extinction maximum. The observed strong electric field localization between the NPs for the cases i3 and i4 is due to suppression of scattering into the far-field via excitation of plasmon modes in particles along the chain axis, mediated by near-field coupling [30]. Depending on the exciting light polarization direction, this leads to a blue-shift of the plasmon resonance for

the transverse light polarization, and to a red-shift for the longitudinal one, as it can been seen from the extinction spectra in **Figure 4.3**. Additionally in the latter case, the second multipole plasmon band becomes significantly pronounced. It reflects characteristics of the multipole polarization, as reported by the Mie theory. However, it should be noticed that the multipole effect in Mie theory takes place for metallic particles with sizes comparable to the light wavelength. In present case, the NP sizes are much smaller and hence the multipole effect is totally ensured by the induced polarization when the inter-particle distance is relatively small [33]. In the case of NP dimer with the distance s=3 nm, the effect of the near-field coupling is less pronounced since for closely spaced particles with $s<<\lambda$ the near-field interactions scale with distance as s^{-3}. The observed spectral range was thus divided on two regions to emphasize nature of plasmon modes for each Ag NP configuration, i.e. as coupled dipole (red-shifted) and coupled multipole plasmon modes for the dimers with high degree of near-field coupling, whereas the non-interacting particles support dominantly dipole plasmon modes.

It is important to note that classical electrodynamics fails to describe physical phenomena when metal NPs are closer than couple nanometres. In these conditions, additional considerations could be incorporated beyond standard FDTD. For example, in case of NPs dimer with separation smaller than 1 nm (as it was discussed recently [34]), a new plasmon mode is enabled when conductive overlap is established between the nanoparticles. This is the charge transfer plasmon [35] and involves conduction electrons flowing between the two NPs. The corresponding resonant frequency was observed to blue shift when increasing the overlap between the two NPs. The energy and width of the resonance depend sensitively on the touching profile, the aspect ratio of the composite particle and on the electronic structure of the individual NPs. What is more, the investigation of the electromagnetic field enhancements clearly shows that quantum mechanical effects can play a major role in decreasing the field enhancements in almost touching NP dimers when compared to the classical calculations.

Near-field coupling between interacting particles can be even more amplified by incorporating plasmonic structures in the environment with higher dielectric constant. As it was discussed above, it will cause redshift of the plasmon resonance with increased magnitude of the electric field around the particles. Consequently, increased inhomogeneity of the local fields leads to higher coupling even at relatively large interparticle distances. **Figure 4.4** depicts role of the refractive index on the near-field coupling in NP (D=20 nm) dimers with interparticle spacing s=5 nm. As one can see in **Figure 4.4a**, when resonance

wavelength of NP dimmer is compared to the single NP embedded in the same dielectric environment (vertical dashed lines), larger redshift (i.e. higher coupling) is observed for the case of higher refractive index. Interestingly, for the higher refractive index, additional higher plasmon mode is pronounced in the absorption spectrum as well as role of scattering in the optical response is increased. Local field enhancement distribution in **Figure 4.4b-d** confirms dominant field localization in the interparticle spacing for the higher refractive index.

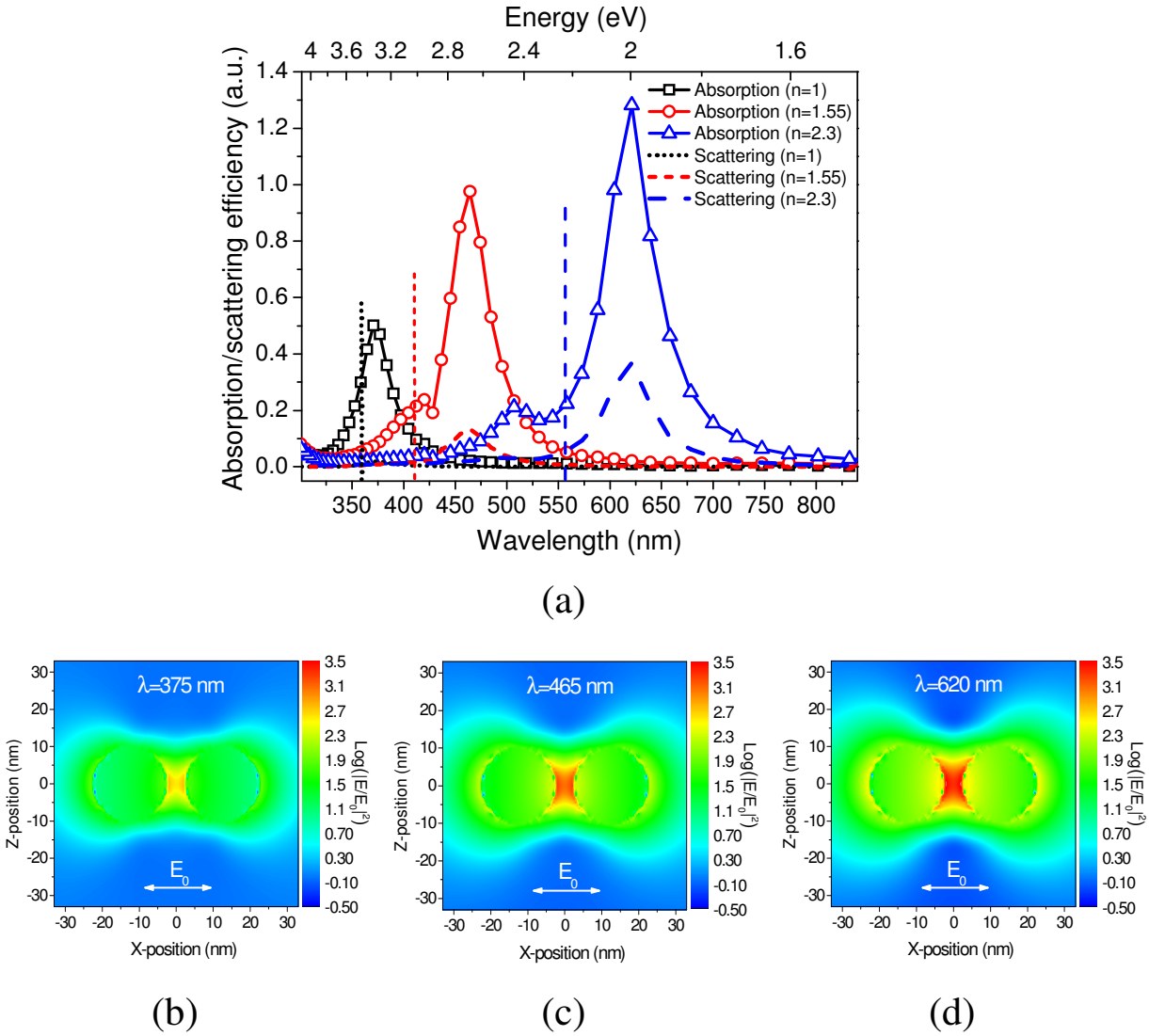

***Figure 4.4**: FDTD calculated (a) absorption/scattering spectra of Ag NPs (D=20 nm) dimer (interparticle spacing s= 5nm) for three different surrounding environments with corresponding spatial distribution of the field enhancements at maxima of each spectrum: (b) refractive index n=1 (black squares/dotted line); (c) n=1.55 (red circles/short dashed line) and (d) n=2.3 (blue triangles/dashed line). Vertical dashed lines represent the maxima of single Ag NPs (D=20 nm) extinction spectra in corresponding environment.*

4.2. Plasmon enhancement of optical properties

4.2.1. Theoretical basis

In general, an optical probe in the near field of an excited metal NP will experience an enhanced local field $E_{loc.}(\lambda) = L(\lambda)E_0(\lambda)$, where $L(\lambda)$ is the wavelength-dependent field enhancement. It was shown in previous section that enhanced electromagnetic fields around NPs $L(\lambda)$ is also a function of material, size and environment as well as the distance between the emitter and the metal surface.

4.2.1.1. Linear optical properties

In plasmon-enhanced fluorescence applications, metallic nanostructures can interact in several ways: by enhancing the optical intensity of incident light through near field enhancement, and by modifying the radiative and non-radiative decay rates of nearby luminescent fluorophores or quantum dots (QDs). In the latter case, both quantum yield (QY) and lifetime are affected. Emission QY is defined as:

QY= (number of emitted photons)/(number of absorbed photons) (4.6)

On the other hand it can be represented as ratio of radiative to total (radiative+nonradiative) decay rates:

$QY= (K_{rad})/(K_{rad}+K_{nonrad})=1/(1+K_{nonrad}/K_{rad})$ (4.7)

Taking into account these relationships, PL intensity or number of emitted photons can be rewritten as:

(number of emitted photons)= (number of absorbed photons)/(1+ K_{nonrad}/K_{rad}) (4.8)

Due to the local-field enhancement, the PL intensity will increase by a factor η_{PL} :

$$\eta_{PL}(\lambda_{ex.},\lambda_{em.}) = \eta_{abs.}(\lambda_{ex.})\eta_{QY}(\lambda_{em.}) \quad (4.9)$$

Here, the first factor reflects increases in PL intensity due to enhanced absorption η_{abs} , at the excitation wavelength λ_{ex}, and the second factor is the enhancement in QY η_{QY} ; this latter term describes the changes in the radiative and non-radiative decay dynamics at the emission wavelength λ_{em}.

In many cases, excitation and emission wavelengths are different, thus spectral overlap control of plasmon resonance of metal nanostructures with the absorption and/or emission bands of the fluorophore might be one of the crucial factors. Furthermore, it has been shown that luminescence quantum efficiency enhancement associated to resonant coupling with plasmon modes is highly dependent on the nanostructure size. An optimal size is the trade-off between i) emitter-plasmon coupling, which is most efficient for small particles, and ii) outcoupling of plasmons into radiation, taking place mainly for large particles [36]. This closely relates to the fact that for small particles with sizes $R<<\lambda$ (where λ is the radiation wavelength), the efficiency of absorption dominates over the scattering [30]. In this way, optimal size of the plasmonic nanostructures reflects the optimal ratio between their absorption and scattering abilities at the emission wavelengths. The importance of spectral overlap between absorption and emission bands of a luminescent agent and a plasmonic nanostructure has been emphasized by several groups [5, 37-40]. Plasmon-enhanced luminescence has been studied on a large variety of nanoscaled materials including colloidal nanohybrids [3, 41], lithography fabricated nanostructures [2] and nanostructured silver films [11, 40].

4.2.1.2. Nonlinear optical properties

Efficiency of most NLO phenomena is known to be greatly increased in presence of metallic nanostructures [6-9, 42]. Very high electric field intensities in close vicinity to the photo-excited nanostructured metals are responsible for strong NLO effects at relatively low pump excitation powers. The observed local field enhancement originates from a combination of: a) the lightning-rod effect; and b) the localized surface plasmon resonances depending on excitation and emission energies [43]. For example, the strong local fields induced by both of these mechanisms can lead to an enhancement factor (η) of SHG which can be represented in the simplest form by the following functional dependence [44]:

$$(\eta_{SHG}) \sim L^2(\lambda) L(\lambda/2), \quad (4.10)$$

, where $L(\lambda)$ and $L(\lambda/2)$ are the local field factors at excitation (λ) and SH ($\lambda/2$) wavelengths, respectively. Taking into account two-photon absorption (TPA) rate proportional to $Im(\chi^{(3)})E^4(\lambda)$, where $\chi^{(3)}$ is the third-order susceptibility and $E(\lambda)$ is the electric field amplitude, an excitation enhancement factor η_{TPA} of two-photon excited photoluminescence (TPPL) can be similarly defined as [45]:

$$(\eta_{TPA}) \sim L^2(\lambda) \quad (4.11)$$

4.2.2. Experimental results

4.2.2.1. Planar plasmonic substrates

In order to achieve a high PL enhancement, an approach based on the two following points was developed: (1) localization of SiC NPs in the vicinity of randomly arranged silver (Ag) NPs chemically formed on silicon nitride (SiN_X)/glass substrates (for details see chapter 2) and (2) careful tuning of the multipolar plasmon bands of the metallic NPs to overlap the excitation and emission spectral bands of SiC NPs. Ag was chosen because, among all other metals, its plasmon resonance in the visible spectral range is most efficient due to low Ohmic losses.

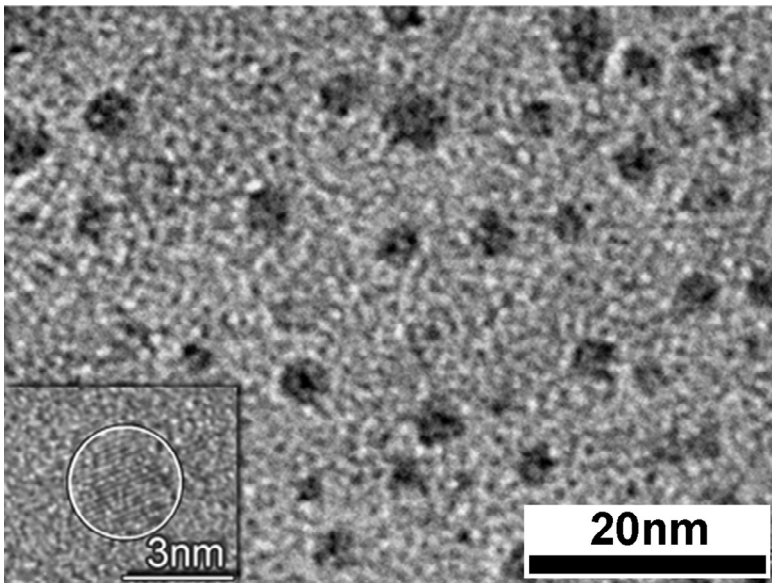

***Figure 4.5**: TEM image of Si NPs inside the SiN_X matrix.*

The TEM picture in **Figure 4.5** shows a typical SiN_X layer with dispersed Si NPs with mean diameters between 2 and 4 nm. Density and size of these NPs, i.e. stoichiometry of the deposited layers can be varied during preparation procedure (variation of NH_3 to SiH_4 ratio (R)). It is worth a remark that SiNx layer with incorporated Si NPs can also manifest in linear and nonlinear optical response as will be discussed later.

Depending on the volume fraction of Si in prepared layers, three possible variations can be observed in evolution of Ag deposition (**Figure 4.6**) [46]:

(i) For samples with large amount of Si atoms (R=0.1) surface density of Si precipitates is high (**Figure 4.6,** first column). Ag NPs are first deposited as nanoscale metallic nuclei on Si nanoclusters present on the surface (top image). Further grow is ensured by preferential deposition of Ag on these nuclei (middle image). Finally, Ag NPs start to coalesce with their neighbours (bottom image).

(ii) For the medium (R=1-3) density of Si precipitates (**Figure 4.6,** second column),

initially embedded into the matrix Si "seeds" progressively appear at surface of SiN_X layer due to chemical dissolution of the superficial layers (top and middle images). With time, new Ag NPs are formed on these growing sites (bottom image).

(iii) Despite chemical dissolution for SiN_X layers with low (R>5) surface density of Si precipitates (**Figure 4.6,** third column) only a small number of new Si seed sites appears with time (top and middle images) due to the low volume fraction of Si nanoclusters. As a result, low surface density and small diameters of Ag NPs can be obtained (bottom image).

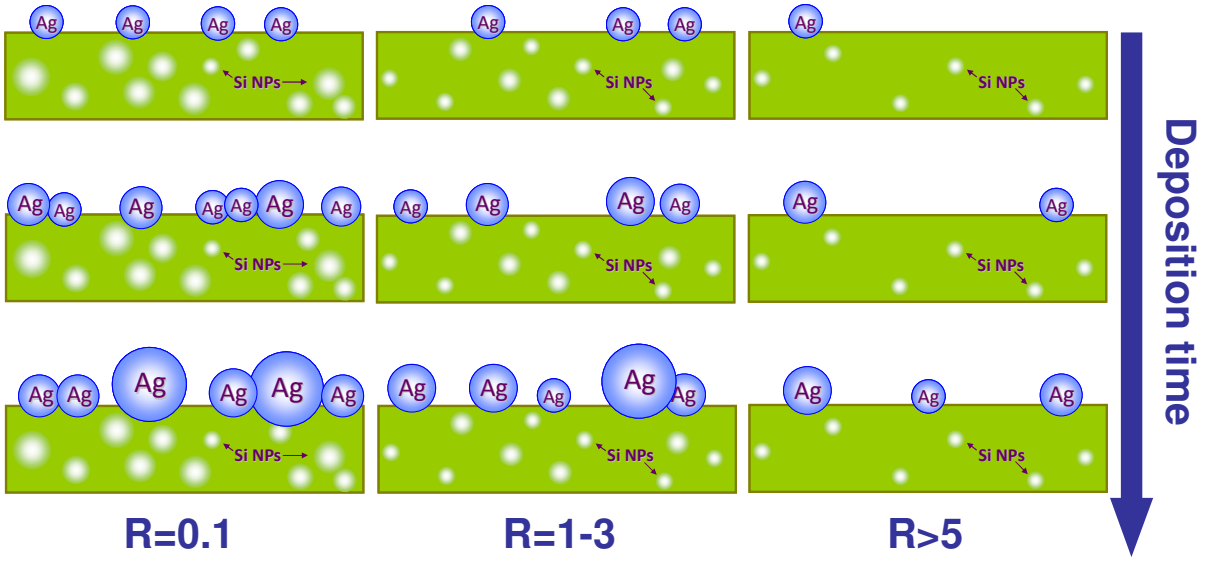

***Figure 4.6**: Schematic views of three possible evolutions of Ag NPs deposition for different stoichiometric ratios (R).*

Topographical AFM views corresponding to the sample with R=5 as a function of Ag deposition time are presented in **Figure 4.7**. As can be seen, both the nanoparticle dimension and surface coverage are strongly dependent on the deposition time. At the beginning, after 1s of deposition (**Figure 4.7a**) several Ag NPs of only few nm in size are formed. Subsequently, when deposition time is increased to 15s, 30s and 1min (**Figure 4.7b-d**), concentration and size of NPs grows. Further, after 2, 3, 4 and 5min (**Figure 4.7e-h**) the formation of Ag nanostructures composed of slightly interconnected NPs, each one of about 30-40 nm in diameter, can be observed. A progressive increase of NPs size from 50 nm to about 100 nm is provided by 10, 15, 20 and 60 min deposition time, correspondingly (**Figure 4.7i-l**).

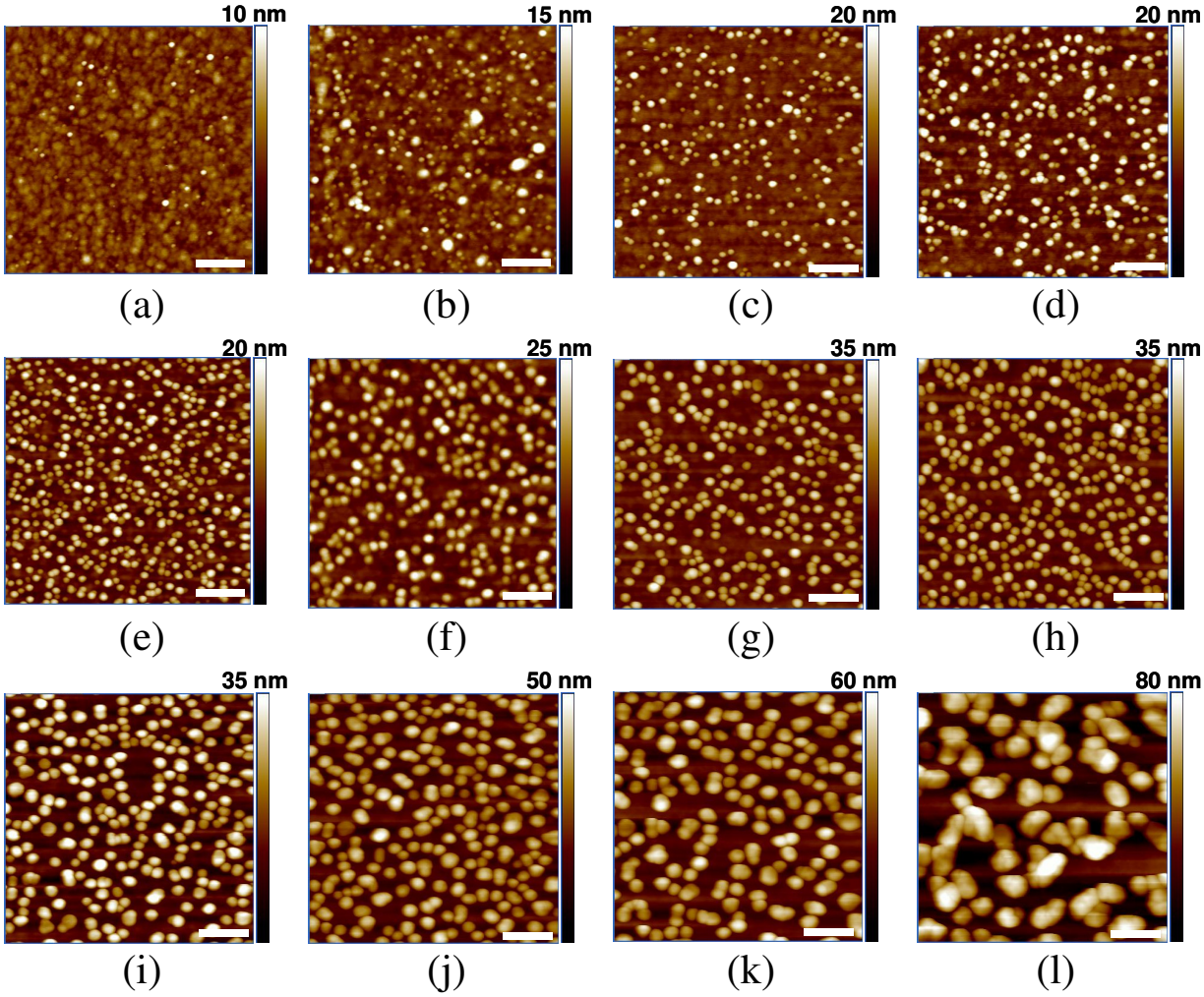

***Figure 4.7**: AFM image of the Ag NPs formed onto the surface of the SiN_X layer after 1s, 15s, 30s, 1min, 2min, 3min, 4min, 5min, 10min, 15min, 20min and 60min deposition time(from (a) to (l)). Scale bar is equal to 200 nm.*

Demonstrated approach of Ag surface coverage allows precise control of substrates plasmonic properties. When only dipolar plasmon modes are needed, one chooses short deposition times and high R, whereas for higher plasmon modes longer deposition times and lower R can be used. Spectral position of the obtained modes and/or level of interparticle coupling can be tuned by the deposition of capping dielectric layer. A cross-section TEM image of the plasmonic structure consisting of nano-Ag/SiNx (sample in **Figure 4.7h**) covered with SiN_Y is presented in **Figure 4.8**. The SiN_X and SiN_Y layers with respective thicknesses of around 150 and 40 nm are clearly visible in the general view of **Figure 4.8a**. The spherical-like Ag NPs are completely embedded into the dielectric SiN matrix and localized at the interface between the SiN_X and SiN_Y layers. The size of the Ag NPs was found from the cross-section TEM image to be about 10-20 nm (**Figure 4.8b**).

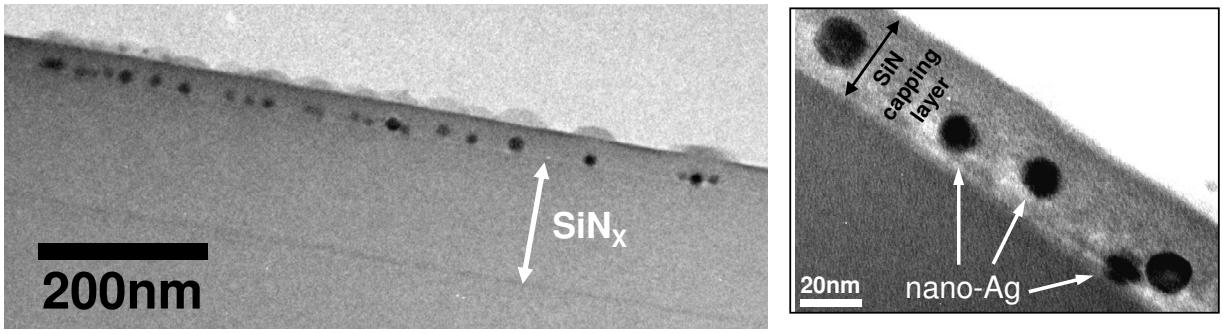

***Figure 4.8**: Cross-section TEM image of the SiN_Y/nano-Ag/SiN_X plasmonic structure in (a) general and (b) magnified view.*

Precise tuning of the local plasmon resonance was carried out by adjusting the SiN_Y dielectric constant (ε_s) which depends on the layer stoichiometry [47]. **Figure 4.9** shows the extinction spectra of the nano-Ag/SiN_X (sample in **Figure 4.7h**) structure covered with SiN_Y as a function of ε_s. For all values, a well defined peak attributed to the local plasmon resonance in Ag nano-islands can be clearly visible. A baseline correction was performed for all samples in order to subtract natural extinction related to the reference SiN_Y/SiN_X sandwich. As one can see, the plasmon resonance wavelength is red-shifted upon increasing the dielectric constant of the surrounding medium, as previously discussed. Thus, a flexible spectral adjustment of the local plasmon resonance in Ag NPs can be easily achieved in the large visible range from 400 to 600 nm.

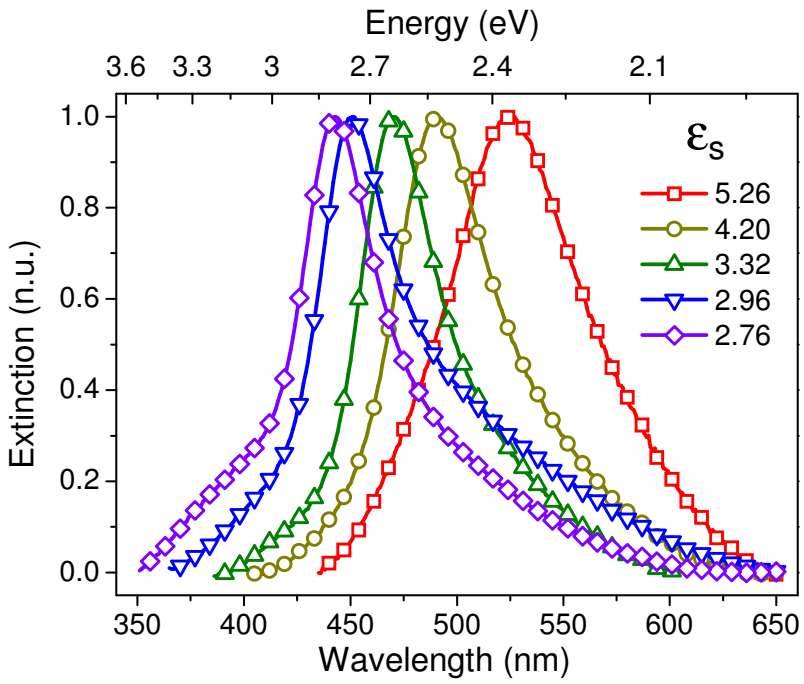

***Figure 4.9**: Extinction spectra of SiN_Y/nano-Ag/SiN_X plasmonic structures as a function of dielectric constant (ε_s) of the superficial SiN_Y layer.*

4.2.2.2. Linear optical properties

In order to realize a resonant coupling between the photoexcited SiC NPs and multi-polar localized plasmons, a sample with R=5 and t=5min Ag deposition time was chosen (**Figure 4.7h**). Localization of the colloidal SiC NPs fabricated by electrochemical etching onto the used nano-Ag/SiNX/glass substrates is performed by a simple drop-and-dry technique (concentration ~0.1 mg/mL). Schematic view of formed samples is illustrated in **Figure 4.10**. Since the mean distance between two adjacent Ag NPs is estimated to be about 20 nm, there is a large number of luminescent SiC NPs with dimensions of 2–5 nm localized between them.

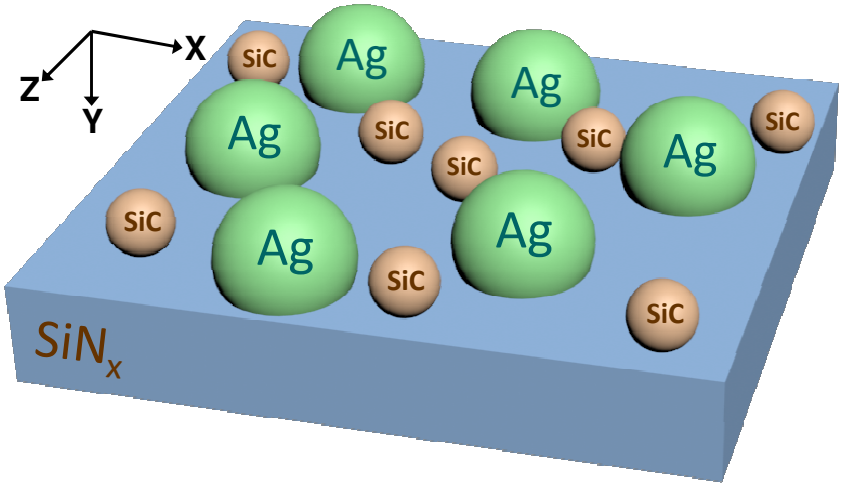

***Figure 4.10**: Schematic representation of the SiC NPs/nano-Ag/SiN$_X$ samples.*

In order to estimate the local excitation field intensity enhancement as well as an effect of near-field plasmon coupling, 3D FDTD simulations were performed. Three-dimensional excitation field enhancement profiles (at wavelength λ= 457 nm) for randomly arranged silver NPs (D=36nm) with the surface coverage calculated on the basis of the AFM picture can be seen in **Figure 4.11**. The centres of seventeen Ag NPs were located in ZX plane for Y = 0 nm. Different configurations of randomly arranged Ag NPs led only to insignificant changes of final results. Since the Ag NPs are slightly immersed into the dielectric SiN_X thin film due to the under-etching of the superficial nanoscale Si sites caused by HF-based solution during the Ag NP formation, their centres were positioned above the dielectric surface at a distance h=6nm. Two spatial regions separated by a black dashed line and referring to air and dielectric layer with respective refractive index n=1 and n=1.72 can be seen on the left picture of **Figure 4.11** corresponding to a ZY plane at X=0. Additionally, four cross-section profiles in ZX plane were calculated for Y = -40, -10, +10, +40 nm (dashed white lines on the left picture of **Figure 4.11**) in order to visualize spatial field enhancement in two opposite

directions from the air-dielectric interface. As one can see, the field enhancement can be observed in both air and SiN_X dielectric regions with the most important part localized in very close vicinity to the neighbouring Ag NPs. In these hot-spot regions, the electric field intensity can easily reach more than 500-fold enhancement leading to drastically enhanced excitation efficiency of luminescent NPs. No field enhancement can be observed at the distances L=40 nm from the NP centre or h=22 nm from the NP surface. This is in good correlation with previous discussion underlining the fact that the SiC NPs should be located within this hot-spot spatial region for maximum excitation/absorption enhancement.

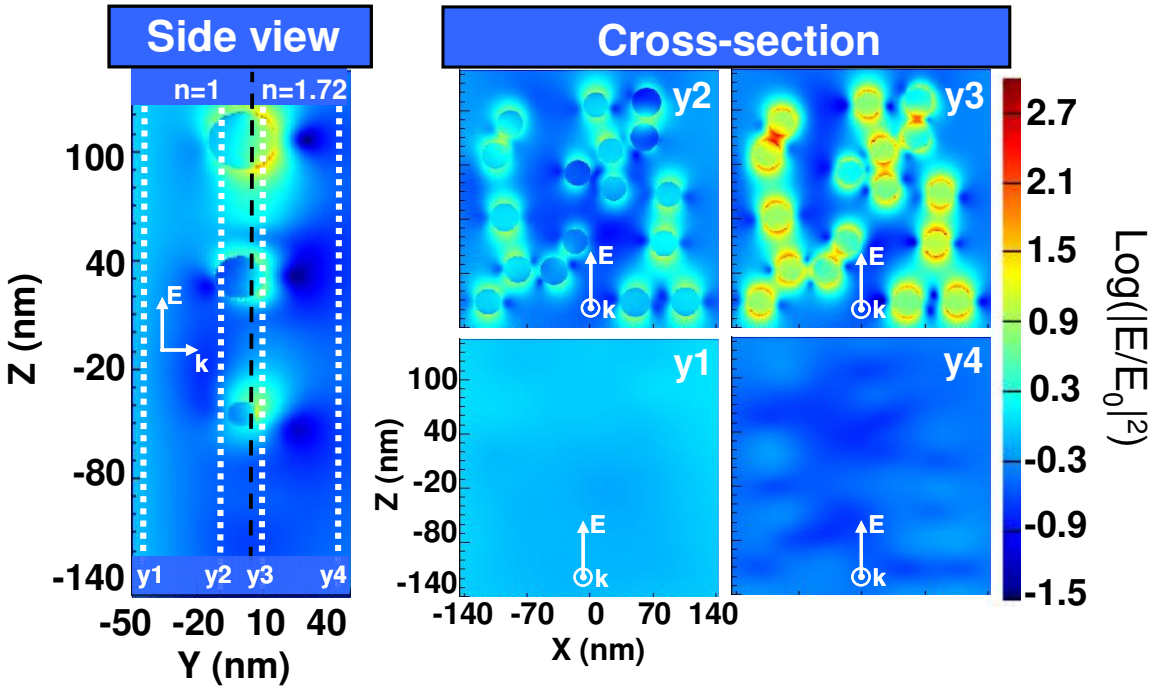

***Figure 4.11**: 3D spatial distribution of the field enhancement factor calculated for the Ag NPs with surface coverage as depicted in Figure 4.7h (N=17 randomly arranged Ag NPs; D=36 nm; centers located in ZX plane at Y=0) at wavelength λ=457 nm . The field enhancement mapping in ZY (X=0) plane (side view) and four cross-sectional profiles in ZX plane corresponding to white dashed lines plotted on the left (side view) part.*

Further, far-field absorption, scattering and extinction spectra of our plasmonic nanostructures were calculated as illustrated in **Figure 4.12**. The inset shows an experimental extinction spectrum for comparison. As one can see, spectral position of the extinction maximum is considerably red-shifted in comparison to single Ag NP with the same characteristic size (**Figure 4.3**). This observation reflects impact of dielectric constant of surrounding medium on the plasmon resonance peak position, when with increasing dielectric constant/refractive index a red-shift is observable [30]. Additionally, broadening of the spectra in comparison with a single NP is induced by collective near-field coupling of the

neighbouring Ag NPs. The good correlation found between the calculated extinction peak position and the experimental one is obtained by reasonable adjustments made to the fitting parameters, such as: Ag NP sizes, their surface density and immersion depth into the dielectric layer. Thus, scattering and absorption spectra can be theoretically analyzed without additional correlations with experiments. The studied spectral range was once again divided on two characteristic regions to separate coupled dipole plasmon modes from coupled multipole plasmon modes, as it was implemented in **Figure 4.3**. As one can see, the first region is mostly non-radiative due to absorptive nature of the extinction spectrum leading to excitation/absorption enhancement, while scattering phenomenon begins to play more important role in case of coupled dipole plasmon modes, thus increasing emission level by outcoupling of radiation into far-field [39].

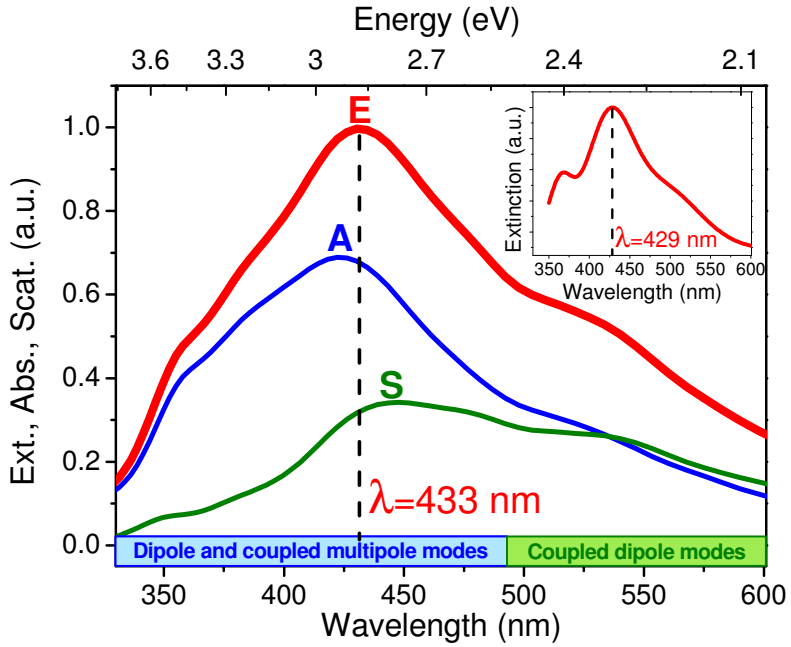

***Figure 4.12**: Calculated absorption (A), scattering (S), and extinction (E) spectra for the nano-Ag/SiN_X/glass substrates described above. Inset shows an experimental extinction spectrum of the plasmonic nano-Ag/SiNX/glass substrates for comparison.*

Figure 4.13 shows extinction spectra of the nano-Ag/SiN_X/glass structures with and without deposited SiC NPs. A baseline correction was performed for all spectra in order to subtract natural extinction related to the SiN_X layer without Ag NPs. Complex spectral features attributed to the overall plasmon modes simulated above can be clearly visible in both cases. The main spectral plasmon mode features are retained after a single-drop deposition of our colloidal SiC NPs, while their spectral positions are red-shifted of about 30nm. As discussed before, it is mainly related to the difference in effective dielectric constant of the local environment created around the Ag NPs by the deposited SiC QDs. In general, a precise spectral tuning of the local plasmon resonance can be ensured by amount of the deposited SiC NPs or by deposition of an additional SiNx layer as it was reported before.

In order to enhance PL of the SiC NPs deposited onto the nano-Ag/SiN_X/glass substrate, the first condition related to their photo-excitation with the wavelength λ= 457 nm matching perfectly extinction spectral maximum has to be satisfied. Indeed, in this case, the absorption cross-sections of the NPs are considerably increased due to their near-field interaction with the localized plasmons. Since the local field intensity enhancement is strongly dependent on the precise NP location on the silver nanostructure, only an averaged value of the field enhancement can be considered.

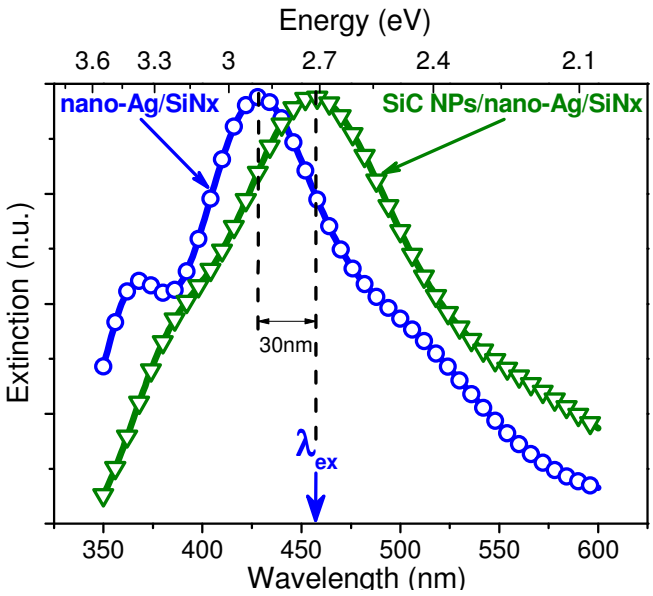

***Figure 4.13**: Extinction spectra of the nano-Ag/SiN_X structures before (blue circles) and after (green triangles) deposition of the SiC NPs.*

Room temperature PL spectra of the SiC NPs photo-excited with the laser wavelength λ= 457 nm is shown in **Figure 4.14**. PL spectra of the SiNx layer with and without deposited Ag NPs are also present in order to take into account its luminescent properties. Slight spectral and intensity PL difference between the SiNx and SiC NPs/SiNx samples reflects relatively small quantity of the deposited SiC NPs. The PL spectra of these samples mainly consist of well-known characteristic broad spectral red band [48] corresponding to the radiative transitions E_C -> Si^- between the conductive band bottom (E_C) of the SiNx matrix and Si^- defect states of the Si NPs present in the SiN_X layer. A small decrease of the red PL band can be observed for the nano-Ag/SiN_X/glass substrate which is due to the absorption and far-field backscattering of the laser excitation by Ag NPs. A green characteristic PL band (emission wavelength λ~530 nm) of the dielectric SiN_X layer related to the radiative transitions Si^0 ->N^- between the Si NPs and the defect state N^- of the SiNx film could also manifest as it was earlier reported [40]. However, this radiative channel is completely absent in the SiN_X substrates as it can be seen in **Figure 4.14**. Thus, the PL enhancement in 500-600 nm spectral range detected for the nano-Ag/SiNx/glass substrate with deposited SiC NPs is rather due to PL of the NPs and not to the green PL band of the SiN_X substrate.

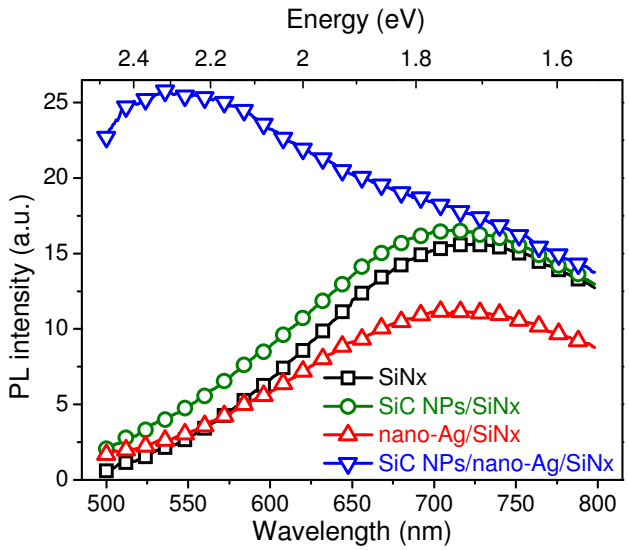

***Figure 4.14**: Room temperature PL spectra (excitation wavelength λ=457 nm) of: SiN_X substrate (black squares), SiC NPs deposited on SiN_X substrate (green circles), nano-Ag/SiN_X substrate (red triangles), and SiC NPs deposited on nano-Ag/SiN_X substrate (blue triangles).*

After subtraction of the corresponding references, PL spectra of the plasmon enhanced and original SiC NPs are shown in **Figure 4.15**. One can see that the SiC NPs deposited onto the nano-Ag/SiN_X/glass clearly show a drastic increase of their PL intensity in comparison with the spectrum obtained on a reference structure without the Ag NPs. It is worth noting that the PL peak is shifted toward the short-wavelength region revealing interaction of local plasmons with the emitting NPs. Spectral dependence of the PL enhancement factor obtained by division of the spectra is shown in inset of **Figure 4.15**. 6-fold enhancement level which remains constant at long-wavelength region (starting from about 630 nm) reflects an averaged excitation/absorption enhancement, while maximum 15-fold enhancement value reached at about 500 nm results from both absorption and emission enhancement. Moreover, a monotonic increase of the enhancement factor with decreasing emission wavelength perfectly correlates with a similar increase of the scattering/extinction spectra of the plasmonic nano-Ag/SiNx substrates in this spectral region (see **Figure 4.12** and **Figure 4.13**).

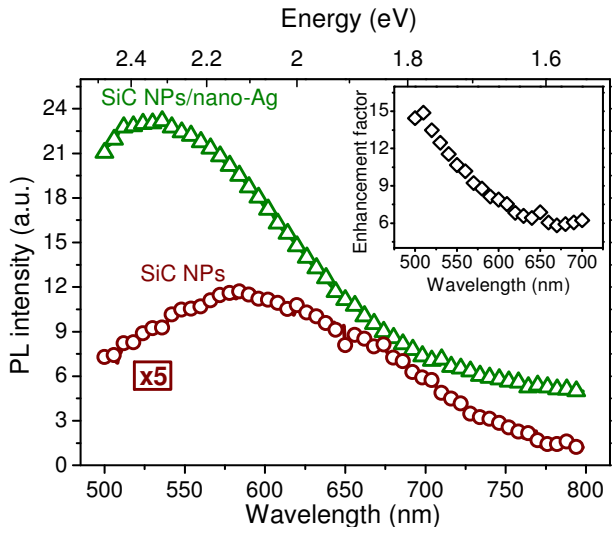

***Figure 4.15**: Corrected PL spectra of the SiC NPs on: SiN_X/glass (brown circles) and nano-Ag/SiN_X/glass (green triangles) substrates. Inset shows spectrum of the PL enhancement factor.*

The mentioned spectral overlap corresponds to the emission enhancement caused by the plasmon-induced modification of the ratio between non-radiative and radiative rates and, consequently, to a general increase of the PL intensities. Taking into account that: (i) the emission enhancement is strongly dependent on the distance between the luminescent and the plasmonic NPs [36, 38] and (ii) the Ag NPs are randomly distributed at the SiN_X surface, one can deduce that not all the SiC NPs are located at optimal distances from plasmon-induced enhancement condition point of view. Nevertheless, a significant PL signal increase of the SiC NPs is stated in the measurements with about 8.9-fold integral enhancement (the ratio between the integral intensities from the green-red spectral range) averaged over 10 independent PL measurements performed in different places at the substrate surface.

4.2.2.3. Nonlinear optical properties

To realize the plasmon-induced enhancement of NLO properties of the SiC NPs, plasmonic substrates shown in **Figure 4.7k** were used (Ag deposition time t=20 min). One can clearly see the characteristic sizes of the Ag NPs which are in the range of 40-65 nm. Some of these NPs are found to be overlapped due to their random arrangement leading sometimes to quite complex conformations. Nevertheless, the inter-particle distances range from a few to dozens nanometres in most cases. According to equations (4.10) and (4.11), a significant enhancement of the non-linear response is expected when local field factor at excitation wavelength reaches a maximum. Additionally, scattering efficiency should be reasonable at shorter wavelengths for SHG and emission enhancement of TPPL. These conditions are satisfied by prolonged nano-Ag deposition, which leads to a large size distribution and strong inter-particle coupling between the Ag NPs, as it can be seen in **Figure 4.7k**.

In order to theoretically estimate local field enhancement factors ($|E|^2/|E_0|^2$) at excitation and SH wavelengths as well as the final enhancement factor for SHG (η_{SHG}, according to equation (4.10)) induced by metallic NPs, numerical three-dimensional FDTD calculations were performed. Similar FDTD simulations were found to be reasonable in estimation of high-harmonic generation [9], and TPPL of Au, Ag and Al nanostructures [49]. Surface density (130 NPs per 1 μm^2) and size distribution (D=40-65 nm) were depicted from the experimental AFM image given in **Figure 4.7k**. Simulation area was chosen to be large enough (0.1 μm^2) in order to take into account the NP size distribution and inter-particle coupling effects, as well as to keep quite fine spatial grid to eliminate all numerical errors caused by finite size discretization. Different configuration of the simulated randomly-

arranged Ag NPs led only to insignificant changes in final results. Ag NPs were once again slightly immersed into the dielectric SiN_X thin film, i.e. centres of the thirteen simulated Ag NPs are located in a plane separated by a distance of 19 nm from the surface level of the SiN_X layer with refractive index n=1.72. In this way, the simulation conditions are very close to reality and allow gaining field enhancement mapping at the fabricated plasmonic substrates.

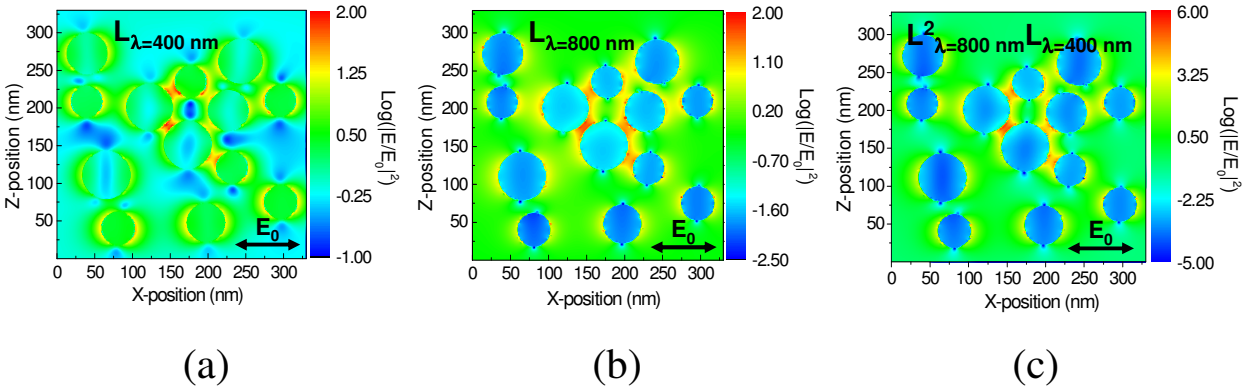

***Figure 4.16**: FDTD simulated field intensity enhancement factor distribution in logarithmic scale: (a) at fundamental wavelength (λ= 800 nm); (b) at SH wavelength (λ = 400 nm); and (c) for final SHG process.*

The calculated local field enhancements (in logarithmic scale) for excitation (λ= 800 nm) and SH (λ= 400 nm) wavelengths in the plane of the Ag NP centres can be seen in **Figure 4.16a** and **Figure 4.16b**, respectively. The highest field enhancement values (more than two orders of magnitude for both wavelengths) correspond to the relatively narrow inter-particle hot-spot regions. **Figure 4.16c** represents enhancement of the SHG intensity computed from the field enhancement maps shown in **Figure 4.16a,b**. Maximal SHG enhancement in the hot spots is more than of 10^6-fold higher in comparison with "no-metal" substrate, while the surface-averaged enhancement value is around 220-fold level.

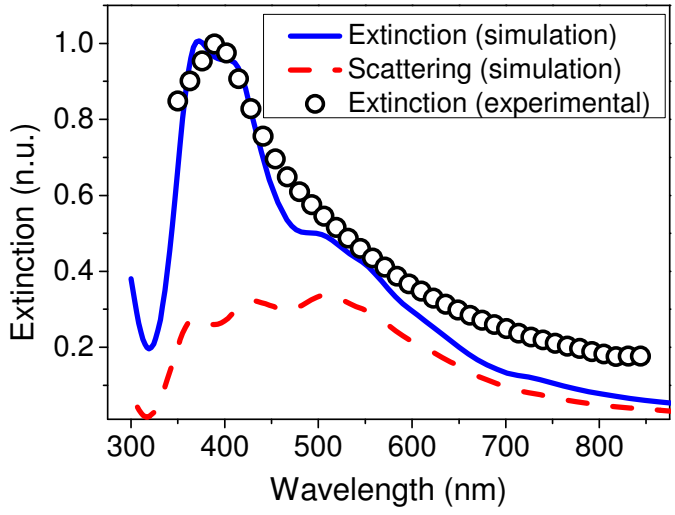

***Figure 4.17**: Calculated extinction spectrum (solid blue curve), calculated scattering (red dashed curve) spectrum and experimental extinction spectrum (circles).*

Far-field scattering and extinction spectra are simulated in order to estimate plasmon-induced emission enhancement in the TPPL process. The normalized simulated and experimental extinction spectra are compared in **Figure 4.17**. A good correlation of the spectral peak positions can be stated, which is partially due to the reasonable trial-and-errors fitting of the immersion depth of the Ag NPs into the dielectric layer. It is worth noting that slight differences at the long wavelength region are caused by still insufficient size of the simulated region, and small discrepancy between physical phenomena in closely spaced NPs (s<1 nm) and implemented FDTD (see discussion on near-field coupling). Nevertheless, in present case number of such closely interacting NPs is rather small and thus the performed simulation gives an excellent way to estimate an order of magnitude for the field enhancement and scattering efficiency of such samples.

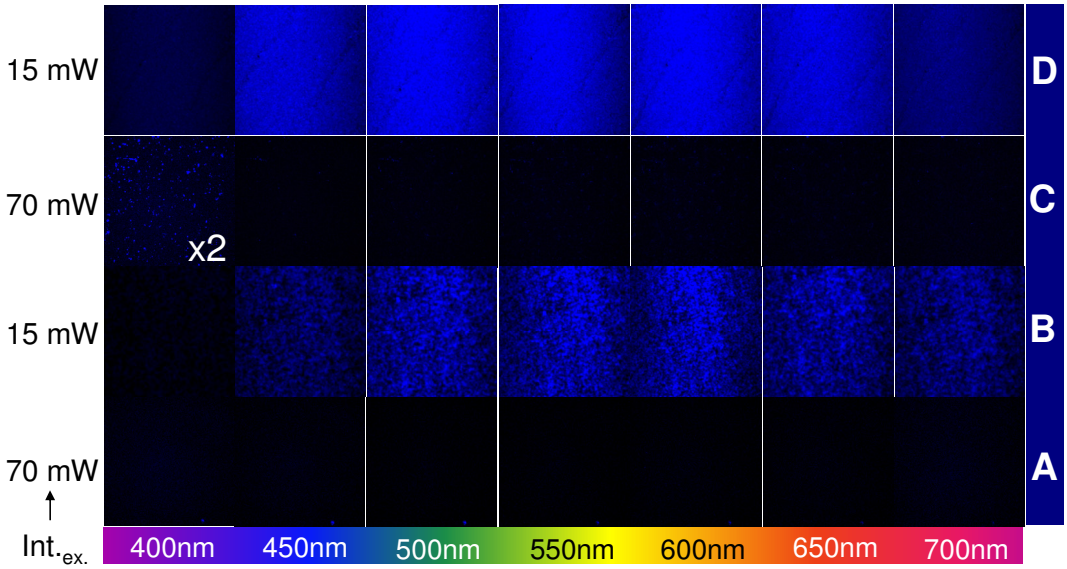

***Figure 4.18**: Fluorescence microscopy images of SiNx (a), nano-Ag/SiNx (b), SiC NPs/SiNx (c) and SiC NPs/nano-Ag/SiNx (d) samples, for SH (400nm) and several TPPL wavelengths (450, 500, 550, 600, 650 and 700 nm) with corresponding excitation (λ= 800 nm) laser power.*

To experimentally study the plasmon-induced enhancement of the samples nonlinear response, they were excited at λ=800nm with a femtosecond laser. Since each sample component, such as: SiNx layer with Si NPs, Ag NPs and SiC NPs can naturally exert a specific nonlinear response, they were separately investigated. Typical two-photon scanning microscopy images with detection set for SH (λ=400nm) and TPPL (λ=450-700nm) are presented in **Figure 4.18**. The excitation power was adjusted for each image set to better highlight the observed enhancement level. In particular, the excitation power was systematically reduced for the samples with strong emission level to avoid saturation. Image

rows correspond to the following samples: a) standalone dielectric SiNx thin film; b) SiNx film with Ag NPs; c) SiNx film with deposited SiC NPs; d) nano-Ag/SiN_X with deposited SiC NPs.

Despite the fact that the second-order susceptibility term $\chi^{(2)}$ is close to zero for centrosymmetric bulk silicon crystals, the earlier reported SHG and TPPL [50-52] are mostly caused by the shape irregularities and broken crystalline symmetry at interfaces. Since neither SHG nor TPPL were detected in the case of SiNx layer (image row A), it is reasonable to conclude that the chosen excitation laser power (70 mW) is not sufficiently high to observe corresponding NLO response. However, an increased TPPL signal was observed (see images in row B) even at 15 mW of the excitation power after deposition of Ag NPs at the SiNx surface. SHG was also detected in this case (see quantitative data discussed below) but it can not be clearly seen on the corresponding image. The observed enhancement of the NLO signals can be simultaneously related to the two following mechanisms: 1) plasmon-induced enhancement of NLO responses of Si NPs located in close vicinity to Ag NPs and 2) near-field SHG and luminescence from the nanostructured Ag [49, 53].

In comparison to the standalone SiNx layer (image row A), SiNx layer with the deposited SiC NPs (image row C) demonstrate a slight increase of SHG signal. The luminosity of the corresponding picture was numerically increased by 2 times to visualize the original SHG from the nano-SiC. Since the band-gap of bulk SiC substrate is 2.3eV (λ=540 nm), efficient SHG at 3.1 eV (λ=400 nm) occurs in SiC NPs with the band-gap values (E_G> 3.1 eV) increased due to quantum confinement effect to satisfy the following condition: $E_{SHG}<E_G$. On the other hand, deposition of the same quantity of SiC NPs on the nano-Ag/SiNx substrate provokes a substantial rise of nonlinear response (image row D), in comparison with the previous case (image row C). Furthermore, for correct comparison of the corresponding responses and taking into account quadratic dependence of the SHG and TPPL signals on excitation power [45], the enhancement of the NLO signals was calculated for: a) nano-Ag/SiNx complex; and for b) SiC NPs. In the second case, the values of SHG and TPPL related to the nano-Ag/SiNx were subtracted and divided on the detected signal emitted from the SiC NPs/SiNx. The corresponding enhancement factors are represented by histograms in the **Figure 4.19**. Additionally, scattering efficiency of the plasmonic nano-Ag/SiNx substrate is plotted to show the role of the plasmon-induced enhancement on the emission part of TPPL. Even if no signal is visible on the SHG microscopy pictures in image sets A and B in **Figure 4.18**, the calculated value of the SHG enhancement factor of the Ag-Si NPs complex is 23-fold. At the same time, SHG enhancement magnitude related to the SiC NPs is 72-fold,

somewhat lower than estimated (220) numerically. This is related to the fact that during the drying of the colloidal suspension some part of the SiC NPs creates agglomerates extending in and/or out of the high field regions. Thus, the exact localization of SiC NPs is not a priori known. Moreover, when surface averaged SHG enhancement was estimated in the plane of the most probable localization of SiC NPs (4 nm above the dielectric layer), only 44-fold enhancement has been obtained. This is why, the calculated 220-fold surface averaged SHG enhancement gives an order of magnitude of the possible enhancement level and which is in quite good correlation with the obtained experimental results.

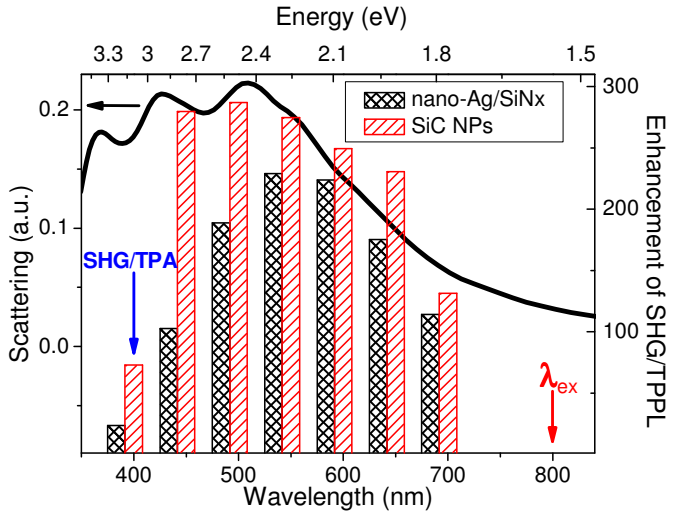

***Figure 4.19**: Calculated enhancement factor for SHG and TPPL (excitation wavelength λ= 800 nm) for Si NPs/nano-Ag (cross patterned black bars) and SiC NPs (diagonally patterned red bars).*

In the case of TPPL, plasmon-induced enhancement is more complex, since the localized plasmons influence not only TPA but also the recombination rate of the radiative electronic transition. Non-constant TPPL spectral enhancement of SiC NPs with maximum 287-fold value recorded at λ=500 nm gives a direct indication on such mechanism. In the case of nano-Ag/SiN_X complex (with maximum 228-fold enhancement value), the TPPL signal is ensured not only by plasmon enhanced Si NPs from the SiN_X layer but also directly by Ag NPs. It is worth remarking that the TPPL enhancement of the SiC NPs follows scattering spectral efficiency of the plasmonic nano-Ag/SiNx substrate. **Figure 4.15** illustrates a similar enhancement behaviour in the experiments with one-photon excited (at λ=457 nm) photoluminescence, reaching 15-fold enhancement. In both cases, the increased emission level is caused by wavelength-dependent scattering efficiency governing ability of the plasmonic nanostructure to outcouple the radiation into far-field [36, 39]. It is worth emphasizing that the role of plasmon enhancement for TPPL is much more efficient in comparison with one-photon excited photoluminescence (287-fold versus 15-fold enhancement, respectively), due to the quadratic dependence of the non-linear absorption on the local field factors at these excitation wavelengths.

4.3. Conclusions

PL enhancement of the SiC NPs induced by their efficient near-field coupling with multi-polar localized plasmons is experimentally demonstrated in this chapter. In order to understand and illustrate main physical mechanisms involved in a complex interaction between the localized plasmons and emitting SiC NPs three-dimensional FDTD simulations were performed to estimate absorption and scattering efficiencies of the used nano-Ag/SiN_X/glass substrates. In particular, PL enhancement factors reaching a value of 15 are ensured by localization of the SiC NPs at the plasmon-induced high field regions as well as by a spectral overlap of multi-polar plasmon modes with absorption/excitation and emission bands of the NPs.

Moreover, a detailed experimental study of the plasmon-induced enhancement of non-linear response in SiC NPs was presented. Despite a number of studies devoted to the clarification of the physical mechanisms involved in such phenomenon, none of them was explicitly addressed to the case of SiC NPs. In particular, SHG enhancement factor reaching 72-fold level is ensured by localization of the SiC NPs in the high field regions as well as by a spectral overlap of multi-polar plasmon modes with excitation and SH wavelengths. The developed nano-Ag/SiN_X plasmonic substrates ensured also maximal 287-fold enhancement of TPPL of the SiC NPs, thus reflecting in general a significant plasmon-induced enhancement of their NLO properties.

4.4. References

1. OKAMOTO K., NIKI I., SHVARTSER A., et al. Surface-plasmon-enhanced light emitters based on InGaN quantum wells. Nature Materials, 2004, vol. 3, p.601–605.
2. POMPA P.P., MARTIRADONNA L., TORRE A.D., et al. Metal-enhanced fluorescence of colloidal nanocrystals with nanoscale control. Nature Nanotechnology, 2006, vol. 1, p.126–130.
3. JIN Y., GAO X. Plasmonic fluorescent quantum dots. Nature Nanotechnology, 2009, vol. 4, no. 9, p.571–576.
4. MA X., TAN H., KIPP T., et al. Fluorescence enhancement, blinking suppression, and gray states of individual semiconductor nanocrystals close to gold nanoparticles. Nano Letters, 2010, vol. 10, p.4166–4174.
5. TAM F., GOODRICH G.P., JOHNSON B.R., et al. Plasmonic enhancement of molecular fluorescence. Nano Letters, 2007, vol. 7, no. 2, p.496–501.
6. ZHANG Y., GRADY N.K., AYALA-OROZCO C., et al. Three-Dimensional Nanostructures as Highly Efficient Generators of Second Harmonic Light. Nano Letters, 2011, vol. 11, p.5519–5523.
7. PARK I.-Y., KIM S., CHOI J., et al. Plasmonic generation of ultrashort extreme-ultraviolet light pulses. Nature Photonics, 2011, vol. 5, p.677–681.
8. PU Y., GRANGE R., HSIEH C., et al. Nonlinear Optical Properties of Core-Shell Nanocavities for Enhanced Second-Harmonic Generation. Physical Review Letters, 2010, vol. 104, no. 207402.
9. KIM S., JIN J., KIM Y.-J., et al. High-harmonic generation by resonant plasmon field enhancement. Nature, 2008, vol. 453, p.757–760.
10. ATWATER H.A., POLMAN A. Plasmonics for improved photovoltaic devices. Nature Materials, 2010, vol. 9, p.205–13.
11. ZHANG J., FU Y., LIANG D., et al. Enhanced fluorescence images for labeled cells on silver island films. Langmuir, 2008, vol. 24, no. 21, p.12452–12457.
12. GOVOROV A.O., RICHARDSON H.H. Generating heat with metal nanoparticles. NanoToday, 2007, vol. 2, no. 1, p.30–38.
13. HUANG X., QIAN W., EL-SAYED I.H., et al. The potential use of the enhanced nonlinear properties of gold nanospheres in photothermal cancer therapy. Lasers in Surgery and Medicine, 2007, vol. 39, p.747–753.

14. BOTSOA J., LYSENKO V., GÉLOËN A., et al. Application of 3C-SiC quantum dots for living cell imaging. Applied Physics Letters, 2008, vol. 92, no. 173902.
15. FAN J., LI H., JIANG J., et al. 3C-SiC nanocrystals as fluorescent biological labels. Small, 2008, vol. 4, no. 8, p.1058–1062.
16. FAN J.Y., LI H.X., WANG Q.J., et al. UV-blue photoluminescence from close-packed SiC nanocrystal film. Applied Physics Letters, 2011, vol. 98, no. 081913.
17. WANG J., XIONG S.J., WU X.L., et al. Glycerol-bonded 3C-SiC nanocrystal solid films exhibiting broad and stable violet to blue-green emission. Nano Letters, 2010, vol. 10, p.1466–1471.
18. DING J.-L., WANG Y.-C., ZHOU H., et al. Nonlinear Optical Properties and Ultrafast Dynamics of Undoped and Doped Bulk SiC. Chinese Physics Letters, 2010e, vol. 27, no. 124202.
19. SATO H., ABE M., SHOJI I., et al. Accurate measurements of second-order nonlinear optical coefficients of 6H and 4H silicon carbide. Journal of the Optical Society of America B, 2009, vol. 26, no. 10, p.1892–1896.
20. WU I.J., GUO G.Y. Second-harmonic generation and linear electro-optical coefficients of SiC polytypes and nanotubes. Physical Review B, 2008, vol. 78, no. 035447.
21. CHAO L.C., STECKL A.J. CW blue-green light emission from GaN and SiC by sum-frequency generation and second harmonic generation. Journal of Electronic Materials, 2000, vol. 29, no. 9, p.1059–1062.
22. NIEDERMEIER S., SCHILLINGER H., SAUERBREY R., et al. Second-harmonic generation in silicon carbide polytypes. Applied Physics Letters, 1999, vol. 75, no. 5, p.618–620.
23. RASHKEEV S.N., LAMBRECHT W.R.L., SEGALL B. Second-harmonic generation in SiC polytypes. Physical Review B, 1998, vol. 57, no. 16, p.9705–9715.
24. BORSHCH A.A., BRODYN M.S., VOLKOV V.I., et al. Nonlinear refraction in nanocrystalline silicon carbide films. JETP Letters, 2008, vol. 88, no. 6, p.386–388.
25. KONOROV S.O., IVANOV A.A., ALFIMOV M.V., et al. Generation of the second and third harmonics of femtosecond Cr: forsterite laser pulses in SiC/PMMA nanopowder films. Laser Physics Letters, 2004, vol. 1, no. 1, p.37–41.
26. KONOROV S.O., SIDOROV-BIRYUKOV D.A., BUGAR I., et al. Diffuse optical harmonic generation in SiC nanopowder films: hunting scattered photons. Applied Physics B, 2004, vol. 78, p.73–77.

27. KITYK I.V., KASSIBA A., BENET S. Origin of Nonlinear Optical Susceptibility in SiC Nanocrystallites. Journal of Cluster Science, 2001, vol. 12, no. 2, p.399–419.
28. KITYK I.V., MAKOWSKA-JANUSIK M., KASSIBA A., et al. SiC nanocrystals embedded in oligoetheracrylate photopolymer matrices; new promising nonlinear optical materials. Optical Materials, 2000, vol. 13, p.449–453.
29. PALIK E.D. Handbook of optical constants of solids. Orlando: Academic Press, 1985.
30. MAIER S.A. Plasmonics: fundamentals and applications. 1st edn. New York: Springer, 2007, 223 p.
31. MAIER S.A., ATWATER H.A. Plasmonics: Localization and guiding of electromagnetic energy in metal/dielectric structures. Journal of Applied Physics, 2005, vol. 98, no. 011101.
32. KUMBHAR A.S., KINNAN M.K., CHUMANOV G. Multipole plasmon resonances of submicron silver particles. Journal of the American Chemical Society, 2005, vol. 127, no. 36, p.12444–12445.
33. YAN J.-Y., ZHANG W., DUAN S., et al. Optical properties of coupled metal-semiconductor and metal-molecule nanocrystal complexes: Role of multipole effects. Physical Review B, 2008, vol. 77, no. 165301.
34. ZULOAGA J., PRODAN E., NORDLANDER P. Quantum description of the plasmon resonances of a nanoparticle dimer. Nano Letters, 2009, vol. 9, no. 2, p.887–891.
35. LASSITER J.B., AIZPURUA J., HERNANDEZ L.I., et al. Close encounters between two nanoshells. Nano Letters, 2008, vol. 8, no. 4, p.1212–1218.
36. MERTENS H., KOENDERINK A.F., POLMAN A. Plasmon-enhanced luminescence near noble-metal nanospheres: Comparison of exact theory and an improved Gersten and Nitzan model. Physical Review B, 2007, vol. 76, no. 115123.
37. CHEN Y., MUNECHIKA K., GINGER D.S. Dependence of fluorescence intensity on the spectral overlap between fluorophores and plasmon resonant single silver nanoparticles. Nano Letters, 2007, vol. 7, no. 3, p.690–6.
38. BHARADWAJ P., NOVOTNY L. Spectral dependence of single molecule fluorescence enhancement. Optics Express, 2007, vol. 15, no. 21, p.14266–14274.
39. MUNECHIKA K., CHEN Y., TILLACK A.F., et al. Spectral control of plasmonic emission enhancement from quantum dots near single silver nanoprisms. Nano Letters, 2010, vol. 10, p.2598–2603.

40. NYCHYPORUK T., ZAKHARKO Y., SERDIUK T., et al. Strong photoluminescence enhancement of silicon quantum dots by their near-resonant coupling with multi-polar plasmonic hot spots. Nanoscale, 2011, vol. 3, p.2472–2475.
41. LIU N., PRALL B.S., KLIMOV V.I. Hybrid gold/silica/nanocrystal-quantum-dot superstructures: synthesis and analysis of semiconductor-metal interactions. Journal of the American Chemical Society, 2006, vol. 128, no. 48, p.15362–15363.
42. GENEVET P., TETIENNE J.-P., GATZOGIANNIS E., et al. Large Enhancement of Nonlinear Optical Phenomena by Plasmonic Nanocavity Gratings. Nano Letters, 2010, vol. 10, p.4880–4883.
43. BOUHELIER A., BEVERSLUIS M., HARTSCHUH A., et al. Near-Field Second-Harmonic Generation Induced by Local Field Enhancement. Physical Review Letters, 2003, vol. 90, no. 013903.
44. CHEN C.K., CASTRO A.R.B., SHEN Y.R. Surface-enhanced second-harmonic generation. Physical Review Letters, 1981, vol. 46, no. 2, p.145–148.
45. BHAWALKAR J.D., HE G.S., PRASAD P.N. Nonlinear multiphoton processes in organic and polymeric materials. Reports on Progress in Physics, 1996, vol. 59, p.1041–1070.
46. NYCHYPORUK T., ZHOU Z., FAVE A., et al. Electroless deposition of Ag nanoparticles on the surface of SiNx:H dielectric layers. Solar Energy Materials and Solar Cells, 2010, vol. 94, p.2314–2317.
47. XU G., TAZAWA M., JIN P., et al. Wavelength tuning of surface plasmon resonance using dielectric layers on silver island films. Applied Physics Letters, 2003, vol. 82, no. 22, p.3811–3813.
48. MO C., ZHANG L., XIE C., et al. Luminescence of nanometer-sized amorphous silicon nitride solids. Journal of Applied Physics, 1993, vol. 73, no. 10, p.5185–5188.
49. CASTRO-LOPEZ M., BRINKS D., SAPIENZA R., et al. Aluminum for nonlinear plasmonics: resonance-driven polarized luminescence of Al, Ag, and Au nanoantennas. Nano Letters, 2011, vol. 11, p.4674–4678.
50. NAYFEH M.. H., AKCAKIR O., BELOMOIN G., et al. Second harmonic generation in microcrystallite films of ultrasmall Si nanoparticles. Applied Physics Letters, 2000, vol. 77, no. 25, p.4086–4088.
51. HE G.S., ZHENG Q., YONG K.-T., et al. Two- and Three-Photon Absorption and Frequency Upconverted Emission of Silicon Quantum Dots. Nano Letters, 2008, vol. 8, no. 9, p.2688–2692.

52. JIANG Y., WILSON P.T., DOWNER M.C., et al. Second-harmonic generation from silicon nanocrystals embedded in SiO_2. Applied Physics Letters, 2001, vol. 78, no. 6, p.766–768.
53. BORYS N.J., WALTER M.J., LUPTON J.M. Intermittency in second-harmonic radiation from plasmonic hot spots on rough silver films. Physical Review B, 2009, vol. 80, no. 161407(R).

Chapter 5

Bio-Imaging Applications and Perspectives

Silicon carbide nanostructures due to interesting physico-chemical properties have already found numerous applications as discussed in Chapter 1. This chapter will focus on a deeper analysis of SiC as fluorescent agent in cell biology.

At the present time, colour imaging and "multiplexing" (simultaneous detection of multiple signals) of bio-objects usually requires their labelling by various fluorescent molecules [1-4] or colloidal QDs [5-8]. In many cases, dye molecules demonstrate high emission QY, but their narrow excitation spectrum makes simultaneous excitation difficult, and their broad emission spectrum with a long tail at red wavelengths introduces spectral cross talk between different detection channels [5]. General drawback in fluorescent molecules of low photo-stability or photo-bleaching under intense excitation has been struggled by discovering green fluorescent protein (GFP) and its variants [3]. On the other hand, solid-state luminescent nanostructures provide tuneable and narrow emission in UV-blue (ZnS, ZnSe, CdS), green-yellow (CdSe, CdTe) and red-IR (PbS, PbSe) spectral ranges [9-14]. Further, high QY, low photo-bleaching and high value of optical absorption making QDs an ideal probes for multicolour experiments where the whole group of probes is excitable at a single wavelength. It has been also demonstrated that colloidal QDs can have an orders of magnitude larger TPA cross section compared with conventional organic fluorophores [15]. This makes them suitable for in vivo deep-tissue imaging using two-photon excitation at low intensities. The main drawbacks of QDs are their intermittency (blinking) under continuous excitation [16], interaction with cell functioning and possible cytotoxicity due to chemical degradation [17, 18]. As one can see, fluorescent dyes/proteins and QDs have their own advantages and drawbacks and they will complement their deficiencies in particular applications.

It should be made clear that not all QDs are alike. As mentioned before chemically inert, stable and biocompatible SiC NPs were successfully used in biological cell imaging [19, 20]. It is also interesting that SiC NPs were found to easily label cells and especially nucleus without any additional surface functionalization. Nevertheless, surface of SiC NPs with natural presence of carboxylic acid groups can be easily modified when needed. In general, biochemical surface coverage (antibodies, enzymes, etc.) is used to precisely localize NPs in specific cell compartments. Likewise, only few works paid attention to the influence of surface charge or hydrophobicity of NPs on localization inside the cell and the nucleus [21]. It was recently reported on the selective intracellular targeting of SiC NPs by controlling their surface charges [22]. For the first time authors have experimentally shown that electrical charge of few nm agents play a critical role on their ability of self-penetration through the nuclear pore complex (NPC). Towards this end, grafting of amino groups on the SiC NPs surface was performed via the reaction of their surface carboxylic acid groups with ethylenediamine. The considered procedure did not significantly modified PL spectra of colloidal SiC NPs suspensions with -30, +4 and +100 mV zeta-potentials. These results are in contrast to the spectral changes discussed in Chapter 3, where PL spectra for samples with small surface charge demonstrated red-shift due to dominant role of large NPs. The probable reason of such inconsistency lies in size segregation of NPs obtained during sample preparation and chemical treatment. In this case only smallest particles are present in the suspension and thus no significant spectral changes can be detected. The fluorescence images shown in **Figure 5.1** clearly highlight selective incorporation of the fluorescent SiC NPs inside the cell. The cells marked by the NPs are very bright (**Figure 5.1b, c, d**) while the autofluorescence of unmarked cells is not visible at all (**Figure 5.1a**) under the same excitation/detection conditions. In particular, the cells labelled with the negatively charged SiC NPs appear extremely bright with the most intense fluorescence signal coming from the nucleus (**Figure 5.1b**). Similar nucleus labelling effect can be observed for the case of the almost neutral SiC NPs (**Figure 5.1c**). However, a significant difference between the negatively charged and neutral SiC NPs concerns the cytoplasm labelling. A specific heterogeneous localization of the neutral NPs was explained by their zwitterionic nature increasing their affinity to the membranes. The images of cells exposed to the positively charged NPs are totally different (**Figure 5.1d**). In comparison with the negative and neutral SiC NPs, the nuclei are not labelled and remain completely dark, whereas most of the positively charged SiC NPs are forming filament-like structures in the cytoplasm. The authors proposed explanation of selective charge dependent localization of NPs inside the nucleus due

to the structure of the NPC. The NPC is composed of different components characterized by net positive charge. This suggests that electrostatic interactions between SiC NPs and the NPC are an essential part of the selective filtering mechanism. Together with results discussed in Chapter 3 on the role of surface modification and/or surrounding environment on the initial optical properties of SiC NPs, these findings will help expanding of SiC NPs applicability as a modern fluorescent agent.

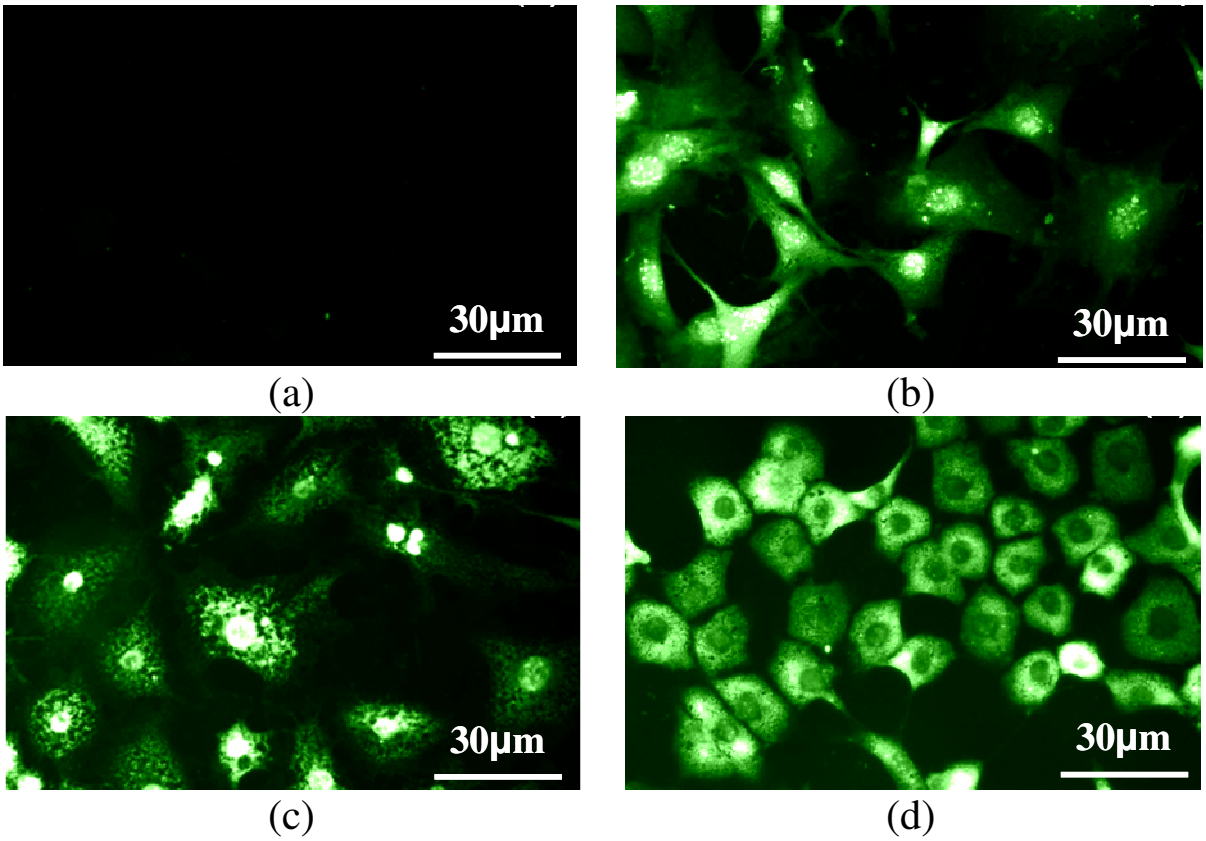

Figure 5.1*: Fluorescence images of 3T3-L1 cells: (a) without SiC NPs; (b) labelled with negatively charged (zeta potential -30 mV), (c) labelled with quasi neutral (zeta potential +4 mV), and (d) labelled with positively charged (zeta-potential +100 mV) SiC NPs [22].*

SiC NPs have, however, few disadvantages preventing their use in more complex bio-imaging applications. This includes low quantum yield (see Chapter 3) and very broad emission band (due to large size distribution), ranging from 400 to 800 nm, which makes multicolour imaging difficult. Low QY also influences concentration at which labelling effect is detectable. Botsoa et al. [23] have reported decrease of cell proliferation starting from 0.25 mg/ml SiC NPs concentration. In this case, even if SiC NPs are chemically nontoxic, their high concentration in the cell nucleus alters cell proliferation. Therefore, to compete with usual fluorophores, the PL of SiC NPs has to be enhanced from intensity and spectral bandwidth points of view.

In the first section of this chapter it will be shown how significant luminescence enhancement of fibroblast cells labelled with the SiC NPs can be obtained by localization on the nano-Ag/SiN_X/glass plasmonic substrates. In this way, low PL QY as the main problem of SiC NPs can be overcame. In case of conventional fluorescence dyes used in bio-imaging under near-field interaction with localized plasmons, greatly improved emission intensity, shortened life-time, and extended photostability [24-26] have been already demonstrated. Moreover, intrinsic fluorescence enhancement of several fluorescent proteins was also discussed [27, 28].

Further, fluorescent-plasmonic nanohybrids (NHs) were fabricated for advanced bio-imaging applications. The last section is devoted to the demonstration and characterization of elaborated hybrid structures. These NHs consist of a gold core overcoated with a silica shell, followed by the addition of SiC NPs onto the surface. In theory, this architecture allows precise tuning of NP-metal interactions by control of the core size (and potentially shape and composition) and the thickness of the dielectric spacer. The first one, allows spectral match between excitation/absorption and/or emission bands to the plasmon modes. Secondly, variable silica shell thickness ensures control of PL quenching and enhancement. Similar nanostructures were fabricated by other groups to enhance PL of organic dyes [29] or inorganic QDs [30]. The originality of the approach discussed in last section lies in the combination of only chemically inert materials (silica, SiC) in order to elaborate in perspectives a potential 'all-biocompatible' nanoprobe.

5.1. Plasmonic nanostructures for enhanced cell imaging

To illustrate application of the nano-Ag/SiN_X/glass substrates for plasmon-enhanced fluorescent imaging of cells labelled with the SiC NPs, cell cultures of 3T3-L1 fibroblasts were used. The cells were grown on glass and nano-Ag/SiN_X/glass substrates in Dulbecco's modified Eagle's medium (DMEM) supplemented with 10% newborn calf serum, 4 mM glutamine, 4 nM insulin (Actrapid Human; Novo), 10 mM Hepes, 25 µg sodium ascorbate, 100 IU penicillin, 100 µg streptomycin, and 0.25 mg/l amphotericin B at 37°C in a water saturated atmosphere with 5% CO_2 in air, in a Heraeus incubator (BB16). The cells were incubated for 6 hours in presence of the SiC NPs (with concentration of 0.4 g/L) dispersed in the DMEM.

Fluorescence images of fibroblast cells on glass and plasmonic substrates with or without SiC NPs can be seen in **Figure 5.2**. All images were obtained under the same

observation conditions in terms of excitation (UV/violet excitation band (λ=350-460 nm) and an observation spectral range corresponding to the wavelengths λ >470 nm) and acquisition time. Natural fluorescence of the cells grown on the usual glass cover slip substrates is too weak to be observed in such experimental conditions (**Figure 5.2a**). On the other hand, the cells grown on the glass substrates and labelled with the SiC NPs can be better seen in **Figure 5.2b** which is in perfect accordance with the studies reported earlier [19, 20]. Strong auto-fluorescence enhancement of the fibroblast cells grown onto the nano-Ag/SiN_X/glass substrates is shown in **Figure 5.2c**. This label-free natural green cell auto-fluorescence is significantly increased in comparison with the cells grown on a simple glass substrate (**Figure 5.2a**). The cells with the up-taken SiC NPs grown onto the nano-Ag/SiN_X/glass substrates show a drastic fluorescence enhancement (**Figure 5.2d**) in comparison to the cells containing the same quantity of the SiC NPs and grown on a usually-used glass cover slips (**Figure 5.2b**).

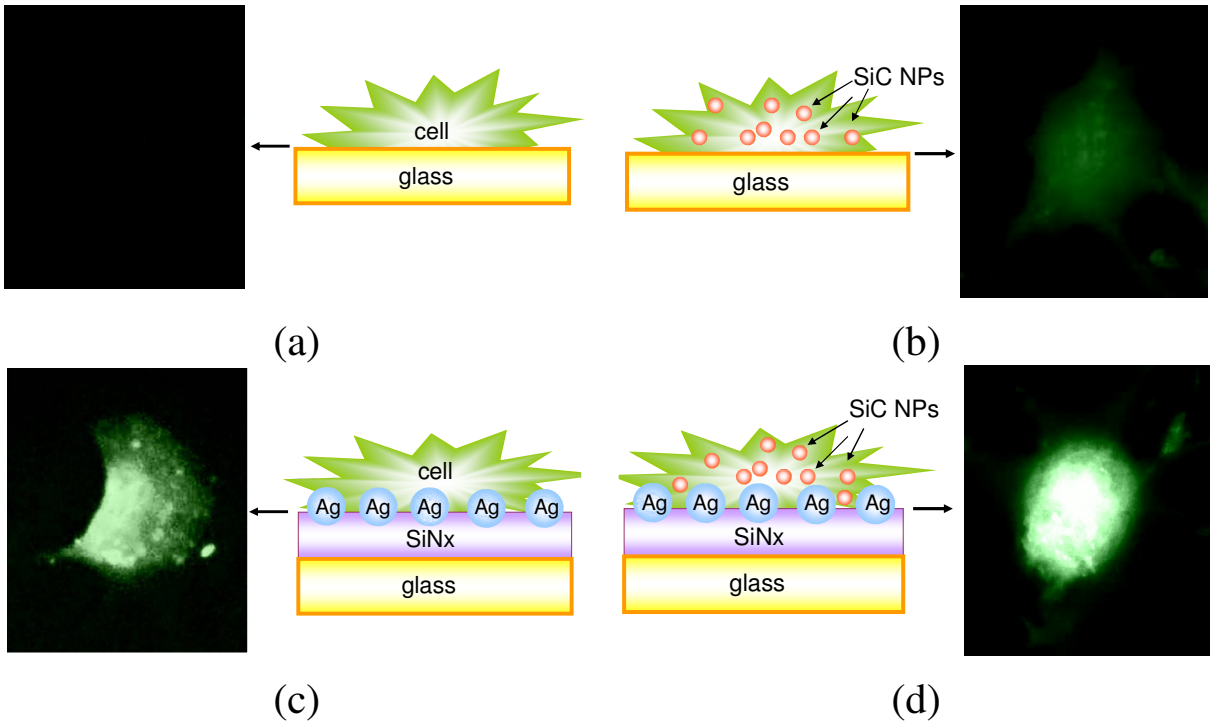

***Figure 5.2**: Sample schematics and corresponding fluorescent images of fibroblast cells: (a) on glass substrate, (b) labelled with the SiC NPs on glass substrate, (c) on nano-Ag/SiN_X/glass substrate, (d) labelled with the SiC NPs on nano-Ag/SiN_X/glass substrate.*

Different mechanisms can be responsible for the observed fluorescence enhancement of the cells. Firstly, as discussed above for the SiC NPs, the localized plasmons appearing in the Ag NPs leads to an increase of excitation/absorption and photostimulated auto-emission of the cell membranes due to their close proximity to the Ag NPs. A similar effect of the plasmon induced fluorescence enhancement of dye-labelled cell membranes was previously

reported [24]. As it is highlighted by the authors, the fluorescence enhancement can be only observable when the plasmons are localized in very close vicinity to the cell membrane. Moreover, the cell membrane thickness is estimated to be around a few nanometres, which allows plasmon-induced PL enhancement of the NPs up-taken by the cells and localized near the membrane after the dehydration and the subsequent fixation of the cells on the plasmonic nano-Ag/SiN_X/glass substrate. All these factors can explain the detected enhancement of cell auto-fluorescence and PL of the up-taken SiC NPs (see **Figure 5.2c** and **d**, respectively). Secondly, the cell labelling with the SiC NPs can induce modification of the local effective dielectric constant which will lead to a better near-field coupling (in terms of spectral overlap) with the localized plasmon modes under the same excitation conditions. In addition, the higher values of the local dielectric constant will also ensure the higher intensities of the plasmon-induced local electric field penetrating deeper inside the labelled cells. Finally, a certain degree of the excitation scattering within the nanostructured area and inside the cells may explain general PL enhancement taking place in the whole cell volume [31]. Moreover, the use of a UV/violet filter selecting the exciting photons from the relatively large spectral range (λ= 350-460nm) of a white lamp leads to a simultaneous photo-excitation of a wide absorptive part of the extinction spectra, provoking significant increase of the absorption cross-sections of numerous cell fluorescent agents as well as of a big number of the SiC NPs with various sizes. In addition, the auto-fluorescence cell signal and PL of the SiC NPs incorporated inside the cells (detected in the spectral range λ>470nm) are strongly enhanced by near-field interaction with the coupled dipole plasmon modes.

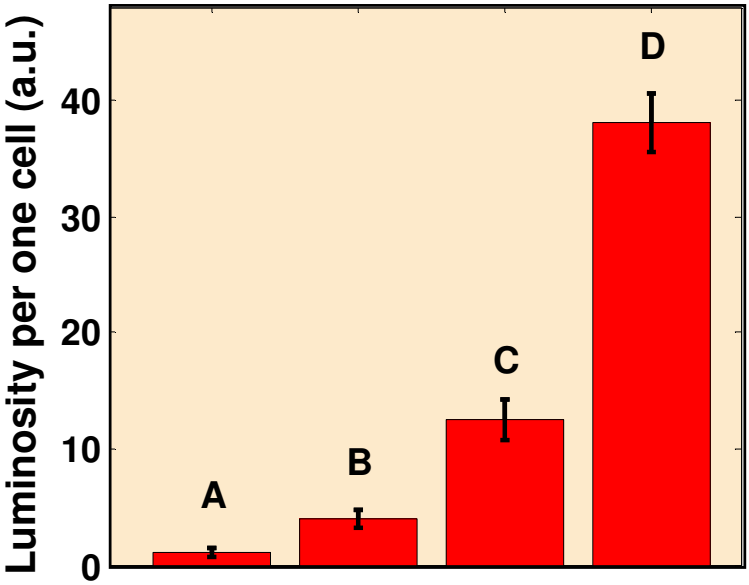

***Figure 5.3**: Calculated luminosity per one fibroblast cell: A on glass substrate, B labelled with the SiC NPs on glass substrate, C on nano-Ag/SiN_X/glass substrate, D labelled with the SiC NPs on nano-Ag/SiN_X/glass substrate.*

A quantitative comparison of the cell luminosities can be done using the data exposed in **Figure 5.3**. In particular, the plasmon-induced enhancement factor of the cell auto-fluorescence (column C / column A) is deduced to be equal to 10. To calculate the plasmon-induced PL gain of the SiC NPs used as the cell markers, luminosity of the non-labelled cells deposited on the nano-Ag/SiN_x/glass substrate (column C) is first subtracted from the luminosity of the cell containing the SiC NPs and deposited on the same nano-Ag/SiN_X/glass structure (column D). The resulted value (D-C) is then divided by the luminosity of the cell containing the SiC NPs deposited on the glass substrate (column B). The calculated PL enhancement of the SiC NPs is thus found to be around 8.

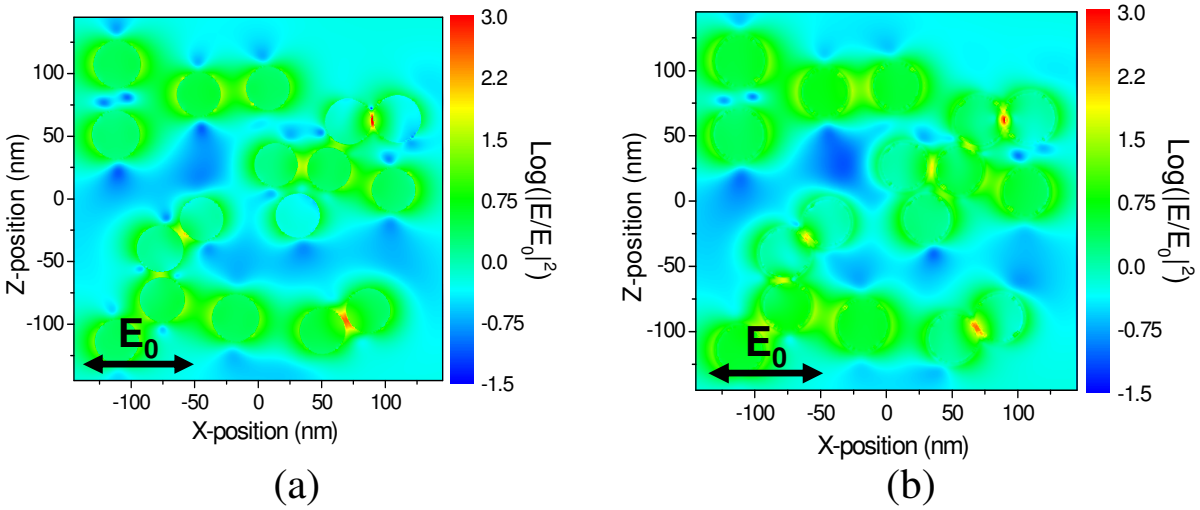

***Figure 5.4**: FDTD simulated field (λ = 457 nm) intensity enhancement factor distribution in logarithmic scale: (a) without, and (b) with 3-nm dielectric (n=1.55) layer.*

Since silver surface is known to be cytotoxic to the living cells, an additional simulation (analogous to the one discussed in Chapter 4, section 4.2.2.2) was performed to investigate an impact of a 3-nm dielectric (n=1.55) coating layer around the Ag NPs on the field intensity enhancement at wavelength λ=457 nm. As a result, the extinction peak position as well as surface-averaged value of the field enhancement (**Figure 5.4**) remained almost unchanged due to very slight changes of the surrounding effective dielectric constant caused by the coating.

5.2. Colloidal nanohybrids: towards bright biocompatible light emitters

Colloidal (Au@SiO_2)SiC nanohybrids were fabricated by the procedure described in Chapter 2. This method allows a good control of the size and morphology of silica shell larger than 10

nm depending on the amount of TEOS, solvent and basic reagent. At the moment, synthesis of homogenous silica shell smaller than 10 nm can not be well conducted. The size distribution of Au@SiO_2 particles was controlled using SEM. Smaller gold colloids (core diameter D=20 nm) were all spherical (**Figure 5.5a,b,c**) with monodisperse size distribution, while bigger colloids (D=60 and 150 nm) had more heterogeneous shapes (**Figure 5.5d,e**). Several long colloids were observed when gold diameter was 60 nm (**Figure 5.5d**), while long and triangular shapes were observed when gold diameter was 150 nm (**Figure 5.5e**). This is due to the particularities of the formation steps which consist in the gold nuclei growth, dissolution of smaller particles and then redeposition of the dissolved species on larger particles. For bigger NPs, dissolution is negligible compared to aggregation, allowing the development of different shapes. However, whatever was the shape of gold colloids (spherical or non-spherical), silica shell growth with different thicknesses always followed well the shape of gold colloids as can be observed in **Figure 5.5**.

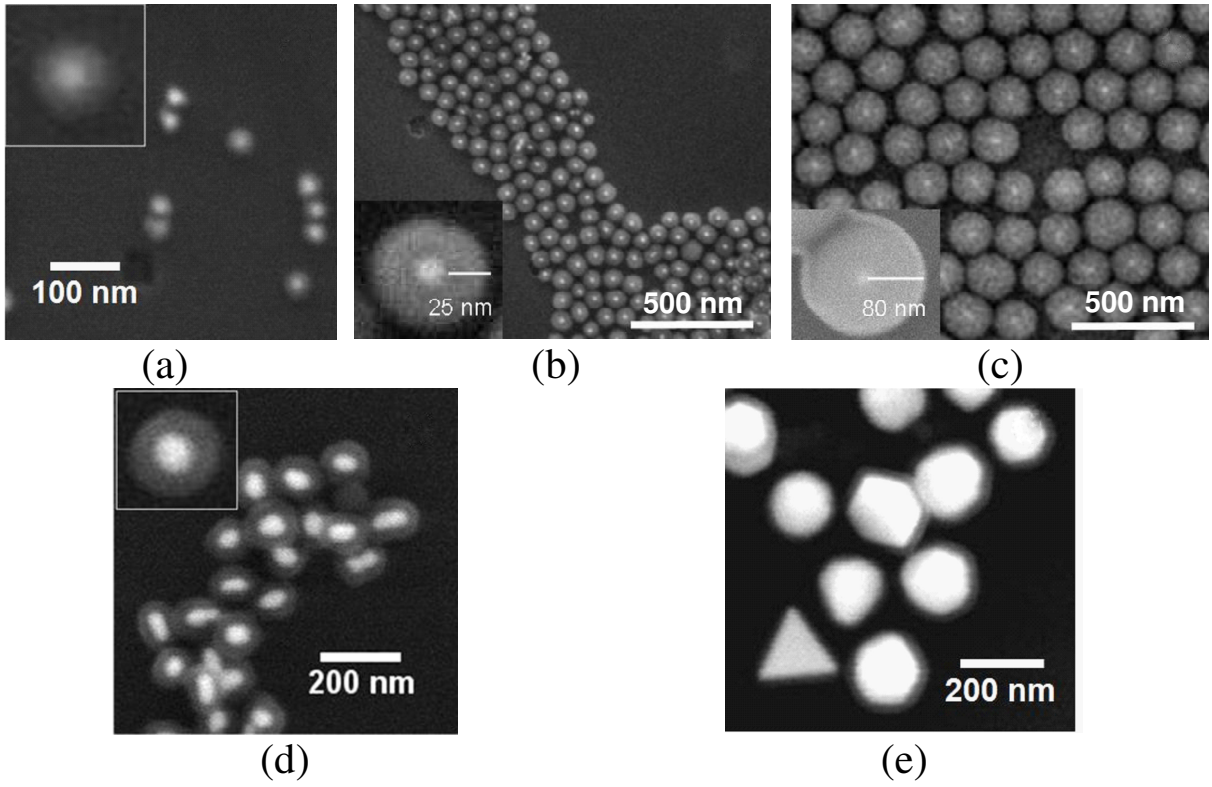

Figure 5.5*: SEM images of 20 nm-gold colloids coated with a silica shell of different thickness: (a) 10nm, (b) 25 nm, (c) 80 nm, (d) 60 nm gold core coated with 30 nm silica, and (e) 150 nm gold core coated with 15 nm silica shell. The insets show high magnification images on a single particle.*

The immobilization of SiC NPs onto silica was then controlled by TEM (**Figure 5.6**). For the physical adsorption (**Figure 5.6a**), SiC NPs are not attached very well on the surface and can be distinguished apart from the NHs. Similar isolated SiC NPs can be found for

electrostatic method. However, strong immobilizaion of NPs can be also observed (**Figure 5.6b**). Finally, for the covalent bonding single SiC NPs were never observed, proving the stability of this immobilization method **(Figure 5.6c)**. High magnification TEM image also indicates that a weak density of SiC NPs can be obtained on silica surface (**Figure 5.6d**).

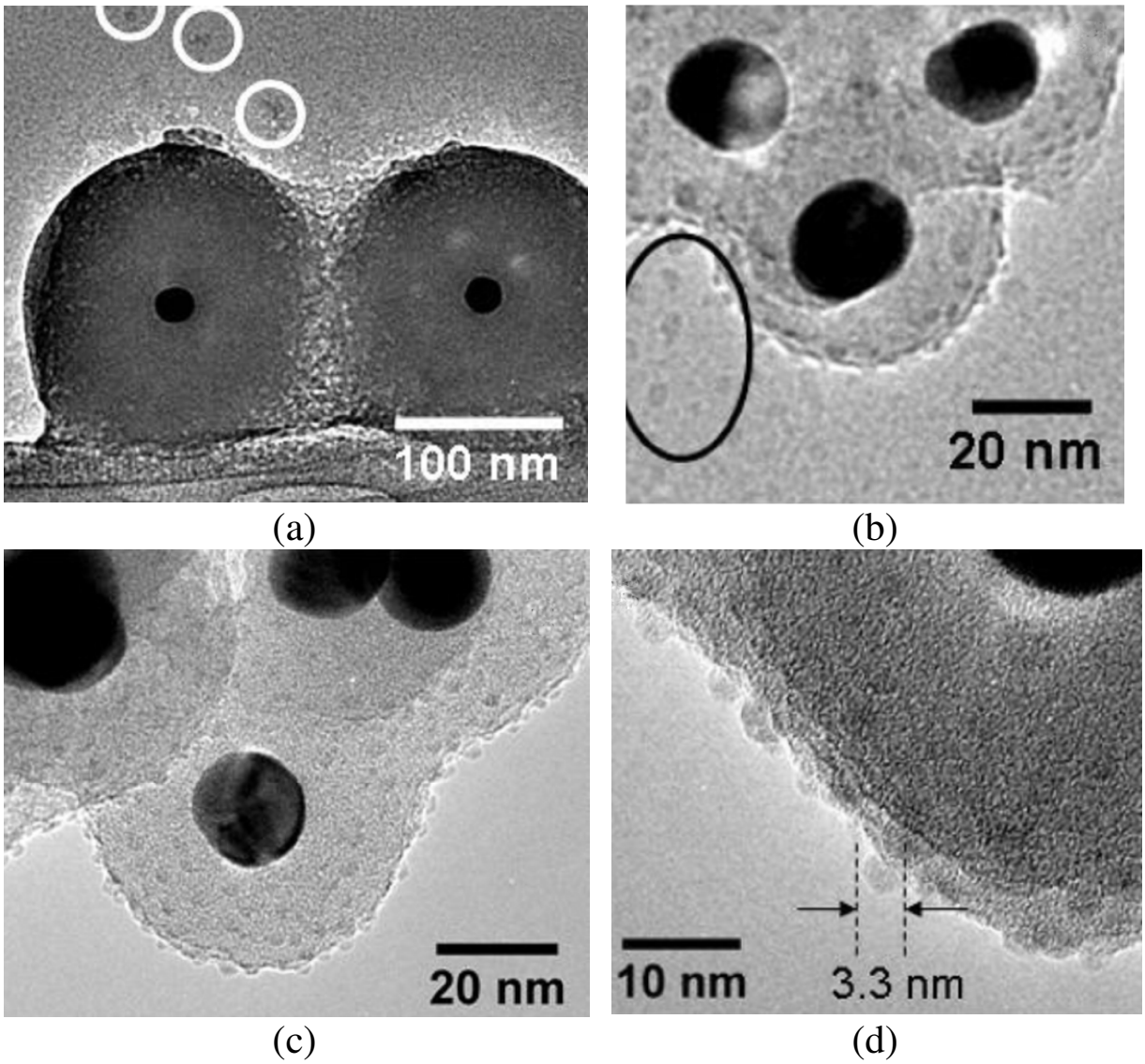

***Figure 5.6**: TEM image of (Au@SiO_2)SiC prepared by: (a) physical adsorption, (b) electrostatic bonding, (c) covalent bonding of SiC NPs, and (d) covalent bonding at higher magnification.*

Absorption spectroscopy was used to investigate the position of gold plasmon bands as a function of silica thickness and gold core size (**Figure 5.7**). Au-20nm@SiO_2-10nm and Au-20nm@SiO_2-25nm NPs exhibited narrow plasmon band in the 520-530 nm region (**Figure 5.7a,b**). As can be seen in **Figure 5.7c,d,** when the diameter of metallic core increased plasmon band became broader and red-shifted. This behaviour can be attributed to the large

shape distributions of 60 nm and 150 nm gold colloids and appearance of higher-order plasmon modes with red-shift of the dipolar ones.

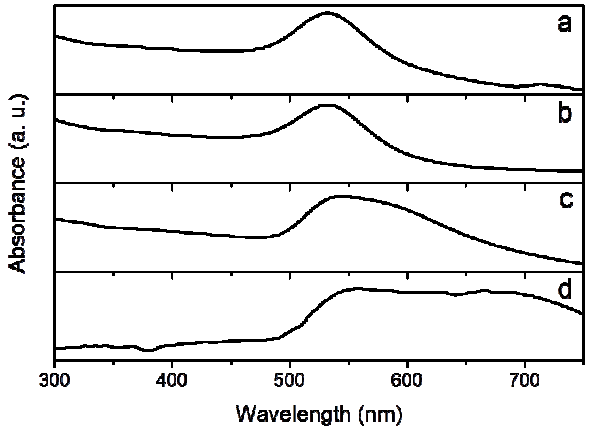

***Figure 5.7**: Absorption spectra of Au@SiO_2 NPs with various gold core diameters and silica shell thicknesses: (a) Au-20nm@SiO_2-10nm, (b) Au-20nm@SiO_2-25nm, (c) Au-60nm@SiO_2-30nm and (d) Au-150nm@SiO_2-15nm.*

An example of preliminary PL studies of the SiC NPs attached by electrostatic and covalent bonding on the surface of Au-20nm@SiO_2-25 NPs can be seen in **Figure 5.8**. The excitation was chosen to be at 488 nm for several reasons. Firstly, as it was shown in Chapter 3, small particles with quantum confinement effects are luminescent around 450 nm. In this case, neither excitation/absorption nor emission spectral match with plasmon mode at 520 nm can be obtained. Secondly, for larger NPs with emission wavelengths >500 nm dipole plasmon mode can ensure PL enhancement. Moreover, when the excitation will be closer to the plasmon mode one can expect also absorption enhancement. PL spectra in **Figure 5.8** exhibit intense Raman peaks around 570-580 nm, due to the solvent (ethanol/water). The broad band at lower intensity and located between 500 and 750 nm corresponds to the PL signal of SiC NPs and NHs when excited at 488 nm. For the electrostatic bonding (**Figure 5.8a**), a neglectable increase was obtained and the shape of emission spectra was unchanged while a strong enhancement and a blue-shift of the spectrum was observed for covalent bonding (**Figure 5.8b**). The weak enhancement obtained for electrostatic bonding can be attributed to the unstable immobilization of SiC NPs as shown on TEM image (**Figure 5.6b**). In the case of the spectral reshaping observed in **Figure 5.8b**, the blue-shift can be due to strong surface chemistry modification of SiC NPs when they are covalently bonded to silica. As previously described in Chapter 3, chemical environment has a high influence on SiC NPs optical properties. To verify this explanation, a reference sample involving silica particles without a gold core were prepared. SiC NPs were immobilized covalently with the same procedure as the one used for NHs. The PL spectrum of this SiO_2-SiC sample was compared to the one of SiC reference sample with the same SiC concentration (**Figure 5.9**). The first remark is that the fluorescence intensity of SiC NPs reference sample is quite the same as the fluorescence intensity of SiO_2-SiC reference sample, which proves that silica does not induce

fluorescence enhancement. Secondly, the emission spectrum of SiO_2-SiC has a weak band at 525 nm, which can be attributed to the surface modification of SiC NPs when they are covalently linked to silica.

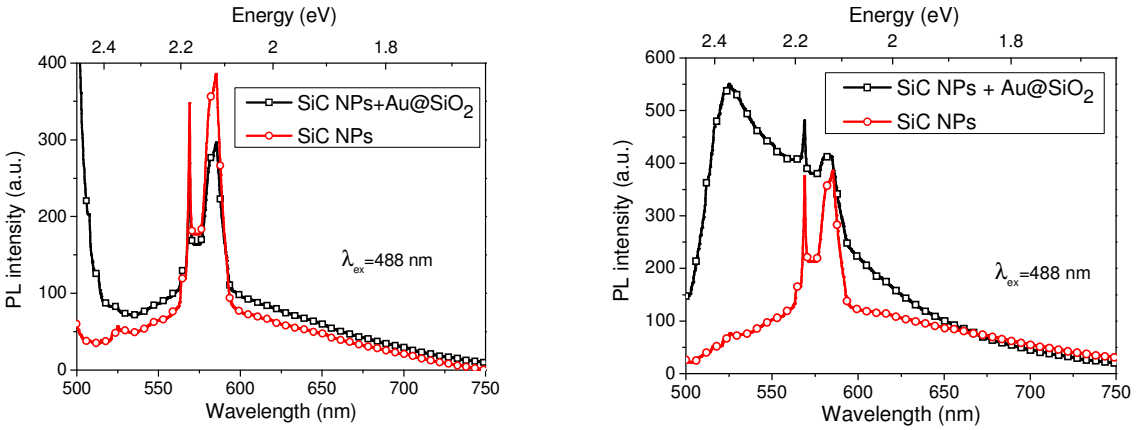

(a) (b)

***Figure 5.8**: PL spectra of Au@SiO_2-SiC NHs with (a) electrostatic and (b) covalent bonding in comparison with the same amount of SiC NPs.*

Nature of the drastic PL enhancement seen in **Figure 5.8** for covalent bonding is still unclear. It is even more surprising since the near-field effect should be rather low at 25 nm distance from the 20 nm gold core surface. In order to fully exploit potential of proposed colloidal NHs several problem should be solved in future. Firstly, silica shell fabrication of only few nanometres in size has to be improved. Mertens et al. [32] reported that optimal fluorophore-metal distance for emission enhancement is located in this range. Secondly, since only the smallest SiC NPs are dominantly bonded to the surface of NHs (**Figure 5.6**) maximal plasmon enhancement can not be ensured from viewpoint of absorption/emission spectral overlap. To resolve this complication metallic core in NHs can be changed to silver for better interaction. For this material basic dipole plasmon mode is located in higher energy spectral range, where PL of SiC NPs occurs.

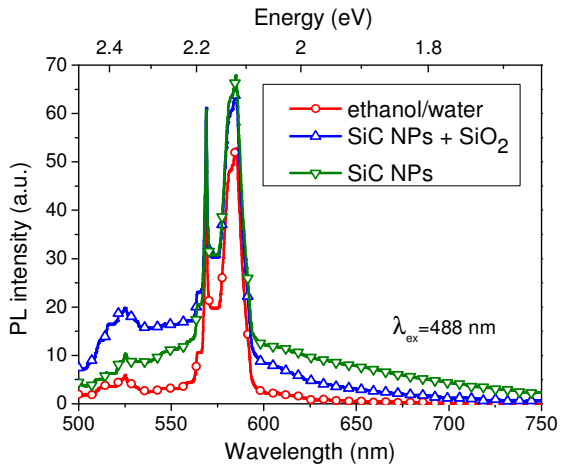

***Figure 5.9**: PL spectra of solvent (ethanol/water), SiO_2-SiC NHs obtained by covalent bonding in comparison with the same amount of SiC NPs.*

5.3. Conclusions

In this chapter, SiC NPs were shown to be promising material in bio-imaging applications. In order to increase PL intensity of SiC NPs localized in fibroblast cells, the latter one were deposited directly on the nano-Ag/SiN_X/glass plasmonic substrates. The calculated PL enhancement was found to be around 8. To avoid future silver-induced cytotoxicity, a solid-state dielectric or a molecular spacer can be easily used as a barrier between the metallic NPs and biological cells.

As a perspective, it was also demonstrated that SiC NPs can be immobilized on the surface of elaborated Au@SiO_2 NHs with controlled silica thickness and core size. It was important to note that optical properties of immobilized SiC NPs can be strongly affected due to various mechanisms. In addition to plasmon enhancement, chemical bonding can alter electronic transitions of SiC NPs by means similar to those discussed in Chapter 3. Finally, at high concentration of SiC NPS on the surface of NHs, interparticle effects can take place. The preliminary results indicate on the applicability of NHs as versatile and “all-biocompatible” nanoprobes in life sciences.

5.4. References

1. CUMMINGS R.J., MITRA S., LORD E.M., et al. Antibody-labeled fluorescence imaging of dendritic cell populations in vivo. Journal of Biomedical Optics, 2008, vol. 13, no. 044041.
2. TSIEN R.Y. Building and breeding molecules to spy on cells and tumors. FEBS Letters, 2005, vol. 579, p.927–932.
3. BRANDIZZI F., FRICKER M., HAWES C. A greener world: the revolution in plant bioimaging. Nature Reviews. Molecular Cell Biology, 2002, vol. 3, p.520–30.
4. MEDAROVA Z., PHAM W., FARRAR C., et al. In vivo imaging of siRNA delivery and silencing in tumors. Nature Medicine, 2007, vol. 13, no. 3, p.372–377.
5. MEDINTZ I.L., UYEDA H.T., GOLDMAN E.R., et al. Quantum dot bioconjugates for imaging, labelling and sensing. Nature Materials, 2005, vol. 4, no. 6, p.435–446.
6. MICHALET X., PINAUD F.F., BENTOLILA L. A., et al. Quantum dots for live cells, in vivo imaging, and diagnostics. Science, 2005, vol. 307, p.538–44.
7. ALIVISATOS P. The use of nanocrystals in biological detection. Nature Biotechnology, 2004, vol. 22, no. 1, p.47–52.
8. DUBERTRET B., SKOURIDES P., NORRIS D.J., et al. In vivo imaging of quantum dots encapsulated in phospholipid micelles. Science, 2002, vol. 298, p.1759–62.
9. HINES M.A., GUYOT-SIONNEST P. Synthesis and Characterization of Strongly Luminescing ZnS-Capped CdSe Nanocrystals. The Journal of Physical Chemistry, 1996, vol. 100, no. 2, p.468–471.
10. PENG Z.A., PENG X. Formation of high-quality CdTe, CdSe, and CdS nanocrystals using CdO as precursor. Journal of the American Chemical Society, 2001, vol. 123, no. 1, p.183–184.
11. HINES M.A., GUYOT-SIONNEST P. Bright UV-Blue Luminescent Colloidal ZnSe Nanocrystals. The Journal of Physical Chemistry B, 1998, vol. 102, no. 19, p.3655–3657.
12. SUYVER J.F., WUISTER S.F., KELLY J.J., et al. Synthesis and Photoluminescence of Nanocrystalline ZnS:Mn 2+. Nano Letters, 2001, vol. 1, no. 8, p.429–433.
13. MOZAFARI M., MOZTARZADEH F., TAHRIRI M. Green synthesis and characterisation of spherical PbS luminescent micro- and nanoparticles via wet chemical technique. Advances in Applied Ceramics, 2011, vol. 110, no. 1, p.30–34.
14. DU H., CHEN C., KRISHNAN R., et al. Optical Properties of Colloidal PbSe Nanocrystals. Nano Letters, 2002, vol. 2, no. 11, p.1321–1324.

15. LARSON D.R., ZIPFEL W.R., WILLIAMS R.M., et al. Water-soluble quantum dots for multiphoton fluorescence imaging in vivo. Science, 2003, vol. 300, p.1434–1436.
16. FRANTSUZOV P., KUNO M., JANKÓ B., et al. Universal emission intermittency in quantum dots, nanorods and nanowires. Nature Physics, 2008, vol. 4, p.519–522.
17. HARDMAN R. A Toxicologic Review of Quantum Dots: Toxicity Depends on Physicochemical and Environmental Factors. Environmental Health Perspectives, 2006, vol. 114, no. 2, p.165–172.
18. LEWINSKI N., COLVIN V., DREZEK R. Cytotoxicity of nanoparticles. Small, 2008, vol. 4, no. 1, p.26–49.
19. FAN J., LI H., JIANG J., et al. 3C-SiC nanocrystals as fluorescent biological labels. Small, 2008, vol. 4, no. 8, p.1058–1062.
20. BOTSOA J., LYSENKO V., GÉLOËN A., et al. Application of 3C-SiC quantum dots for living cell imaging. Applied Physics Letters, 2008, vol. 92, no. 173902.
21. NABIEV I., MITCHELL S., DAVIES A., et al. Nonfunctionalized nanocrystals can exploit a cell's active transport machinery delivering them to specific nuclear and cytoplasmic compartments. Nano Letters, 2007, vol. 7, no. 11, p.3452–3461.
22. SERDIUK T., ALEKSEEV S.A., LYSENKO V., et al. Charge-driven selective localization of fluorescent nanoparticles in live cells. Nanotechnology, 2012, vol. 23, no. 315101.
23. BOTSOA J. Synthèse de nanostructures de carbure de silicium et étude de leurs propriétés optiques. Lyon: INSA de Lyon, 2008, 146 p.
24. ZHANG J., FU Y., LIANG D., et al. Enhanced fluorescence images for labeled cells on silver island films. Langmuir, 2008, vol. 24, no. 21, p.12452–12457.
25. ZHANG J., FU Y., MEI Y., et al. Fluorescent metal nanoshell probe to detect single miRNA in lung cancer cell. Analytical Chemistry, 2010, vol. 82, no. 11, p.4464–4471.
26. ZHANG J., FU Y., LAKOWICZ J.R. Fluorescent Metal Nanoshells: Lifetime-Tunable Molecular Probes in Fluorescent Cell Imaging. The Journal of Physical Chemistry C, 2011, vol. 115, p.7255–7260.
27. SZMACINSKI H., RAY K., LAKOWICZ J.R. Metal-enhanced fluorescence of tryptophan residues in proteins: application toward label-free bioassays. Analytical Biochemistry, 2009, vol. 385, p.358–364.
28. RAY K., SZMACINSKI H., LAKOWICZ J.R. Enhanced fluorescence of proteins and label-free bioassays using aluminum nanostructures. Analytical Chemistry, 2009, vol. 81, no. 15, p.6049–6054.

29. TOVMACHENKO O.G., GRAF C., VAN DEN HEUVEL D.J., et al. Fluorescence Enhancement by Metal-Core/Silica-Shell Nanoparticles. Advanced Materials, 2006, vol. 18, p.91–95.
30. LIU N., PRALL B.S., KLIMOV V.I. Hybrid gold/silica/nanocrystal-quantum-dot superstructures: synthesis and analysis of semiconductor-metal interactions. Journal of the American Chemical Society, 2006, vol. 128, no. 48, p.15362–15363.
31. GARTIA M.R., HSIAO A., SIVAGURU M., et al. Enhanced 3D fluorescence live cell imaging on nanoplasmonic substrate. Nanotechnology, 2011, vol. 22, no. 365203.
32. MERTENS H., KOENDERINK A.F., POLMAN A. Plasmon-enhanced luminescence near noble-metal nanospheres: Comparison of exact theory and an improved Gersten and Nitzan model. Physical Review B, 2007, vol. 76, no. 115123.

General Conclusions

As part of this thesis, two different approaches for nano-SiC fabrication have been described. Firstly, SiC nanopowder was obtained by simple and inexpensive electrochemical etching method. However, this procedure involves extremely toxic and corrosive electrolytes based on hydrofluoric (HF) acids. Thus, direct and clean laser ablation method was additionally used to produce colloidal suspensions of luminescent SiC NPs in water.

Size dependence of complex optical response from the elaborated nanostructures has been investigated after filtration and centrifugation techniques. It was confirmed by structural and elemental analysis that electrochemical etching method allows supplementary formation of a large amount of carbon-based nanostructures. These objects were reported in literature to be also optically active in UV-Visible region. After preparation, both components (carbon and SiC) may form complex structures with strong near-field interaction evidenced by PL and optical absorption studies. For example, oxidation-induced carbon removal allowed visualization of the transitions between energy levels in the SiC NPs in which photo-generated charge carriers are quantumly confined.

The most importantly, chemical environment strongly influenced the electronic transitions in the carbon-SiC NPs. In particular, the solvent nature and the surface charges of the NPs have to be considered in terms of local field effects to understand the spectral peculiarities of the absorption and PL spectra. Observed dependencies have been described by electron-hole wavefunction overlapping and redistribution of localized energy states in the band-gap.

Original optical properties of SiC nanostructures allow their various promising applications as light-emitting agents and in nonlinear optics. However, in comparison with commonly used materials, the reported characteristics of the SiC nanostructures have to be enhanced. PL enhancement of the SiC NPs induced by their efficient near-field coupling with multi-polar localized plasmons has been experimentally demonstrated. In order to understand and illustrate main physical mechanisms involved in a complex interaction between the localized plasmons and emitting SiC NPs, as well as to estimate absorption and scattering efficiencies of the used nano-Ag/SiN_X/glass substrates three-dimensional FDTD simulations have been performed. In particular, high PL enhancement factors can be ensured by localization of the SiC NPs at the plasmon-induced high field regions and by a spectral overlap of multi-polar plasmon modes with absorption/excitation and emission bands of the

NPs. Moreover, a detailed experimental study of the plasmon-induced enhancement of non-linear response in SiC NPs has been presented. Despite a number of studies devoted to the clarification of the physical mechanisms involved in such phenomenon, none of them was explicitly addressed to the case of SiC NPs.

In perspective, there is a whole field of action and research on the application of SiC NPs for biological cell labeling. These NPs can be bio-chemically functionalized for targeting the specific cell components. In order to increase PL intensity of SiC NPs localized in fibroblast cells, the latter ones have been deposited directly on the nano-Ag/SiN_X/glass plasmonic substrates. To avoid future silver-induced cytotoxicity, a solid-state dielectric or a molecular spacer can be easily used as a barrier between the metallic NPs and biological cells.

As a perspective, it was also demonstrated that SiC NPs can be immobilized on the surface of elaborated Au@SiO_2 nanohybrids with controlled silica thickness and core size. The preliminary results indicate on the applicability of the nanohybrids as versatile and "all-biocompatible" nanoprobes in life sciences.

List of publications

Portions of this thesis have appeared in the following publications :

- ZAKHARKO Y., BOTSOA J., ALEKSEEV S.A., et al. Influence of the interfacial chemical environment on the luminescence of 3C-SiC nanoparticles. Journal of Applied Physics, 2010, vol. 107, no. 013503. (Chapter 3)
- ZAKHARKO Y., RIOUX D., PATSKOVSKY S., et al. Direct synthesis of luminescent SiC quantum dots in water by laser ablation. physica status solidi-Rapid Research Letters, 2011, vol. 5, no. 8, p.292-294. (Chapter 3)
- ZAKHARKO Y., LYSENKO V. Local electric field effects on photo-induced electronic transitions in SiC quantum dots. AIP Conference Proceedings, 2011, vol. 1399, p. 455-456. (Chapter 3)
- NYCHYPORUK T., ZAKHARKO Y., SERDIUK T., et al. Strong photoluminescence enhancement of silicon quantum dots by their near-resonant coupling with multi-polar plasmonic hot spots. Nanoscale, 2011, vol. 3, p.2472–2475. (Chapter 4)
- ZAKHARKO Y., SERDIUK T., NYCHYPORUK T., et al. Plasmon-enhanced photoluminescence of SiC quantum dots for cell imaging applications. Plasmonics, 2012, doi:10.1007/s11468-012-9364-2. (Chapter 4, 5)
- SUI N., MONNIER V., ZAKHARKO Y., et al. Plasmon-controlled narrower and blue-shifted fluorescence emission in (Au@SiO2)SiC nanohybrids. Journal of Nanoparticle Research, 2012, vol. 14(8), no. 1004. (Chapter 5)
- SUI N., MONNIER V., ZAKHARKO Y., et al. Fluorescent (Au@SiO2)SiC nanohybrids: influence of gold nanoparticle diameter and SiC nanoparticle surface density. Plasmonics, 2012, doi:10.1007/s11468-012-9425-6. (Chapter 5)

FOLIO ADMINISTRATIF

THESE SOUTENUE DEVANT L'INSTITUT NATIONAL DES SCIENCES APPLIQUEES DE LYON

NOM : ZAKHARKO DATE de SOUTENANCE : 30/10/2012

Prénoms : Yuriy

TITRE : INITIAL AND PLASMON-ENHANCED OPTICAL PROPERTIES OF NANOSTRUCTURED SILICON CARBIDE

NATURE : Doctorat Numéro d'ordre : 2012ISAL0105

Ecole doctorale : Matériaux de Lyon

Spécialité : Physique des matériaux

RESUME :

Le carbure de silicium (SiC) nanosturturé est considéré aujourd'hui comme une bonne alternative aux matériaux traditionnels pour diverses applications multidisciplinaires. Dans cette thèse, des nanostructures de SiC ont été élaborées par gravure électrochimique et par ablation laser. La première partie de cette thèse décrit et explique la dépendance en taille des propriétés optiques ainsi que l'importance des effets de champ local sur les transitions électroniques photo-induites des nanostructures de SiC. Dans la seconde partie, il est démontré une amplification d'un facteur 15 de l'intensité de photoluminescence des nanoparticules de SiC par leurs interactions en champ proche avec les plasmons multipolaires localisées. En outre, un facteur 287 et un facteur 72, induits par le couplage plasmonique, sont obtenus respectivement pour les signaux de luminescence à deux photons et de génération de seconde harmonique. Les principaux mécanismes physiques responsables des effets observés ont été décrits par des simulations de type différences finies dans le domaine temporel en trois dimensions. Enfin, l'effet de couplage de nanoparticules de SiC luminescentes à des nanostructures plasmoniques en structures planes est utilisé pour améliorer le marquage de cellules biologiques. Une perspective est ouverte sur la réalisation et les premières caractérisations de suspension colloïdales de nanohybrides plasmonique (Au@SiO_2)SiC.

MOTS-CLES : Nanostructures de SiC, Confinement quantique, Photoluminescence, Réponse optique non linéaire, Exaltation plasmonique, Marquage biologique.

Laboratoire (s) de recherche : Institut des Nanotechnologies de Lyon

Directeur de thèse: BLUET Jean-Marie, LYSENKO Vladimir

Président de jury : DUJARDIN Christophe

Composition du jury : LERONDEL Gilles, ROZHIN Alex, DEREUX Alain, PAILLARD Vincent, MONNIER Virginie, BLUET Jean-Marie